Universität Bremen

Influence of Microstructure on Damage Behavior of Sound Absorbing Ceramics

Vom Fachbereich Produktionstechnik

der

Universität Bremen

zur Erlangung des Grades

Doktor-Ingenieur

genehmigte

Dissertation

von

M. Sc. Reza Malekmohammadi Nourifar

Gutachter: Prof. Dr.-Ing. habil. Reinhold Kienzler

Prof. Dr.-Ing. Vasily Ploshikhin

Tag der mündlichen Prüfung: 24.04.2012

Acknowledgements

The presented work was carried out as a research project within the framework of the Graduate School PoreNet (None metallic Porous Structures for Physical-Chemical Functions) at the University of Bremen. The productive intramural cooperation between the Faculty of Applied Mechanics and the Faculty of Combustion at the Center of Applied Space Technology and Microgravity (ZARM) has culminated in a contribution to the investigation of the mechanical behavior of sound absorbing ceramics at high temperature applications. I appreciate the German Research Foundation (DFG) for the financial support of this project, the council and also the organizers of PoreNet for their supports, feedbacks and efficient program in the last three years.

My special thanks go to Professor Reinhold Kienzler for the opportunity of doing this work, for giving me freedom of action, his complete support and endless patience. Further, I want to thank Professor Vasily Ploshikhin for acting as the second reviewer of this thesis.

Dr. Mostafa Mehrafza has played a significant role in my life in the last eight years. For all exchange of ideas, suggestions and the noble technical discussions regarding this contribution I am truly thankful.

Furthermore, I would like to express my gratitude to Professor Frank Jablonski as my project director for his active and boundless support. Dipl.-Ing. Roland Schröder and Cand. Dipl.-Ing. Kevin Kutz have supported me kindly in programming the user-subroutine in this work. Mr. Schröder as a bike specialist has always shared generously his knowledge with me and taught me the maintenance of bikes as well as its pitfall. Mr. Kutz was an enthusiastic hard-working student assistant at the faculty. In many aspects

we could exchange our knowledge and experiences. He also boosted up my technical expertise in IT. I am grateful to them.

Also, I want to utter my gratitude to Dr. Mohammad Ali Taheri whose mystical world-view changed my life positively in many respects.

My deepest gratitude goes to my wonderful parents for giving me a nurturing home and a good education, to my lovely brother and to Shima.

Last, but not least, I thank my Creator for blessing me with good health and overall luck in life.

Abstract

Porous sound-absorbing ceramics are gaining great importance in the combustion chamber of gas turbines and in exhaust silencers. They contribute to the passive damping of thermo-acoustic instabilities and sound dissipation. As ceramic liners, they must satisfy all requirements respecting mechanical strength and thermal resistance. Design and development of such ceramics concern various aspects like thermal shock resistance, crack behavior, fatigue limit, creep and erosion resistance.

Based on the freeze gelation process, a new technique to produce porous sound absorbing ceramic is introduced in the framework of the research projects at the graduate school PoreNet. It uses a wide range of advantages of freeze gelation with regard to production and application of sound absorbing ceramic over other procedures such as injection molding or gel casting. The ceramic components produced by this technique are near-net-shape and feature an open-pored structure with high connectivity and porosity. They present, in contrast to traditional fibrous absorbing materials, a combination of good sound absorption, high temperature resistance, chemical inertness and material strength.

The aim of this work is to investigate the mechanical behavior of highly porous sound absorbing ceramics and to predict the brittle damage behavior considering the material microstructure. It studies the applicability of such ceramics as insulation liners for the combustion chambers and gives a clue to further material improvement in terms of mechanical strength.

Experiments were performed in this work to characterize the mechanical strengths of this new sound absorbing ceramic for the application as ceramic heat shields for the combustion chambers of premixed gas turbines. Compressive tests at both room and high temperature as well as four-point bending tests at room temperature have been carried out. Furthermore, the fits of fracture strengths of the material to the Normal, Weibull and

Type I extreme value distributions are investigated. The characterization was then expanded to other physical properties such as porosity, density, thermal conduction coefficients and thermal expansion coefficients.

The underlying theory for the mechanical investigation varies depending on the physical processes occurring in these ceramic liners. Considering, for example, the transpiration cooling technique obtained by a porous wall in the combustion chamber of gas turbines, there are two heat exchange effects: the film effect at the warmer front where hot and cold gases mix, and the convective effect at the cooler surface through the wall. These cooling condition prerequisites a multi-physic approach towards description of the mechanical behavior of sound absorbing ceramic liners. The Theory of Porous Media (TPM), Theory of Mixtures combined with the Concept of Volume Fractions, provides a macroscopic description of immiscible or miscible multiphasic aggregates. Due to this macroscopic approach, however, structural parameters like pore distribution and pore shape are indirectly considered in the material parameters of the model, which is disadvantageous in terms of material development, since a precise study of influencing factors of each structural parameter on the overall behavior of the material demands a set of experiments to determine the material parameters.

Since no cooling air flow is considered to take place in these developed ceramic liners, a non-multi-physic but multi-scale approach is applied in this work which predicts the influence of the microstructure on the macroscopic properties. The scale transition method is known as mean-field homogenization method, based on assumed relations between average values of micro-strain and -stress fields in each phase. This homogenization model is based on the Eshelby model and assumes the pores (or rather inclusions) to be ellipsoidal. Influence of the pore density, pore form and pore orientation on the strength of these porous sound absorbing ceramic are studied here. Depending on

the loading condition higher strength by higher porosity values is achievable by for example aligning the pores on a desired direction or changing their form from spherical to ellipsoid with high aspect ratios.

Furthermore, direct finite element simulations of a representative-volume element (RVE) are also implemented in this work to investigate the pure brittle damage of this sound absorbing ceramic. An effective-stress degradation model has been implemented in a predefined user-subroutine of ABAQUS. It is based on the three dimensional rupture criterion and describes the pure brittle damage under mechanical, thermomechanical, static and quasi-static loadings. Different RVE's have been generated and investigated in terms of damage considering different structural parameters.

The present results demonstrate the application potential of these sound absorbing ceramic as liner in terms of mechanical strengths, predict their brittle damage behavior considering the microstructure and provide a base for further material developments and numerical investigations. The applicability of these ceramic to line the combustion chambers in terms of sound absorption is investigated on an experimental set-up at the Faculty of Combustion of the Center of Applied Space Technology and Microgravity (ZARM). The validation of the results from this chapter will be performed on this set-up.

Zusammenfassung

Schallabsorbierende poröse Keramiken erhalten immer mehr Bedeutung beim Einsatz in den Brennkammern von Gasturbinen, in denen sie zur passiven Dämpfung der thermoakustischen Instabilitäten und somit zur Schalldissipation beitragen. Als keramische Auskleidung müssen sie jegliche Anforderungen hinsichtlich der mechanischen Festigkeit und der thermischen Beständigkeit erfüllen.

Die vorliegende Arbeit entstand im Rahmen des Graduiertenkollegs PoreNet und untersucht das mechanische Verhalten, insbesondere das spröde Schädigungsverhalten, von hochporösen, schallabsorbierenden, Keramiken in Abhängigkeit der Strukturparameter wie Porosität, Porengröße und Porenverteilung. Die Arbeit überprüft ferner die Einsetzbarkeit dieser Keramiken als Isolierkacheln in Brennkammern und weist auf mögliche Materialverbesserungen hinsichtlich der mechanischen Festigkeit hin.

Zunächst wurden die physikalischen, mechanischen und thermodynamischen Eigenschaften der im Graduiertenkolleg PoreNet entwickelten schallabsorbierenden porösen Keramik ermittelt. Für die Beschreibung der Streuung der Festigkeitswerte aus Druck- und Vier-Punkt-Biegeversuchen wurde ein Vergleich zwischen Normalverteilung, Weibull-Verteilung und Typ I Extremwert-Verteilung durchgeführt.

Durch einen Mehrskalenansatz, basierend auf der “Mean-Field”-Homogenisierungsmethode, wurden die makroskopischen Eigenschaften in Abhängigkeit von den Parametern der Mikrostruktur vorhergesagt. Die Einflüsse von Porosität, Porenform und Porenorientierung auf die Festigkeit der schallabsorbierenden porösen Keramiken wurde untersucht.

Die rein spröde Schädigung in schallabsorbierenden porösen Keramiken wurde durch Finite-Elemente-Simulationen an repräsentativen Volumenelementen (RVE) untersucht. Ein Degradationsmodell basierend auf effektiven Spannungen wurde für die

Untersuchung in eine vordefinierte User-Subroutine des Finite-Elemente-Programms ABAQUS implementiert. Das Modell beruht auf einem dreidimensionalen Bruchkriterium und beschreibt die rein spröde Schädigung unter statischer, bzw. quasi-statischer mechanischer und thermomechanischer Belastung. Die Modellvalidierung erfolgt durch die Simulation eines Druckversuchs und den Vergleich zwischen statistisch ermittelten Festigkeitswert aus dem Experiment und der berechneten kritischen Druckbelastung am RVE.

Die präsentierten Ergebnisse in dieser Arbeit bestätigen die potenzielle Einsetzbarkeit dieser schallabsorbierenden Keramiken und sagt die Schädigung sowohl im repräsentativen Volumenelement als auch in der realen Isolierkachel vorher. Eine experimentelle Validierung der Einsetzbarkeit der schallabsorbierenden Isolierkacheln wird am Prüfstand des Fachgebiets „Verbrennung und Antriebe der Luft- und Raumfahrt“ im Zentrum für Angewandte Raumfahrttechnologie und Mikrogravitation (ZARM) durchgeführt werden.

Eidesstattliche Erklärung gemäß § 5 Abs. 1 der Promotionsordnung

Hiermit erkläre ich, Reza Malekmohammadi Nourifar, geboren am 28.08.1978 in Teheran - Iran, an Eides statt, dass ich mich an keiner weiteren Stelle einem Promotionsverfahren unterzogen oder ein solches beantragt habe.

Reza Malekmohammadi Nourifar

Table of Contents

List of Figures

List of Tables

Nomenclature

$\boldsymbol{\varepsilon}$	Tensorial total strain
ε_{ij}^{e}	Tensorial elastic strain
ν	Poisson's ratio
ρ	Mass density
σ , σ_{ij} , $\boldsymbol{\sigma}$	Uniaxial and tensorial stresses
σ_H	Hydrostatic stress
σ_{eq}	Von Mises equivalent stress
σ^*	Damage equivalent stress
σ_u	Ultimate stress
σ_R	Stress to rupture
a_{ijkl}	Elastic moduli
c	Specific heat capacity
D	Damage variable
D_c	Critical damage at crack initiation
D_{1c}	Critical damage in pure tension
$\dot{e}$	Specific internal energy rate
E	Modulus of elasticity
F	Force
$\mathbf{I}$	Unit tensor
j	Scale fractal parameter
$\dot{k}$	Specific kinetic energy rate
m	Weibull parameter
p_x	Specific external force power
$\mathbf{q}$	Heat flux
φ	Porosity
Q	Parameter
Q	Input heat rate
r	Volumetric heat supply
R	Fracture strength
R_v	Tiaxiality function
t	Time
T	Temperature
V_s	Volume fraction of solid
ω_e	Elastic strain energy density
Y	Strain energy density release rate
Y_c	Critical strain energy density release rate at rupture

1 Introduction

MOTIVATION

Porous sound-absorbing ceramics have become of great importance in the combustion chamber of gas turbines and in exhaust silencers. They contribute to sound dissipation and passive damping of thermo-acoustic instabilities. Consideration of this property requires introducing highly porous ceramic liners which not only prevent the occurrence of acoustic instability, but also expand the stable operating range towards lean burning through acoustic damping. Therefore, it is essential to develop a material with structural conditions conformed to the design and development criteria. The developed material must satisfy all requirements respecting mechanical strength and thermal resistance.

In the Graduate School PoreNet “None metallic Porous Structures for Physical-Chemical Functions” at the University of Bremen, within two research projects it has been striven to investigate, whether highly porous ceramics are applicable as liners in the combustion chamber of swirl stabilized premixed burners. One project deals with material development and study of acoustic effects of using such liners on the operating behavior, whereas the other project, this work, investigates their mechanical behavior and predicts their brittle damage. Based on the freeze gelation process, a new technique to produce porous sound absorbing ceramic is introduced in the framework of the first research project at the graduate school PoreNet. It uses a wide range of advantages of freeze gelation with regard to production and application of sound absorbing ceramic over other procedures such as injection molding or gel casting. The ceramic components produced by this technique are near-net-shape and feature an open-pored structure with high connectivity and porosity. They present, in contrast to traditional fibrous absorbing materials, a combination of good sound absorption, high-temperature resistance, chemical inertness and material strength.

RESEARCH AIM AND OUTLINE OF THE THESIS

It is the aim of this contribution to investigate the mechanical behavior of highly porous sound absorbing ceramics as well as their applicability as insulation-ceramic liners and to predict the brittle damage behavior considering the material microstructure.

The underlying theory for the mechanical investigation varies depending on the physical processes occurring in these ceramic liners. Considering, for example, the transpiration cooling technique obtained by a porous wall in the combustion chamber of gas turbines, there are two heat exchange effects: the film effect at the warmer front, where hot and cold gases mix, and the convective effect at the cooler surface and through the wall. These cooling condition prerequisites a multiphysic approach towards the description of the mechanical behavior of sound absorbing ceramic liners. The Theory of Porous Media (TPM), which combines the Theory of Mixtures with the Concept of Volume Fractions, provides a macroscopic description of immiscible multiphasic aggregates. A thermo-elastic isothermal biphasic model consisted of a materially incompressible thermo-elastic solid (thermal compressible) and a compressible viscous gas is applicable for this multi-physic problem. Due to this macroscopic approach, however, structural parameters like pore distribution and pore shape are indirectly considered in the material parameters of the model, which is disadvantageous in terms of material development, since a precise study of the influence of each structural parameter on the overall behavior of the material demands a set of experiments to determine the material parameter.

Since no cooling air flow is considered to take place in these developed ceramic liners, a single-physic but multi-scale approach is favored which allows the prediction of the influence of the microstructure on the macroscopic properties. The scale transition method is known as mean-field homogenization method, based on assumed relations between average values of micro-strain and -stress fields in each phase. This homogenization model is based on the Eshelby model and assumes the inclusions to be ellipsoidal. Chapter 2 deals with the theoretical foundations in fracture of ceramics,

damage criterion for brittle material and multi-scale approach for material property prediction.

Chapter 3 concerns the experiments which aim to characterize the mechanical strengths of this new ceramic sound absorber for the application as ceramic heat shields for the combustion chambers of premixed gas turbines. It starts with sample preparation and material production followed by compressive tests at both room and high temperature as well as four-point bending tests at room temperature. A comprehensive study discusses the fits of fracture strengths to the Normal, Weibull and Type I extreme value distribution. Further, the material characterization considers other physical properties such as porosity, density, thermal conduction coefficients and thermal expansion coefficients. Influence of the pore density, pore form and pore orientation on the strength of the porous sound absorbing ceramics are studied based on the mean-field homogenization method.

Chapter 4 is dedicated to simulation and damage analysis. Direct finite-element simulation of representative volume elements (RVE) has been carried out in this work to investigate the pure brittle damage of this sound absorbing ceramic, concerning its microstructure. An effective-stress degradation model has been implemented in a predefined user-subroutine of ABAQUS. It is based on the three dimensional rupture criterion and describes the pure brittle damage under mechanical, thermomechanical static and quasi-static loadings. Different RVE's have been generated and investigated in terms of damage considering different structural parameters. Further simulations are also performed on the real size ceramic tiles. Different sets of macroscopic engineering parameters for these simulations have been calculated by the mean-field homogenization method. Then, the brittle damage of a ceramic tile under critical loading with respect to its microstructure is studied.

A final conclusion and discussion is given in chapter 5 including an illustration of further possible developments based on the presented work.

LITERATURE REVIEW

Industrial gas turbines generally use natural gas as fuel which produces a little carbon dioxide, owing to the high hydrogen-carbon ratio in comparison to the combustion of coal, and emits relatively small amounts of unburnt carbon hydride. By almost complete elimination of such pollutants, the reduction of nitrogen oxides comes to the fore in the research. According to the Zeldnovich Mechanism [1] high pressure and temperature in the reaction zone affect NOx production. With this knowledg several efficient concepts were developed to diminish NOx emission. All industrial gas turbine manufacturer have moved in recent years towards lean premixed combustion to keep the flame temperature low and to suppress NOx emissions [2-3]. This concept is, however, prone to vibration of the combustion chamber and as a result, the lean extinguishing limit drives towards low air numbers [4-6]. As an example, a back coupling between the energy-release-rate variations and the periodic pressure fluctuations results in self-excited thermoacoustic instabilities with high-pressure amplitudes. This develops undesirable Low-Frequency Dynamics (LFD) which may cause adverse mechanical loads on the tiles. By varying the geometry of burner and combustion chamber or fuel insertion device it is possible to suppress these oscillations. One good approach to suppress the combustion-chamber vibrations is passive damping which manipulates the burning process with improved burner and chamber geometries [7-8], optimized fuel preparation [9] or resonators. The other approach is active controlling. An example to understand the principle of active controlling is an additional pulsating fuel mass flow that overlays by the mean fuel mass flow and acts against the variation of energy-release rate [10]. Nevertheless, both approaches face the difficulty of providing a stable burning over the total operating range. It happens frequently that a previously unconsidered frequency becomes amplified due to mode coupling with the suppression of a certain frequency. But for all that, passive damping is preferable compared to active controlling regarding maintenance effort and probable controlling failure [11]. Details of excitation mechanisms as well as relations between flow instabilities and fluctuations by heat

release are partly unknown. Further, the geometry of components like burner and combustion chamber has a decisive effect on the amplitude and frequency of vibrations.

Ceramic materials find common applications as insulating wall panels in combustion chambers of gas turbines due to their low thermal conductivity and high temperature stability. Unlike metallic tiles, the low cooling requirement of ceramic tiles results in increasing the efficiency of gas turbines. Design and development of such ceramics focus currently on aspects like isolating capability, thermal shock resistance, creep strength, fatigue resistance, fracture behavior and erosion resistance. Numerous research works deal with the development of appropriate isolating ceramics. Oxide ceramic matrix composites are promising candidates representing the aforementioned criterion [12]. Embedding ceramic fibers in a ceramic matrix produces a relief as the energy-dissipative microstructural-failure mechanism can be realized in the ceramic composites. This culminates in a ductile failure behavior of ceramics [12-13]. An example is a porous oxide-ceramic composite with uncoated oxide fibers (total porosity 25-50%) developed at the German Aerospace Center (DLR) [12], which provides low specific weight, low thermal conductivity, damage tolerance because of non brittle behavior and thermal shock stability. Hence, the sound absorption property was not treated as a design criterion for these ceramic tiles. Giese [14] has taken the sound absorption property of ceramic tiles into account and developed a ceramic with outstanding temperature resistance and sound absorption. He focused on the sound absorption in lower frequency range and applied the theory of homogenous media for the estimation of the bulk properties of the absorber [14].

A series of research works deals with the acoustic behavior of porous materials and the numerical treatment of noise insulation of solid walls. A vibrating wall which is excited by acoustic pressure, acts as the main noise source. Application of the poroelastic materials as effective sound insulators can be modeled by considering the walls as poroelastic plate. This requires the formulation of plate theories based on poroelastic constitutive equations. Classical plate theories reduce a 3-d continuum to a 2-d structure using some assumptions with regard to the strain and stress distribution in the direction of

the thickness. Biot [15-16] has presented a very first theory of wave propagation in poroelastic materials. He extended then his work to the anisotropic case [17] and poroviscoelasticity [18]. Despite an unfulfilled consistency within the framework of thermodynamics, Biot's theory is applied to model the poroelastic behavior. Further poroelastic plate formulations can be found by works of Taber [19] based on the assumption of the elastic Kirchhoff plate for the quasi-static case as well as by Theodorakoupolos and Beskos [20] for poroelastodynamic case based on the Kirchhoff plate theory. In case of a poroelastic plate theory, it is to examine, whether these assumptions can be transfered to pore pressure and the flux of the interstitial fluid. The in-plane flux was considered to be negligible in both works, whereas Cederbaum [21] assumes only the flux in the perpendicular direction to be negligible. The use of the Kirchhoff theory (valid for thin plates) or higher-order theories like Mindlin plate theory does not answer the question concerning the transferability of the kinematical assumptions for the displacement to the pore pressure [22]. Implementation of series expansions by development of plate theories waives the need to make any assumption and confrontation with this question. This approach can be found by works of Mindlin [23], Preusser [24] and Kienzler [25-26]. Based on the method of series expansions, Schanz [22] presented a method to drive poroelastic plate formulations for dynamic behavior of any desired level of approximation. It is based on the Biot's three-dimensional equations of poroelasticity in frequency domain. By order reduction, however, it uses the series expansion method in thickness direction to approximate the unknown quantities. This approach realizes a macroscopic expression of the acoustic behavior of such materials and does not give any direct clue regarding the influence of microstructure on the macroscopic acoustic behavior of the absorbing walls.

A porous medium is a solid skeleton with pores which are filled with a number of liquids and/or gases (immiscible) which represents an internal structure with a complicated geometry. The constituents have different material properties and motions. The study of the interaction between the constituents and their reactions due to the mechanical and thermomechanical effects paves the way to predict the response of these

constituents and the composed body. Based on the Theory of Porous Media (TPM) [27-32] it is possible to create a mathematical model which serves to describe on the macroscopic scale the behavior of empty and saturated porous media under mechanical and thermal load with respect to the micromechanical effects like compressibility, incompressibility, pore-water pressure on the solid and capillarity. The Theory of Porous Media represents the mixture theory combined with the volume fraction concept. The mixture theory was developed based on the description of heterogeneous composition of continua with internal interactions between the constituents and independent degrees of freedom and uses only partial quantities, which refer to a control space and cannot describe phenomena at the microscopic scale [27] [33]. Hereby, volume fractions are measures of the local portions of the individual constituents of the overall medium, and all incorporated fields are local averages of corresponding quantities of a microstructure. The volume fraction concept assumes the statistically distribution of pores over the control space and is of great advantage due to the accessibility of porosity value in comparison to the other average concepts. Thus, the porous medium is homogenized and the constituents then can be treated by continuum mechanical methods. Drumheller [34] used the volume fraction concept by description of an empty porous solid based on the theory of mixtures. Subsequently, his work was taken by Bowen [35] for introducing a porous media theory using the thermodynamics of mixtures with the volume fraction concept. A successive paper of Bowen [36] introduced an extension of his theory to compressible porous media by the use of volume fractions as internal state variables. Mow et al [37] made also an approach similar to the Bowen's theory describing two-phasic creep and stress relaxation of articulate cartilage under compression. Implantation of the developed models into numeric algorithms, extension of the developed mathematical model for further material behavior and investigation of special phenomena which appear in saturated and empty porous media are the main research direction in the TPM. Some findings in the TPM relate to the development of constitutive equations for different materials with elastic, elastic-plastic, and viscous behavior, the concept of effective stress and the implementation of the basic equations in numerical processes, the

incorporation of the Cosserat kinematics into the theory of porous media and fundamental phenomena such as capillarity, friction and uplift. The TPM has found application by a variety of porous materials like metal foams [38], tissues, geo-materials [39-40], polymer foams [41] and porous ceramics [42].

Depending on the problem, a micro- or macroscopic approach can be implemented. In the macroscopic range, all defined and measured quantities in the microscopic scale are statistically averaged values.

As two-phase material with an existing gas in pores as a second phase, porous ceramics find usage as furnace lining because of their good thermal resistance and good compressive strength. The pores contribute mainly to the stress concentration and fracture in the material [43-44]. Porosity plays a crucial role in the material structure. It accelerates the failure process and results in a decrease of the material strength [43, 45] . The main source of micro-crack initiation due to stress concentration is the existing pores in the material [44, 46], whereas further growth of micro cracks depends on the loading history. A precise defined content of initial porosity is necessary in many technical applications like thermal barrier coatings. The damage state, however, is developed due to the loading condition (e.g. mechanical, thermal, etc). It is because of the fact that many initial mechanical properties (Young's modulus, Poisson's ratio) of the porous media as a whole are influenced by porosity [47]. Based on the combination of the mesomechanical, phenomenological models and experimental data, Sadowski [46, 48-56] has investigated the mechanical response of porous ceramic under compression and tension as well as the development of damage in semi-brittle polycrystalline ceramics. The cracks in a polycrystal under loading spread mainly on the grain boundaries. This behavior leads to brittle macro failure at the end of loading. Sadowski applies a mesomechanical approach to study the physical aspects of damage initiation and damage growth in polycrystalline porous ceramics the moderate porosity (under 40%) and limited pore interactions. Taking into account the elastic deformation of porous material, the existence of shear dislocation bands and deformations connected with crack growth, constitutive equations were set up for a representative surface element (RSE) containing hexagonal grains under quasi-static

loading. The initial porosity was also assumed to be closed and distribute in grains or along grain boundaries. The phenomenological approach is for the global material behavior when the loading history is on hand. The experimental part consists of a procedure of loading–unloading–reloading with continuously increased loading level up to the rupture. Some characteristics like pore size and grain size as well as crack path and loading-rate effect were investigated by Sadowski using scanning electron microscopy (SEM). This combined approach was applied to two-phase (a matrix from Al2O3 and second phase ZrO2 up to 20% volume fraction) ceramic composite material under tension in his recent works [51]. Difficulties by creation of this ceramic composite are discussed as to be due to different thermal expansion coefficients of the constituents which result in the generation of a certain amount of microcracks and microporosity within the initial internal structure. Microscopic observations concerning grain shape and size, pore location, size and pore shape are needed in modeling as well as for the analysis of the fracture surface.

A series of works report on the mechanical strength distribution of highly porous ceramics in terms of Weibull, normal, Duxbury-Leath and Type I extreme value distibutions [57-64]. Length dependence of mechanical strength, determination of the effective volume and effective surfaces for testing samples by flexural tests, comparison of the fit of fracture strength to the distributions, modification of Weibull distributions for advanced reinforced composite ceramics and deviations from Weibull statistics are discussed there. Hosson [57] has used the acoustic emission method to characterize the failure of the highly porous ceramic under indirect tensile test. The amplitude of the distribution of the acoustic emission signal can be expressed in terms of material constants and depends on the energy-release rate of the material.

In the course of the correlation of porosity with the mechanical property of porous ceramics, various research works have been performed [65-69]. It is generally accepted that microstructural parameters like pore shape, distribution and orientation have influence on the correlation between mechanical property and porosity. Rossi and Rice [70-71] have presented approaches based on shape-stress concentration and

minimum solid area respectively. Rice [71] has studied the influence of stress concentration for the cases of isolated pores, pore-pore interactions and pore-crack interactions, and has questioned its role as a dominant factor for the mechanical properties-porosity correlations with the following finding; firstly, in case of isolated pores there is no consistency between the porosity dependence of the material and significant changes in maximum stress concentration with the stress state. Secondly, by pore-pore interaction, the stress concentration is considerably reduced due to the interaction of pore-stresses by decreasing pore spacing, which makes this concept unsuitable for high porosity ranges. Thirdly, in the case of pore-crack interaction, it is the crack which dominates the stress concentrations. Further, in a study based on comparison between stress concentration and minimum solid area [68] he shows the possible applicability of stress-concentration approach for the determination of elastic properties under compression, as well as the suitability of minimum solid area approach for mechanical property-porosity correlation. In an empirical approach, Boccaccini [67] has explicitly brought the maximum stress-concentration factor in the correlation as an exponent and predicted the fracture strength of porous ceramic with isolated pores and concluded that the calculation of stress concentration is appropriate for the cases like porous glasses with well-defined spheroidal pores at low to moderate range of porosity (< 40 % vol), under which no interaction should take place between pores. Ji et. al. [66] proposes a formula, known as General Mixture Rule (GMR), for the study of mechanical properties of porous materials in terms of the constituent's properties, porosity and microstructure. He has expressed the effects of microstructure by scaling fractal parameters, which indeed represents size distribution, shape, continuity and connectivity of the constituting phases. Considering porous solids, some mechanical property – porosity correlation equations like the one of Gibson-Ashby [72] and Phani expression [73] can be derived from this generalized formula [66]. Ji states further that the values of the scaling fractal parameters for properties like shear, Young's and bulk moduli as well as Poisson's ratio could be different for a porous solid with constant microstructure [66]. This promising approach still needs some physical validity and a profound analysis in

terms of mathematic mechanics due to its unclear physical meaning [66]. There are also approaches [74-76] which have studied computationally the influence of porosity and other microstructure features on the elastic properties of porous ceramic. Based on the finite-element method, Roberts [74] has studied the modulus of elasticity of different models with randomly distributed spherical pores, ellipsoidal pores and solid spheres and found independency between Poisson' ratio of the solid matrix and the modulus of elasticity of the models. Furthermore, he has found a convergence of Poisson's ratio to a fixed value for the models at high porosity, again independent from the matrix Poisson's ratio.

Another way to predict the influence of microstructure on the behavior of the composite materials (e.g. fiber reinforced, inclusion reinforced, and porous materials) is the multi-scale approach. Depending on the art of scale-transition, the multi-scale approach falls into four categories [77]. The first category deals with direct finite-element simulations of a unit cell with periodic microstructures or a representative-volume element; e.g. [78-80]. Transformation-field analysis (subcell method) forms the second category. This method uses subdivision of a representative-volume element into a number of subcells and then use the expression of traction and strain compatibility in terms of average stress and strain in each subcell [81-83]. The third method utilizes homogenization on the basis of an asymptotic expansion of the displacement field with the assumption of periodic microstructure. At the end it remains a unit cell problem which can be solved by finite element [84-85]. Finally, the fourth scale transition method is the mean-field homogenization based on assumed relations between average values of microstrain and stress fields in each phase [77], e.g [86-91]. The formulation of mean-field homogenization models is dependent on the mathematical structure of the constitutive equations of each phase of material [90]. Examples are homogenization models based on the Eshelby method [92] considering ellipsoidal inclusions, or other homogenization models with some assumptions which thus cannot describe some phenomena like clustering, percolation, strain localizations and grain size (when the Hall-Petch-Type relation [93-94] is not considered) [77]. Nevertheless, mean-field

homogenization is most the cost-effective solution in terms of computer time and the simplicity of use, when the conditions of applications of these models are met, and one is interested in the effective properties and per-phase averaged stress and strain [77]. Homogenization schemes like Voigt, Reuss, Mori-Tanaka, self-consistent model and double-inclusion model [95-96] are prominent schemes which have been developed within the framework of linear elasticity. Further extensions based on mean-field homogenization have been developed for the viscoelastic composites with coated inclusions [97], elasto-plastic reinforced composites with distributed-orientation [98], elasto-viscoplastic composites [99].

Several damage mechanisms of ceramics are discussed in the literature; sudden failure [45, 100], sub-critical crack growth [101-102], creep [100, 103-106], corrosion [107] and fatigue [108-109]. Damage extension in two ceramic refractory models with thermal expansion mismatch between the components have been studied at high temperature by Briche [110] with acoustic emission measurement technique as well as pulse ecography, and associated changes of elastic properties were observed. A good correlation was made between the findings from both methods. Fractographic results recognized the thermal shock as the prominent cause of more than one-third of all failures of ceramic components [111]. Contact failure is another typical failure mode of ceramics. Due to loading contact of hard surfaces, cracks can be initiated by exceeded stresses. Some relating works concerning thermal shock as well as contact failure of ceramics are [112-117].

Due to the particular mechanical behavior of ceramic materials like brittleness and low fracture strains, the experimental characterization of the material behavior at very high temperatures are complicated. Insufficiency of experimental data concerning high-temperature mechanical properties of insulating ceramics impedes the calibration and validation of the numerical models [100]. Therefore, there is still need of experimental and numerical research to fill the puzzle of mechanical behavior of highly porous ceramic materials under high-temperature applications.

2 Theoretical foundation

FRACTURE OF TECHNICAL CERAMIC MATERIALS

A profound description of fracture in ceramics can be found in numerous textbooks and papers [45, 101-103, 105, 107-109, 111, 113-116, 118-126] . It begins from discontinuities in the microstructure, in another word, small flaws. The size of the critical defect, which itself varies from component to component, changes the strength of the specimen and prerequisites a strength-distribution function as well as a large number of specimens for characterization of strength. Therefore, the statistical approach doesn't say if the structure is safe or unsafe, rather it shows if it has a certain probability of failure or survival. A zero failure probability points at a certainty by which the component contains no defect larger than a given size. For technical ceramics under typical design loads, the critical defect size is around 100 µm or smaller and therefore too small for a reliable detection by non-destructive techniques [111]. Microstructure, chemistry, material properties like toughness and type of loading are some factors influencing the fracture of ceramics. At room temperature, ceramics represent brittle fracture. The origin of fracture is a critical flaw with a crack-like behavior. In a tensile test, at the beginning of crack extension, the crack path is perpendicular to the first principal stress. The size of the fracture origin and of the areas around it (mirror, mist and hackle) is proportional to the inverse square of the stress in an uncracked body at the position of fracture origin. In operation, however, the stress is generally not uniaxial and thus an intricate crack path may be observed. The initial picture of fracture may be confused due to secondary damage.

Thermal shock and contact loading are two major failure modes in operation. Occurrence of thermal shock is due to the temperature difference and thermal strains in a component resulted by a rapid temperature change. Constrained thermal strains culminate in increased thermal stress which benefits crack propagation and failure. The boundary conditions here define the shape of the stress fields. Examples of thermal shock can be

observed by quenching a hot part or soldering a resistor. In the former case, there is a rapid heat transfer from the component's surface to the environment. While the surface is cooling down quickly and the material in the surface shrinks, the material's interior is still at high temperature and acts as constraint and impedes the surface shrinkage. As a result, the surface suffers from tensile stress and the interior, consequently, undergoes compression condition. Thermal shock damage occurs when the major tensile stress exceeds a critical value. This associates with a characteristic crack pattern. The further development of thermal shock cracks depend on how critical the local stresses are. The crack growth, in a direction opposite to the heat flow, reduces the tensile stress in the surrounding and consequent crack propagation may be stopped. At outer edges, thermal shock cracks run perpendicular to the surface. Though, at flat surfaces of thin plates they tend to a pattern like the mud cracking patterns in dried-up areas.

Cracking can also occur due to the exceeding of a critical stress value in loading contact of hard surfaces. Examples of loading contact are static or dynamic impingements of bodies. This can be either area loading (blunt contact) or point loading (sharp contact). By blunt contact, a classic scenario when surfaces of two bodies (e.g., a sphere and a flat body) touch, an elastic deformation takes place and a circular contact area appears. Consequently, compression stresses arise under this contact area. The amplitude of compression stresses is a function of the elastic properties of the two surfaces. The region around the contact zone gets under tensile stress. Cracks form in this region if tensile stresses exceed a certain critical value. For sphere and flat surface contact, the region under tensile stresses is ring shaped and the crack is called ring shape crack or Hertzian ring crack. The depth of crack penetration depends on the increase in loading, sine to the occurrence of the crack the tensile stresses decrease under the surface. The cause of such crack formation lies generally in an inappropriate handling or in local overloading of the material.

The sharp contact scenario is well described by sharp indentation techniques like Vickers testing. Radial cracks are formed at any sharp features due to the plastic deformation under the contact point. Development of cracking and damage are under the influence of

internal stresses produced by inelastic strain. Beside the radial cracks, lateral cracks may form in this region and extend parallel to the surface and perpendicular to radial cracks. Intersection of these both cracks may cause fragmentations of the material. Considering the friction and wear of ceramics, this phenomenon is the most prolific wear mechanism. Contact failure can also be observed when two bodies touch near an edge. In this case, the crack may not stop and eventually a flake of material breaks out. Examples for such edge breaking can be seen in tooth implants, human teeth or tool bits. As contact damage may result in an immediate failure, it can also serve as the origin of some delayed failure due to subsequent cracks with steady or fast growth rate.

In brittle fracture, which occurs at room and ambient temperature, there is no significant plastic deformation and the elastic strain is very small. Ductile fracture, however, occurs at very high temperature or at very slow deformation rates. Damage mechanisms fall into the following categories:

- Sudden catastrophic failure
- Sub-critical crack growth
- Fatigue
- Creep
- Corrosion (or oxidation)

Sudden catastrophic failure is the most observed damage mechanism in technical ceramics. It is also the last stage of failure in the material and is caused by quick growth of the critical crack. Due to high growth rate, crack arrest is not possible and thus fracture of the component occurs immediately after the application of the critical load. Examples of critical cracks are generated flaws during ceramic production, by machining and inappropriate handling of the components, contact damage and thermal shock. In case of small cracks, other mechanisms like sub-critical crack growth, fatigue, creep and oxidation contribute to the crack growth to a critical size. The component's service life time depends then on the time of crack growth to the critical size, after which the sudden catastrophic failure occurs.

Sub-critical crack growth is intrigued due to the thermal activation of bond breaking at the tip of a stressed crack. Corrosive action of some polar molecules helps this mechanism and is, therefore, related to the stress corrosion cracking. Precedence of sudden catastrophic failure due to sub-critical crack growth is dependent on how the load is applied. Further, sub-critical crack growth results in delayed failure, i.e., failure of the component long time after the application of the load without any plastic deformation.

Fatigue crack growth in ceramics is due to the cyclical damage of microstructural elements which may precede the sudden catastrophic failure. Breaking of crack bridges during the crack-closure part of a loading is an example of this case. Like sub-critical crack growth, fatigue-crack growth can cause also delayed failure of components.

Creep of ceramics is not that much prominent in comparison to metals and polymers. The reason is the higher activation energy for creep in ceramics which will be possible only at very high temperatures associated with the melting temperature of ceramics. In general, the process of pore generation and further pore growth through coalescence of pores is the main cause of creep damage. Unlike crack growth, creep damage is not localized and may occur overall in a component. Whether the fracture is brittle or ductile, it is determined by the acting stress and temperature.

Corrosion (or oxidation) damage is an important wear mechanism in ceramics and acts as initiation stages of crack growth and consequent fracture. Gaseous products in corrosion can lead to material loss. Besides, oxidation of grain boundaries may cause material disintegration.

In the following section, three dimensional rupture criterion is described for the case of sudden catastrophic failure of sound-absorbing porous ceramics.

A RECOURSE TO DAMAGE MECHANICS

Brittle damage reminds generally of materials like ceramics, concrete or high strength quenched steels. In damage mechanics, damage growth is proportional to plastic

dissipation. Brittle damage is caused by decohesion without any measurable plastic strain at the mesoscale [127]. At microscale, however, damage is a localized phenomenon and hence some plastic strains occur in very small damaged volumes (e.g., slips at grain boundaries or interfaces). Depending on whether these strains are taken into account or not, the brittle damage are categorized to pure brittle and quasi-brittle damage.

Rupture criterion

At the mesoscale, rupture can be understood as a crack propagation which occupies the entire intersection of the representative volume element and is caused mainly by an instability process. The instability process induces decohesion of atoms in the remaining resisting area [127]. The final stage of decohesion is associated with a critical effective stress σ_∞

$$\sigma_\infty = \frac{\sigma}{1 - D_c} \tag{2.1}$$

which acts on this area and is the maximum applicable stress to the material. D_c is the critical value of the damage and σ is the unidimensional stress. In practice, ultimate stress σ_u (a material characteristic) is used as an approximation of this critical effective stress which is smaller in value and identified as a material characteristic. Substitution of ultimate stress gives [127]

$$D_c \simeq 1 - \frac{\sigma}{\sigma_u} \tag{2.2}$$

for the critical value of the damage. In the case of a pure monotonic tension test, this relation takes the form [127]

$$D_{1c} \simeq 1 - \frac{\sigma_R}{\sigma_u} \tag{2.3}$$

Where σ_R is the rupture stress and D_{1c} is the critical damage corresponding to uniaxial tension which plays the role of a reference value.

Damage equivalent stress criterion

The strain-energy density release rate (Y) serves as a principal variable in the phenomenon of damage and is defined by [127]

$$Y = \frac{\omega_e}{1 - D} \tag{2.4}$$

where ω_e is the elastic strain-energy density and D is the damage variable. It has been also given the meaning of an equivalent stress. The law of elasticity with consideration of damage is

$$\sigma_{ij} = a_{ijkl}\varepsilon_{kl}^{e}(1 - D) \tag{2.5}$$

where a_{ijkl} , σ_{ij}, ε_{kl}^{e} are, respectively, the elastic tensor, stress and strain tensors. Accordingly, the elastic strain-energy density is obtained by integration of the law of elasticity over a unit volume (considering D=const) as following:

$$\omega_e = \frac{1}{2} a_{ijkl}\varepsilon_{ij}^{e}\varepsilon_{kl}^{e}(1 - D) \tag{2.6}$$

Reformulation of the elastic strain energy density in terms of the shear and the hydrostatic strain energy is

$$\omega_e = \int \sigma_{ij} d\varepsilon_{ij}^{e} = \int \sigma_{ij}^{D} d\varepsilon_{ij}^{e} + \delta_{ij}\delta_{ij} \int \sigma_H d\varepsilon_H^{e} \tag{2.7}$$

where D und H stand for deviatoric and hydrostatic part of the stress and strain tensors. Considering the law of linear isotropic elasticity coupled with damage and substituting the deviatoric and hydrostatic strains for the stress terms, the elastic strain energy obtains the following form

$$\omega_e = \frac{1}{2}\left(\frac{1 + \nu}{E}\frac{\sigma_{ij}^{D}\sigma_{ij}^{D}}{1 - D} + 3\frac{1 - 2\nu}{E}\frac{\sigma_H^2}{1 - D}\right) \tag{2.8}$$

in which ν stands for Poisson's ratio. Reformulation of the equation (2.8) shows a term of von Mises equivalent stress, ($\sigma_{eq} = \left(\frac{3}{2}\sigma_{ij}^{D}\sigma_{ij}^{D}\right)^{1/2}$). Factoring it out and substituting ω_e leads to another definition of Y :

$$Y = \frac{\omega_e}{1-D} = \frac{{\sigma_{eq}}^2}{2E(1-D)^2}\left[\frac{2}{3}(1+\nu) + 3(1-2\nu)\left(\frac{\sigma_H}{\sigma_{eq}}\right)^2\right]. \quad (2.9)$$

The term $\frac{\sigma_H}{\sigma_{eq}}$ is called triaxiality ratio and is a measure of ductility at fracture. High triaxiality makes materials brittle [127]. Consequently the triaxiality function is defined [127]

$$R_\nu = \left[\frac{2}{3}(1+\nu) + 3(1-2\nu)\left(\frac{\sigma_H}{\sigma_{eq}}\right)^2\right]. \quad (2.10)$$

Subsequently, the damage equivalent stress is expressed as

$$\sigma^* = \sigma_{eq} R_\nu^{1/2} \quad (2.11)$$

which differs from von Mises equivalent stress by the triaxiality function. The triaxiality contributes to the debonding which causes damage. The lateral contaction behavior expressed by Poisson's ratio serves considerably to this phenomenon. A decrease of this ratio results in an increase of triaxiality and thus increases brittleness at fracture.

Three dimensional rupture criterion

The rupture criterion in three dimensions is a generalization the aforementioned rupture criterion in the one-dimensional case based on the damage equivalent-stress criterion [127]. It's derivation starts with the study of the stability condition of damage processes. The non-positive evolution of the kinetic-energy density k is defined as [127]

$$\dot{k} \leq 0 \quad (2.12)$$

and the first principle of thermodynamics as

$$\dot{e} + \dot{k} = p_x + Q - Y_c \dot{D} \quad (2.13)$$

where $\dot{e}$, p_x, Q and $-Y_c\dot{D}$ are, respectively, the internal energy-density rate, external force power density, heat rate and the dissipated power for creation of new micro free surfaces. The latter serves as a boundary variable and is also a material characteristic. With the assumptions of the brittle stage of instability as well as neglecting the inertia forces, where $\dot{k}$ approaches zero, one may express $\dot{e}$ and $p_x$as [127]

$$\dot{e} = \dot{\omega}_e + Q \tag{2.14}$$

$$p_x = \sigma_{ij}\dot{\varepsilon}_{ij} = \sigma_{ij}\dot{\varepsilon}^e_{ij} \tag{2.15}$$

where

$$\dot{\omega}_e = a_{ijkl}\varepsilon^e_{ij}\dot{\varepsilon}^e_{kl}(1-D) - \frac{1}{2}a_{ijkl}\varepsilon^e_{ij}\varepsilon^e_{kl}\dot{D} = \sigma_{kl}\dot{\varepsilon}^e_{kl} - Y\dot{D} \tag{2.16}$$

with

$$\sigma_{kl} = a_{ijkl}\varepsilon^e_{ij}(1-D) \tag{2.17}$$

considering the law of elasticity coupled with damage and the driving force

$$Y = \frac{1}{2}a_{ijkl}\varepsilon^e_{ij}\varepsilon^e_{kl}\ . \tag{2.18}$$

Substituting all terms in the inequality (2.12) delivers

$$\dot{k} = \sigma_{ij}\dot{\varepsilon}^e_{ij} - \sigma_{kl}\dot{\varepsilon}^e_{kl} + Y\dot{D} - Y_c\dot{D} \leq 0\ . \tag{2.19}$$

Reminding that $\dot{D}$ is always positive, the stability condition is obtained as

$$Y - Y_c \leq 0 \tag{2.20}$$

and subsequently the instability criterion as

$$Y \geq Y_c\ . \tag{2.21}$$

This criterion physically states that instability is imminent when the released energy due to the stiffness loss becomes equal or greater than the required energy for creation of new damage surfaces. The occurrence of instability does not necessarily mean rupture (exception is pure brittle damage). It is because of the fact that during instability prior to failure the value of the energy-density-release rate is almost constant. The rupture criterion is then defined by lining up the amount of energy dissipated in damage growth at the final stage of damage rupture for the one-dimensional reference case and three-dimensional case as following [127]

$$\frac{\tilde{\sigma}^{*2}}{2E}D_c = \frac{\sigma_u^2}{2E}D_{1c}\ . \tag{2.22}$$

With the limitation of D_c to 1, the rupture criterion gives the critical value of the damage as a function of the one-dimensional reference value D_{1c} as well as the effective damage equivalent stress $\tilde{\sigma}^{*2}$ and the ultimate stress

$$D_c = D_{1c}\frac{\sigma_u^2}{\tilde{\sigma}^{*2}} \leq 1 \ . \tag{2.23}$$

Pure brittle damage

Pure brittle damage refers either to the absence of plastic strains or to neglecting the permanent micro strains. In both cases, the general law of kinetic damage considers the damage as zero and, therefore, the stability criterion becomes simultaneously the rupture criterion. Pure brittle rupture occurs for [127]

$$Y = Y_c = \frac{\sigma_\infty^2}{2E} \simeq \frac{\sigma_u^2}{2E} \tag{2.24}$$

or

$$Y = \frac{\sigma^{*2}}{2E} = \frac{\sigma_u^2}{2E} \tag{2.25}$$

with $D = 0$, where

$$\sigma^* = \sigma_{eq} R_v^{1/2} = \sigma_u \ . \tag{2.26}$$

As a material characteristic, σ_u is the stress to rupture in a one-dimensional tension tests.

MULTISCALE APPROACH FOR PROPERTY PREDICTION

The raison d'être of multiscale approaches is the study and prediction of the interaction between the microstructure and the body's properties. At micro scale, it is quite complex to solve the mechanical problem computationally. It is needed to define interaction and contact relations to catch the coupling mechanisms at the internal interfaces [27]. Through multiscale approach at macro scale, each integration point is assumed to be a representative volume element (RVE) which contains at micro scale a finite number of components. This representative volume element is small enough with respect to the solid body and large enough to be able to represent the heterogeneous microstructure. At micro scale, a constitutive model is applied for each constituent, whereas at macro scale, continuum mechanics with macro constitutive equations are

implemented. The transition from micro and macro is accomplished by homogenization. In linear elasticity, the aim of homogenization is to find an equivalent homogeneous material with the same stiffness of the real composite under the same boundary conditions. Regarding this, a number of scale transition methods can be mentioned [77]: direct finite element analysis of a unit cell with periodic microstructures or a representative volume element [78-80], transformation field analysis or subcell method which subdivides a representative volume element into a number of subcells and then express a traction and strain compatibility in terms of average stress and strain in each subcell [81-83], homogenization on the basis of a asymptotic expansion of the displacement field with assumption of periodic microstructure [84-85] and the mean-field homogenization based on assumed relations between average values of microstrain and stress fields in each phase [86-91].

In this work, the direct finite-element analysis at micro scale has been applied in chapter four to different RVE's in order to study the micro fields in a detailed general manner. For a complex or realistic microstructure, however, one should make a compromise to reach a good mesh and suitable computation time. Furthermore, for the finite-element analysis of a realistic structure at macro scale, which is coupled with a RVE at each integration point, this approach is not practical. Beside direct finite element analysis of a RVE, mean-field homogenization models has been used in chapter three to predict the macroscopic properties of porous sound absorbing ceramic with respect to its microstructure. In the following, some aspects of mean-field homogenization for linear elastic composites are briefly described. For further cases like linear thermoelastic, linear viscoelastic and elastoviscoplastic composites one may refer to the following refrences [91, 95, 97-99, 128-132].

The mean-field homogenization delivers an accurate approximation of the volume average of the stress and strain fields, which means macro stresses and strains both at RVE level as well as in each phase, but it does not compute the detailed micro stress and strain fields in each phase. Let's assume a two phase composite containing matrix material (subscripted by 0) and a number of inclusions (subscripted by 1). The inclusions

(*I*) are assumed to be all identical with the same material, shape and orientation. Then, the volume fractions can be written as $\nu_0 + \nu_1 = 1$. The volume averages of strain filed over the RVE are expressed as [95, 133]

$$\langle \varepsilon \rangle_\omega = \nu_0 \langle \varepsilon \rangle_{\omega_0} + \nu_1 \langle \varepsilon \rangle_{\omega_1} \tag{2.27}$$

which holds also for any other micro fields, e.g., stress field. The strain concentration tensors are defined based on equation (2.27) as

$$\langle \varepsilon \rangle_{\omega_1} = \mathbf{B}^{\boldsymbol{\varepsilon}} : \langle \varepsilon \rangle_{\omega_0} \quad , \quad \langle \varepsilon \rangle_{\omega_1} = \mathbf{A}^{\boldsymbol{\varepsilon}} : \langle \varepsilon \rangle_{\omega} \ . \tag{2.28}$$

It means that the volume average of strain over all inclusions is in relation to the volume average of strain over the matrix phase through the tensor $\mathbf{B}$ as well as the volume average of strain over the whole RVE through the tensor $\mathbf{A}$. The second tensor can also be expressed as a function of the first tensor as following

$$\mathbf{A}^{\boldsymbol{\varepsilon}} = \mathbf{B}^{\boldsymbol{\varepsilon}} : [\nu_1 \mathbf{B}^{\boldsymbol{\varepsilon}} + (\mathbf{1} - \nu_1)\mathbf{I}]^{-\mathbf{1}} \tag{2.29}$$

which is again applicable for any material model for each phase. Considering linear elastic behavior, the stiffness as macro scale is

$$\bar{\mathbf{C}} = [\nu_1 \mathbf{C}_1 : \mathbf{B}^{\boldsymbol{\varepsilon}} + (\mathbf{1} - \nu_1)\mathbf{C_0}] : [\nu_1 \mathbf{B}^{\boldsymbol{\varepsilon}} + (\mathbf{1} - \nu_1)\mathbf{I}]^{-\mathbf{1}} \ . \tag{2.30}$$

Two simple mean-field homogenization models are the Voigt model and the Reuss model. By Voigt model, the strain field and by Reuss model the stress field is assumed to be uniform inside the RVE. As a consequent, macro stiffness and macro compliance are defined in Voigt and Reuss model as the volume average of micro stiffness and the volume average of micro compliance, respectively. Voigt model generalizes the one dimensional model of bars in parallel, and Reuss model does the same but in series. Considering both Voigt and Reuss model, the first strain concentration tensor is defined for both respectively

$$\mathbf{B}^{\boldsymbol{\varepsilon}} = \mathbf{I} \quad \text{and} \quad \mathbf{B}^{\boldsymbol{\varepsilon}} = {\mathbf{C}_1}^{-1} : \mathbf{C}_0 \ . \tag{2.31}$$

For a real composite's stiffness, Voigt and Reuss estimates result in far-apart upper and lower bound, respectively. Their simple assumptions are not realistic for a real composite. Other mean-field homogenization models with closer bounds are based on the Eshelby method [92]. Eshelby studied the case of an infinite solid body with uniform

stiffness from which an ellipsoidal volume is cut out. The volume experiences an eigenstrain and then is welded back into the same cavity. Results state that the strain in the ellipsoidal volume is uniform and in relation to the eigenstrain ε^* [133]

$$\varepsilon(\mathbf{x}) = \zeta(I, \mathbf{C_0}) : \varepsilon^* \, , \forall \mathbf{x} \in (I) \tag{2.32}$$

where $\zeta(I, \mathbf{C_0})$ is the Eshelby's tensor and $\mathbf{C_0}$ the uniform stiffness of the solid body. The strain depends not only on the uniform stiffness, but also on the shape and orientation of the inclusion (I). For an isotropic body and a spheroid, dependence on the stiffness and the shape is governed by Poisson's ratio and the aspect ratio. Eshelby's solution paves the way for the single inclusion problem which is the fundament of the important mean-field homogenization models. It takes an infinite solid body (uniform stiffness $\mathbf{C}_0$) with an ellipsoidal inclusion (uniform stiffness $\mathbf{C_1}$) and studies the strain inside the inclusion, when the body undergoes linear displacements on the boundaries. The displacements correspond to a uniform remote strain $\mathbf{E}$. Based on Eshelby's solution, the strain within the inclusion is [133]

$$\varepsilon(\mathbf{x}) = \mathbf{H}^{\varepsilon}(I, \mathbf{C_0}, \mathbf{C_1}) : \mathbf{E} \quad , \qquad \forall \mathbf{x} \in (I) \tag{2.33}$$

with

$$\mathbf{H}^{\varepsilon}(I, \mathbf{C_0}, \mathbf{C_1}) = \{\mathbf{I} + \zeta(I, \mathbf{C_0}) : \mathbf{C_0^{-1}} : [\mathbf{C_1} - \mathbf{C_0}]\}^{-1} \tag{2.34}$$

as the single inclusion strain concentration tensor. The term $\zeta(I, \mathbf{C_0}) : \mathbf{C_0^{-1}}$ in equation (2.34) is Hill's polarization tensor [133]

$$\mathbf{P}^{\varepsilon} = \zeta(I, \mathbf{C_0}) : \mathbf{C_0^{-1}} \, . \tag{2.35}$$

Based on the solution of the single-inclusion problem several mean-field homogenization methods, each with different assumptions, are developed for multi-inclusion problems. Examples are self-consistent model [86], Mori-Tanaka model [96], double-inclusion model [134]. The self-consistent model is applicable to general composite materials as well as to the aggregates and polycrystals. The model assumes that a modified matrix with the same stiffness as the unknown stiffness $\bar{\mathbf{C}}$ exists and each inclusion behaves as an isolated one in this matrix. The body is then subjected to the remote strain $\mathbf{E}$. Subsequently, the strain in each inclusion (I) of the RVE is [133]

$$\varepsilon(\mathbf{x}) = \mathbf{H}^{\varepsilon}(I, \bar{\mathbf{C}}, \mathbf{C_1}) : \mathbf{E} \quad , \ \forall \mathbf{x} \in (I) \ . \tag{2.36}$$

Its prediction, however, is not satisfactory, when applied to composites with constituents having different material properties [135].

Based on Eshelby's solution, Mori and Tanaka [96] found that the strain concentration tensor relates the volume average of strain over all inclusions to the mean matrix strain as [133]

$$\mathbf{B^{\varepsilon}} = \mathbf{H}^{\varepsilon}(I, \mathbf{C_0}, \mathbf{C_1}) \quad . \tag{2.37}$$

This is the strain concentration tensor of the single inclusion problem. In other words [136], the behavior of each inclusion in the real RVE is like the one of an isolated inclusion in an assumed infinite matrix subjected to the average matrix strains in the real RVE as the far field remote strains.

The double-inclusion model [134] assumes that in a reference medium (stiffness $\mathbf{C_r}$) each inclusion (stiffness $\mathbf{C_1}$) is surrounded, close to the inclusion, with the real matrix material (stiffness $\mathbf{C_0}$). Therefore, the RVE has to be understood as a model composite with reference matrix and embedded inclusions with coatings. Accordingly, the volumes and volume fractions are in relation with each other [133]

$$\frac{V(I)}{V(I_0)} \geq \frac{\nu_1}{1-\nu_1} \quad . \tag{2.38}$$

Based on double-inclusion model, the interpolative double-inclusion model is proposed by Lielens [133, 137]

$$\mathbf{B^{\varepsilon}} = [(1 - \xi(\nu_1))(\mathbf{B}_l^{\varepsilon})^{-1} + \xi(\nu_1)(\mathbf{B}_u^{\varepsilon})^{-1}] \tag{2.39}$$

$$\text{with } \mathbf{B}_l^{\varepsilon} \equiv \mathbf{H}^{\varepsilon}(I, \mathbf{C_0}, \mathbf{C_1}) \quad , \quad \mathbf{B}_u^{\varepsilon} \equiv [\mathbf{H}^{\varepsilon}(I, \mathbf{C_1}, \mathbf{C_0})]^{-1}. \tag{2.40}$$

It interpolates between the estimations of Mori-Tanaka and inverse Mori-Tanaka model, which is obtained by inverting material properties between the matrix and the inclusion phases.

The aforementioned models are based on the cases of two-phase composites with identical inclusions and aligned orientations. Considering the composite with inclusions of different orientations or materials, three approaches can be mentioned: two-step method [137], two-level method [97] and multi-inclusion [134]. A general method which

is not also restricted to misaligned inclusions (described with an orientation field) is two-step method. According to this method, the RVE is at first step decomposed into a set of pseudo-grains. Each pseudo-grain is the two-phase composite itself with identical inclusions and aligned orientations. Then, the homogenization is performed after a scheme like Mori-Tanaka or double-inclusions. The second step is performed by homogenization of the homogenized pseudo-grains following a Voigt like scheme. Although the Voigt model is not appropriate for a real composite, delivers good prediction for the homogenized pseudo-grains as aggregate in comparison to Mori-Tanaka [97]. Another homogenization procedure is the two-level method which is based on nested homogenization models. It is a two-level recursive application of homogenization. Let's consider a composite having a matrix and coated inclusions. Each inclusion with coating is considered as a two-phase composite (deep level). When the two-phase composite is homogenized, it serves as a homogeneous reinforcement for the matrix (high level). At both levels a homogenization scheme (double-inclusion, Mori-Tanaka or interpolative double-inclusion) is needed. For a comparative study regarding the differences of the aforementioned procedures and combination of different schemes at each level or step as well as examples, one may refer to [97-98, 132].

The next chapter introduces the porous sound absorbing ceramic and its production technique, followed by mechanical and thermal characterizations, and failure statistics. Finally, with the help of micromechanical modeling based on the mean-field homogenization method, elastic material properties are predicted for different material porosities, pore form and orientations.

3 Material Characterization and Modeling

EXPERIMENTAL OUTLINE

Before investigating the mechanical behavior of the material, the ceramic under study must be characterized through a series of experiments and measurements. Subsequently, the required material parameters can be determined from experimental data. They are considered as initial state parameters in numerical investigations, since material parameters can vary during physical processes. As an example, the permeability of a porous material can change, if large deformations occur.

In case of porous materials, the material parameters must be available for constituents, matrix and inclusions (or rather pores). However, it is very complicated to determine the properties of each constituent from experiments. Depending on the experimental procedure, either the properties of the composite or the properties of one constituent are determined. As a resolution for this discrepancy, the required properties are calculated in this chapter with the use of material modeling. In the wake of this calculation, several porous ceramic structures are studied, with various volume fractions, pore form, fully aligned or randomly oriented pores in 3D or 2D. The aim of this study is the estimation of the elastic properties of porous sound-absorbing ceramic.

The experimental data determined in this chapter are technically limited to the existing equipment in the framework of the co-operations within the Graduate School PoreNet. A general overview of the material properties, the chosen measuring methods and the laboratory equipment is listed in Table 3.1.

Table 3.1. General overview of the measuring method and equipment

Properties	Measuring method / equipment	Limitation
Density / Porosity	Helium pycnometry, Archimedes method	Sample geometry
Modulus of elasticity	Compressive test	Sample geometry for high temperature tests
Modulus of rupture	Four-point-bending test	Representative geometry
Thermal expansion coefficient	Dilatometer	1300°C
Specific heat capacity	Differential scanning calorimetry	200°C
Thermal conductivity	Transient Hot Bridge	Room temperature

The technical limitations mentioned here are all discussed in the following. This chapter is divided into three parts. In the first one, the processing technique to produce the test specimen is introduced. The second part describes the tests carried out to obtain mechanical and thermal properties of the ceramics. In the third part a comprehensive study of the material properties by means of material modeling is reported.

PREPARATION OF SPECIMEN

The material processing technique used in this work is introduced by Giese [138], based on the freeze gelation process [139-141]. It uses a wide range of advantages of freeze gelation, with regard to production and application of ceramic sound absorbers, over other procedures such as injection molding and gel casting. On one hand, toxic additives, high pressure components and high binder contents are avoided by this process

[140]. On the other hand, this procedure is cost-effective and environmental friendly [142-143] due to the use of simple equipments, being water-based and excellent capabilities of forming and consolidation. It also inherently provides control over the characteristics of the porosity being generated during the process. Freezing of aqueous sols or powder, characterized by nucleation and growth of ice crystal, makes it possible to control shape, size, local distribution and also orientation of pores, left behind after elimination of the solvent. Moreover, high green body stiffness, low shrinkage and a laminar open-pored structure with high connectivity are achievable by freeze gelation.

Originally, freeze gelation was developed as a near net shape forming technique to produce dense ceramic parts which presented finely the mould details [142]. Since the generated pores, considered as large size defects, were unwelcome for ceramic applications, a great amount of effort has first been put into controlling or avoiding the formation of ice crystals. Later on, it was discovered that the controlled formation and growth of the ice crystal would be beneficial for producing a porous ceramic with specific porosity [143]. The technique consists of four fundamental steps: preparing and freezing a liquid suspension (aqueous or not), sublimation of the solidified phase from the solid to the gas state under reduced pressure and sintering. While freezing, the solidification front moves in the freezing direction and reject the particles in suspension in the slurry, which makes them piling up between the growing crystals. The principle of freeze gelation relies merely on the physical rather than chemical interactions [141]. The described phenomenon is alike the one in the unidirectional solidification of cast materials and binary alloys, in which powders with small particle size are used and the solvent plays the role of fugitive second phase. Following, the whole preparation procedure is discussed in details (Fig. 3.1).

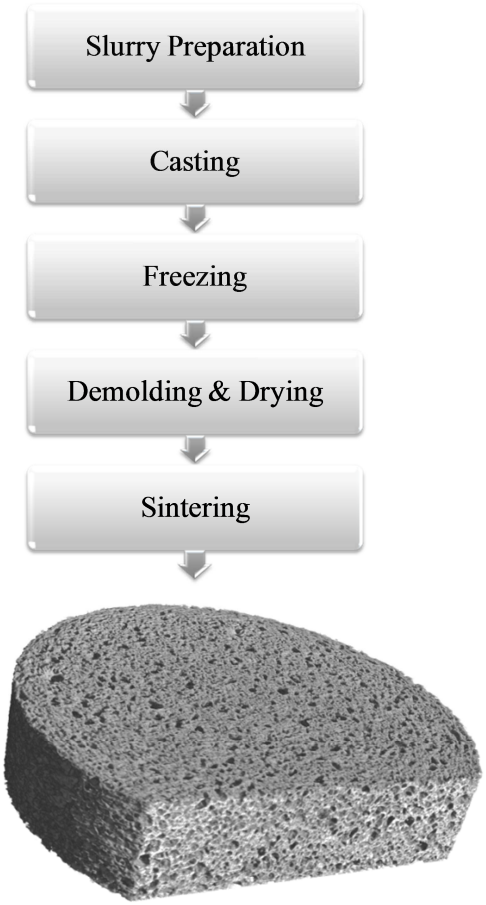

Fig. 3.1 Flow chart of the specimen preparation procedure; CT scan [138]

The preparation of aslurry here is similar to that of conventional processing routes like slip casting. The ceramic powders Alumina (Al_2O_3 , Alcoa: CT3000SG, particle size: 500-800nm) and Mullite ($3Al_2O_3 \cdot 2SiO_2$, Treibacher, Alodur® WFM, particle size: 0-45μm, -325mesh) are stirred into the solvent, a mixture of distilled water, silica sol (30w% of colloidal SiO_2 , BegoSol® K, particle size: 8nm, Bego, Bremen Germany) and a dispersant (polyacrylic acid). The temperature of the slurry should be adjusted to

the temperature, in which the solvent is liquid. In this care, the slurry is prepared at room temperature. The solid loading used in the slurry is set to 45% vol. It is for stabilizing the suspension and to avoid segregation phenomenon during the freezing process which leads to gradient density and porosity in the material.

In order to increase the total porosity, expanded perlite as pore-forming filler is employed. Expanded perlite is a glassy light material with a volcanic origin. Due to some outstanding properties such as high porosity, high thermal insulation, chemical inertness and fire resistance, it has found a great range of applications like filtration, sound absorption and thermal insulation. The expanded perlite grains, size range from 0.1 to 4 mm, are all coated by the manufacturer with paraffin resin to repel the hydrosol. The grains were added then to the suspension volumetric ratio of 1.8, yielding a viscous mixture.

The freezing process is an important stage of the whole process, because it determines the structure and the characteristics of the future porosity. During the freezing, ice crystals are formed and build an ice-front in the slurry, rejecting the solid particles and make them concentrate and being entrapped in-between. Hence, the morphology of the ice front determines the architecture of the material at the end. Here, the slurry was casted in aluminum molds, which underwent almost isotropic cooling at -150°C with a slow cooling rate of 0.384 K/minute to induce homogeneous solidification and to minimize the boundary effects due to sharp temperature gradients close to the mold surface.

Subsequently, the specimens are demolded and dried in ambient conditions. Under these conditions, the frozen solvent is converted into the gas state, which delivers the first type of pores where the solvent crystals were. This stage must be carried out deliberately to avoid any formation of defects during the phase transition, especially in large specimens. After overnight drying, green bodies with enough strength for handling or machining are obtained. The process-related surface effects are avoided here by removing a 2 mm layer from the surface by careful turning.

At the final stage, the green bodies are sintered for 5 hours at 1600°C during which the expanded perlite particles melt at 900°C. A sintering shrinkage of almost 2% was observed by the specimen. Thus, the second type of pores is gained by penetrating the melting expanded perlite grains in the matrix and the first level pores. The cross section of the specimen and the rendered µ-CT scan of the specimen are depicted in Fig. 3.2.

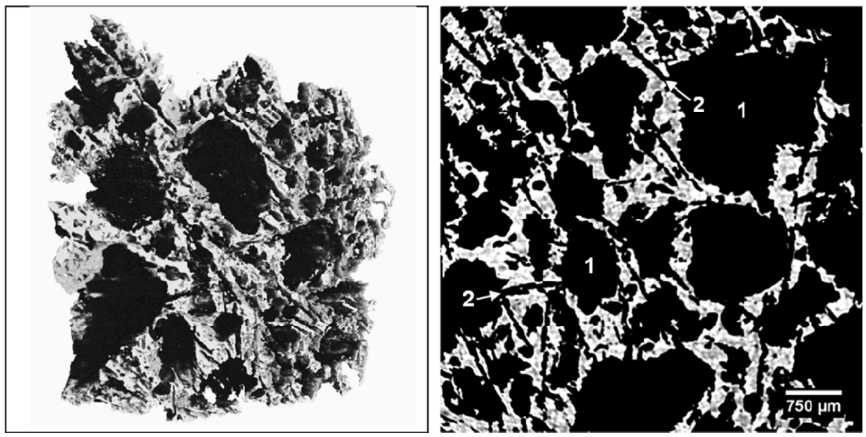

Fig. 3.2. Rendered µ-CT scan (left) and the cross section of the specimen (right) [138]

The dark zones in the right picture, numbered with 1, represent the second type of pores generated through the melting of expanded perlite, whereas the acicular shapes numbered with 2, point at the first type of pores generated by sublimation during the process. The latter have a width of approximately 40 µm and a mean length of 285 µm, far smaller than the former with the size of the raw material. A microstructure analysis of 520 cross section µ-CT scans for pores with an acicular shape gives a porosity of 16% (± 5%). This results from the permeation of the melted perlite in the small acicular pores. The increase of solid loading results in almost complete elimination of the acicular pores, and as a result a reduction of the connectivity of the second type of pores [138]. Therefore, it is essential to optimize the solid loading in order to get a well open-pored structure for effective sound absorption.

This preparation method with the described amount of ingredients delivers a porous ceramic with an open porosity of 74% (measured by Archimedes method) and

skeletal density of 3148 Kg/m^3 (measured by Hellium Pycnometry). The mass density with 74% porosity is measured 732 Kg/m^3.

It is generally accepted that by freeze casting [141], each stage of processing, namely slurry formulation and preparation, solidification and sintering, affect the final structure of the porous ceramics. Among these stages, solidification proves to be very critical with respect to the final structure. Most porosity features like eutectic growth are created during this stage. Control of the porosity features in terms of the regularity and size of the pattern are important issues which affect the final properties of the structure. For the formation of the porous structure, the particles, suspended in the slurry, must be rejected by moving the solidification front and then entrapped between the ice crystals. The main physical parameters affecting this interaction between the solvent solidification front and the particles in suspension are the viscosity of the liquid, the particle size, the thickness of the liquid film (existing between the solidification front and the particles for transporting the molecules towards the growing crystals), and the change of the surface energy. Beside the particle size, other parameters such as particle shape, particle distribution, surface roughness and surface tension could also have influence on this interaction. The morphology of the solidification front is a key issue which determines the architecture of the final material. It must be non-planar; otherwise the particles are collected after the solidification on one side of the sample. During solidification, the front takes different morphologies due to the different triggering mechanisms, namely inherent thermodynamic instability of the interface and reversal of the thermal gradient induced by the particles. Further influencing parameters during the solidification stage are the solidification kinetics and the temperature gradient. An increased speed of solidification front speed results in a fine final microstructure, whereas the temperature gradient governs the directionality of the desired porosity. For certain effects, such as modification of the porosity morphology or modification of the interaction between the solidification front and the particles, additives can also be used in the slurry formula. These additives likely affect some properties such as viscosity and surface tension. In order to achieve a homogeneous structure in the sintered material, it is essential to avoid any segregation

effects and that the slurry remains stable over the solidification stage. The particle size has also great influence on this homogeneity. The size similarity between the particles and the solvent crystals hampers the replication of the crystal details in the final structure. In case of large particles, the velocity of the solidification front is proportionally decreased and the process of building fine microstructure cannot be accomplished [141].

DETERMINATION OF THE MECHANICAL PROPERTIES

This section describes the mechanical strength of porous sound absorbers by performing four-point bending tests at room temperature as well as running a series of compressive tests at both room and high temperature. Besides, the fit of the fracture strength of the material to the normal, Weibull and Type I extreme value distributions is investigated.

Four-point bending

The test described here was performed to determine the tensile strength under bending. The reason, why the tensile strength was not determined by uni-axial tensile test, lies in the high expense and difficulties of performing tensile tests with ceramics. Due to the high porosity of the specimen, it may result in overloading the clamped zone of the specimen and therefore an early rupture of the material in this zone. The four-point bending test is preferred because an extended region with constant bending moment exists between the inner rollers. A Zwick/Roell Z005 testing machine was used to perform the test. Specimens were cut using a wire saw out of a plate of $120 \times 100 \times 10$ mm dimension. Thereafter, each specimen was examined optically to find any visible edge fracture due to the cutting process. Most of the specimens were in perfect or near-perfect condition. Before testing, each specimen was measured by Digital Vernier Caliper for the width and thickness. The average width and thickness of three measurements were $b = 11$ mm and $h = 10$ mm. The length between the two base supports was set with the load

fixture to 90 mm to reduce the geometrical effect on the measurement as well as the probability of local damage around the contact point with the supports. The inner rollers have a distance of $a = 35$ mm to the left and right base supports. An ambient temperature of 23 °C was recorded during the tests. A digital recorder was used to read the deflection of the specimen at the half length between the two base supports. The applied force was read by another digital recorder from the load cell in Newton. A group of 21 specimens were tested. In many cases, after a specimen failed, the crack could only be observed by a 30x optical magnification in the middle of the specimen.

The maximum tensile stress in the surface of the beam when it fails, the modulus of rupture σ_r, is calculated for an elastic material using

$$\sigma_r = \frac{3Fa}{bh^2} \tag{3.1}$$

where F is the applied force on the beam.

Compressive tests

The axial compression test was performed using a universal electromechanical spindle testing machine (Zwick 1474). For a comparative study of the compression strength at different temperatures starting from room temperature, the testing machine dictates a certain range for cylindrical specimen. The average height of the specimen (h=24.8 mm) is limited by the distance between two transmitted laser beams of the laser extensometer mounted onto the testing machine, whereas the average diameter of specimen (d=19.8 mm) is confined to the diameter of the high temperature ceramic pressure rams (25 mm). Nevertheless, the height-diameter ratio of 1.25 (L/D < 2.0) and assuming the absence of friction at the contact surfaces provide a homogenous compression and the specimen size is large enough to provide a reasonable sampling volume and quasi-uniform load transmission state. The study begins with compressive tests at room temperature. A group of 20 specimens were tested here. These twenty specimens stem from two specimen batches which were produced separately; one batch with eleven specimens (specimen number starts with CRTI) and the other one with nine

specimens (specimen number starts with CRTII). The loading surfaces were machined and checked for parallelism. Load as high as 3500 N was required for some specimen. This load complied with the capacity of the load cell that was used. All tests were stopped when the ultimate force (the force under which the specimen breaks) was reached during the test. Furthermore, the temperature influence on the compression strength was investigated using a number of 4 to 5 samples for each series of compressive tests at various temperatures.

Failure statistics

Failure strengths of ceramics are distributed over a wide range of values, even if the specimen are prepared and tested in the same way and under the same condition. Not taking special care by production and handling of the ceramics results in having strength distribution more or less symmetrical, which can be fitted by a normal or Gussian distribution. Weibull distribution is also used frequently for strength distributions of ceramics. It is related to extreme value distributions and provides some mathematical advantages. Another possible distribution for fracture strength is the Type I extreme value distribution. In this work, the fit of failure strength, determined by compressive as well as four-point-bending tests, to these distributions were studied. In the following, the three distributions are described, after which they are compared to the experimental results.

The basic relationship of the Weibull statistical theory, the Weibull two-parameter distribution, is used in the form

$$P(R) = 1 - \exp\left[-\left(\frac{R}{R_0}\right)^m\right] \tag{3.2}$$

where $P(R)$ is the probability of the fact that the limiting stresses for a ceramic body do not exceed R , m is the coefficient of homogeneity (Weibull modulus) that shows the width of the distribution, and R_0 is a coefficient having the dimension of stress and dependent upon the volume and character of load of the body. For large m, the

distribution is narrow, whereas for small m a broad distribution is indicated. A symmetrical distribution is expected at m of about 3.6 [62]. A tail of lower values of R can be observed for higher values of m, while the distribution at small m is inclined to the higher values of R. In the value range of 2 to 6 for m, the Weibull distribution is similar to the normal distribution. In this equation, all samples are assumed to have the same volume and stress distribution. The estimator used to calculate the probabilities is

$$F_i = \frac{i - 0.5}{n} \tag{3.3}$$

which has proven to be appropriate for sample sizes of 20 or greater [64]. For small sample sizes (approximately 10) it has been recommended to use

$$F_i = \frac{(i - \frac{3}{8})}{(n + \frac{1}{4})} \tag{3.4}$$

that gives the least-biased estimate [63].

The probability density function for the normal distribution is

$$P(R) = \frac{1}{\alpha\sqrt{2\pi}} exp\left[-\frac{(R_i - \bar{R})}{2\alpha^2}\right] \tag{3.5}$$

where $\bar{R}$ and α are the mean value and the standard deviation, respectively. The equations for determining $\bar{R}$ and α from a sample of N measurements R_i are

$$\bar{R} = \frac{1}{N}\sum_{i=1}^{N} R_i \tag{3.6}$$

and

$$\alpha^2 = \tfrac{1}{N}\textstyle\sum_{i=1}^{N}(R_i - \bar{R})^2. \tag{3.7}$$

Integrating the probability density function of the normal distribution gives the fraction F of samples that breaks below R_i

$$F = \frac{1}{2}\left[1 + \text{erf}\left(\frac{(R_i - \bar{R})}{\alpha\sqrt{2}}\right)\right] \text{ , erf(u)} = \frac{2}{\pi}\int_0^u e^{-\lambda^2} d\lambda \tag{3.8}$$

where erf( ) is the error function.

Apart from the conventional way of linear regression to determine the unknown parameters in a distribution function, one may obtain the best estimates of these parameters using the maximum likelihood method [144-145]. It presents the smallest coefficient of variation which is the ration of the standard deviation to the sample mean. For the two parameter Weibull distribution, the parameter m from N measured strength, R_i can be determined by

$$\frac{\sum_{i=1}^{N} R_i^m \ln R_i}{\sum_{i=1}^{N} R_i^m} = \frac{1}{m} + \frac{1}{N}\sum_{i=1}^{N} \ln R_i \qquad (3.9)$$

where the estimate of m can be acquired by an iterative procedure. Subsequently, R_0 is given by

$$R_0^m = \frac{\sum_{i=1}^{N} R_i^m}{N}. \qquad (3.10)$$

Extreme value distributions [146] are the limiting distributions for the minimum or the maximum of a large collection of random observations from the same arbitrary distribution. In the context of reliability modeling, they come up with frequent usage as distribution for the minimum. As an example, consider a system, having N identical components in series, which fails when the first of these components fails. Then system failure time is the minimum of N random component failure times. According to the extreme value theory, the system model is not dependent to the choice of component model and will approach a Weibull distribution as N becomes large. Likewise, it holds at a component level, where the component failure occurs when the first of many similar competing failure processes reaches a critical level. The distribution is marked as the Type I Extreme Value Distribution (Gumbel distribution), when it is the limiting distribution of the minimum of a number of unbounded identically distributed random variables. The probability distribution function for the Type I extreme value distribution is

$$P_I(R) = \frac{1}{\beta}\exp\left[\frac{R_i - \mu}{\beta} - \exp\left[-\left(\frac{R_i - \mu}{\beta}\right)\right]\right], \tag{3.11}$$

where μ and β are location and scale parameter, respectively. The cumulative distribution function F is given by

$$F = \exp\left[-\exp\left[-\left(\frac{R_i - \mu}{\beta}\right)\right]\right] \tag{3.12}$$

In order to describe how well these distributions fit the fracture data, some measure of the goodness of fit between the functions and data is required. The measure of goodness of fit used here is the sum of squares

$$Q = 1 - \frac{\sum_{i=1}^{N}\left(R_i - \hat{R}_i\right)^2}{\sum_{i=1}^{N}(R_i - \bar{R}_i)^2} \tag{3.13}$$

where $\hat{R}_i$ is the value of the fracture stress which is calculated for these three distributions as follows:

Normal distribution: $$\hat{R}_i = \bar{R} + \sqrt{2}\,\alpha\,\mathrm{erf}^{-1}(2F - 1) \tag{3.14}$$

Weibull distribution: $$\hat{R}_i^m = -R_0^m \ln(1 - F) \tag{3.15}$$

Type I distribution: $$\hat{R}_i = \mu - \beta \ln[-\ln F] \tag{3.16}$$

where F is the appropriate value from the ranking of failure strengths. The fit is perfect, when $Q = 1$ which means the calculated values of $\hat{R}_i$ are equal to the measured ones; $Q \gtrsim 0.95$ represents a good fit and for $Q < 0.90$ the fit is considered as poor.

Results and discussion

The load-displacement diagrams for both compressive and four-point bending tests are analyzed first, Fig. 3.4. On some diagrams small dips (Fig. 3.4b) were observed, which were caused by local fracture which does not lead to global failure.

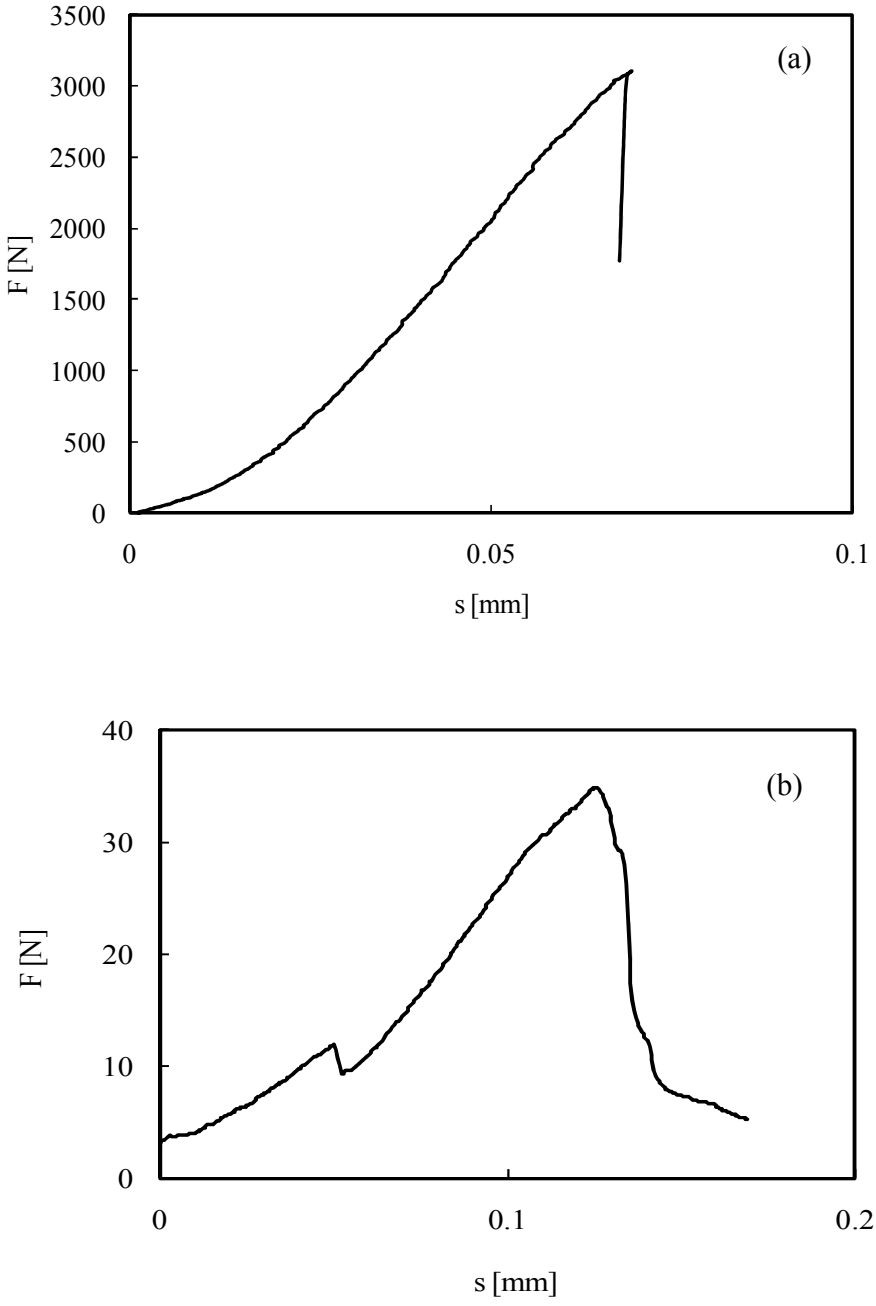

Fig. 3.4. Force-displacement curves as measured in (a) compressive test, (b) bending tests

The compression and tensile strengths for sound absorbing ceramic were determined and are listed in Table 3.2. The strengths in this table are calculated

considering the load-bearing intersection area of the specimen. Details about the sample dimensions can be found in Appendix A.1 to A.4.

Table 3.2. Test data of the compressive and four-point-bending tests

Compressive strengths [MPa]									
CRTI1	CRTI2	CRTI3	CRTI4	CRTI5	CRTI6	CRTI7	CRTI8	CRTI9	CRTI10
10.1	11.4	11.3	4.8	8.5	10.1	10.6	5.3	4.8	6.4
CRTI11	CRTII1	CRTII2	CRTII3	CRTII4	CRTII5	CRTII6	CRTII7	CRTII8	CRTII9
12	6.9	3.7	7	7.7	5.2	6.7	8.9	4.0	8.1
Modulus of rupture [MPa]									
BRT1	BRT2	BRT3	BRT4	BRT5	BRT6	BRT7	BRT8	BRT9	BRT10
5.0	2.2	5.0	2.8	3.0	2.3	2.5	2.7	3.0	3.7
BRT11	BRT12	BRT13	BRT14	BRT15	BRT16	BRT17	BRT18	BRT19	BRT20
2.7	3.6	2.5	3.3	2.4	2.7	4.0	2.5	3.7	4.3
BRT21									
2.50									

The parameters for the distributions are listed in Table 3.3. It shows a reasonable scattering of the mechanical strength caused by high porosity, material production and sample preparation. The modulus of elasticity of the porous ceramic, calculated from the compressive test data lies between 1344 - 4821 MPa.

Table 3.3. Parameters of distribution functions for test data

Distributions	**Bending strength**		**Compression strength**	
Normal	$\alpha = 0.84$ MPa	$\bar{R} = 3.16$ MPa	$\alpha = 2.55$ MPa	$\bar{R} = 7.68$ MPa
Weibull (least squares)	$m = 4.42$	$\bar{R} = 3.48$ MPa	$m = 3.35$	$R_0 = 8.6$ MPa
Weibull (ML)	$m = 3.85$	$\bar{R} = 3.49$ MPa	$m = 3.27$	$R_0 = 8.54$ MPa
Weibull (ML & biasing factor)	$m = 3.63$	$\bar{R} = 3.46$ MPa	$m = 3.08$	$R_0 = 8.84$ MPa
Type I extreme value	$\beta = 0.71$MPa	$\mu = 2.76$ MPa	$\beta = 2.18$MPa	$\mu = 6.43$ MPa

The empirical cumulative fracture distribution F over the fracture strengths, the Weibull plot (least squares) and the Type I distribution plot are shown for the compressive test in Fig 3.5. The plots of these distributions for four-point bending tests are listed in the Apendix A.5 to A.7. The fit lines in these plots are calculated from equations 3.14 to 3.16.

(a) Cumulative fraction versus fracture strength

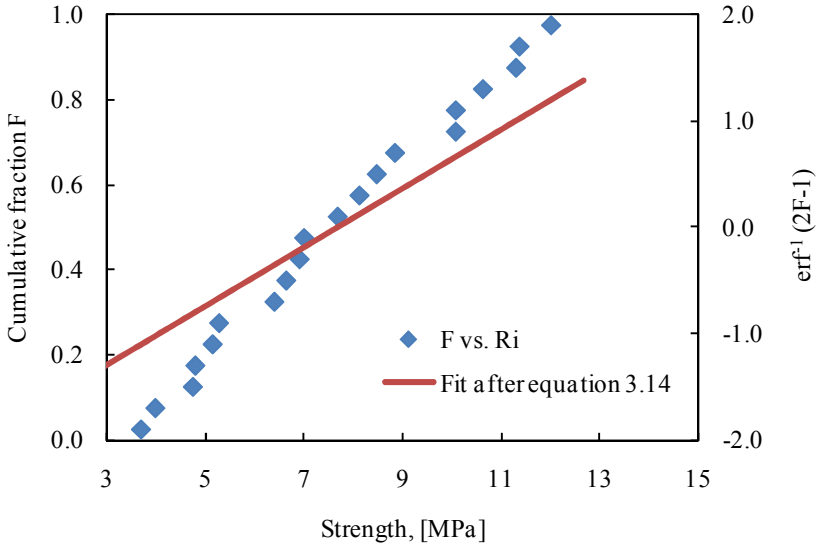

(b) Weibull plot

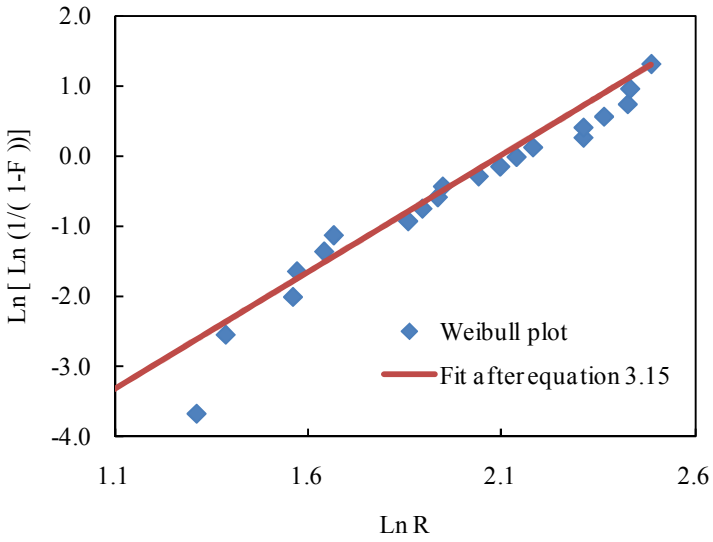

(c) Type I distribution plot

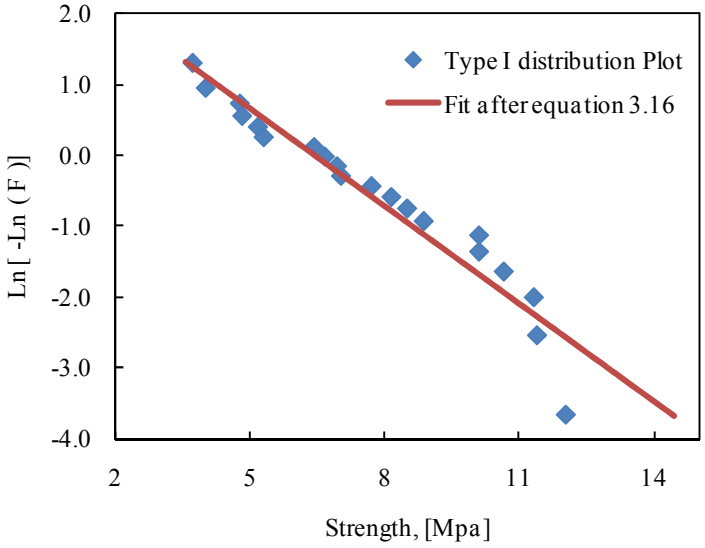

Fig. 3.5. Plots of different distributions for the compressive test results; lines are calculated from equations 3.14 to 3.16

Table 3.4 represents a comparison between the fits to these distributions by the sum of squares Q.

Table 3.4. Measures of fit to bending and compressive strengths

Distributions	**Measure of fit**	
	$Q_{Bending}$	$Q_{Compression}$
Normal	0.862	0.77
Weibull (least squares)	0.868	0.974
Weibull (ML)	0.866	0.956
Weibull (ML & biasing factor)	0.854	0.953
Type I extreme value	0.957	0.973

In the case of compression strengths, all the Weibull distributions and the Type I distribution fits the data considerably good, whereas the Normal distribution gives

here a relative poor fit. Considering the fracture strengths from the bending tests, the Type I distribution fits the data much better than the other distributions. The fits of least squares by both data series are slightly better than the results from the maximum-likelihood method, although there are statistical reasons [145] to prefer the latter. Since this comparison is based on two sets of data and relative small number of tests, this conclusion is tentative to be generalized for such porous ceramics.

The temperature influence on the material strength was also investigated. Compressive tests were performed at six constant temperatures. A number of 4 to 5 samples were used per test and the results are statistically presented on the whisker chart in Fig. 3.6. The points on this chart represent the mean values of the compression strength, whereas the whiskers show the standard deviation.

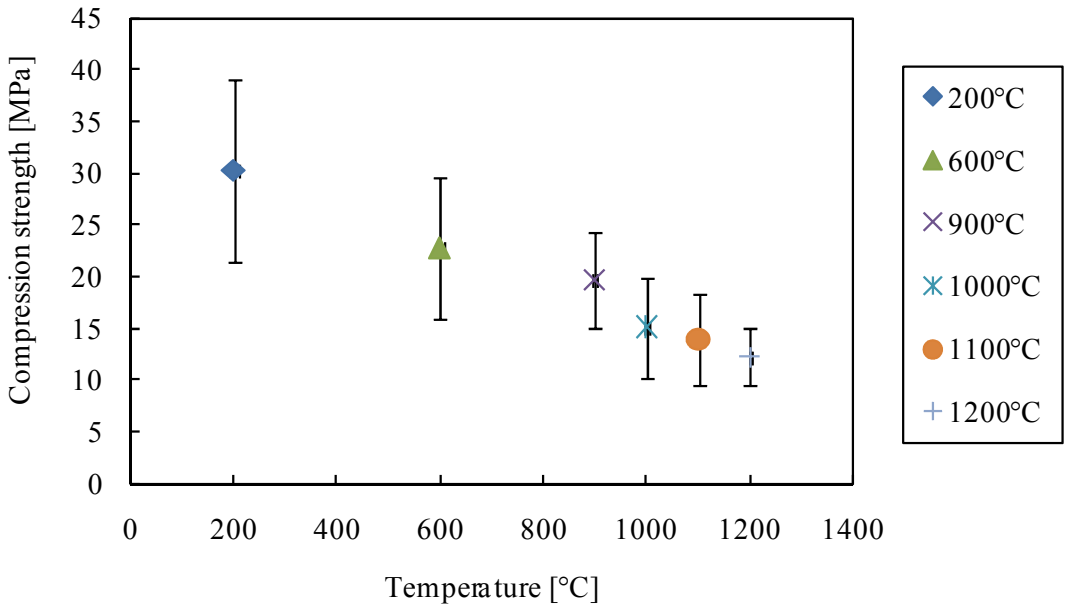

Fig. 3.6. Temperature influence on the compression strength

It shows a considerable, almost linear decrease of compression strength with increasing temperature. The reason for this is the behavior of the glass content of the material during the temperature increase. The tests in this investigation were carried out

up to 1200°C due to temperature limits of the test equipment at 1300°C. A better quantifying description of the material behavior over temperature could be achieved by larger number of samples at each temperature. The relative standard deviation of these results lies in the same range of 20% to 30%. Considering the high sound absorption of this material and the mechanical strengths determined here, a material reinforcement by use of short fibers or a structural change using graded porosity distribution can help to gain a competitive advantage for this absorber over traditional heat shields used as tiles in combustion chambers of gas turbines.

DETERMINATION OF THE THERMAL PROPERTIES

The thermal properties like thermal expansion coefficient and thermal conductivity coefficient of porous sound absorbing ceramic are determined and the measuring methods are briefly introduced in the following. Hereby, the main focus is to measure the required properties for the numerical investigations, rather than the full thermal characterization of the material, which was not applicable due to steady improvement of the material and measurement limitations at hand.

Thermal expansion coefficient

The thermal expansion coefficient of the ceramic absorber was determined by thermal mechanical analysis. The thermomechanical analyzer (TMA 801s, BÄHR-Thermoanalyse GmbH, Germany) used here acts as dilatometer for measurements under inert gas, vacuum and air within a temperature range of −160°C up to 2400°C.

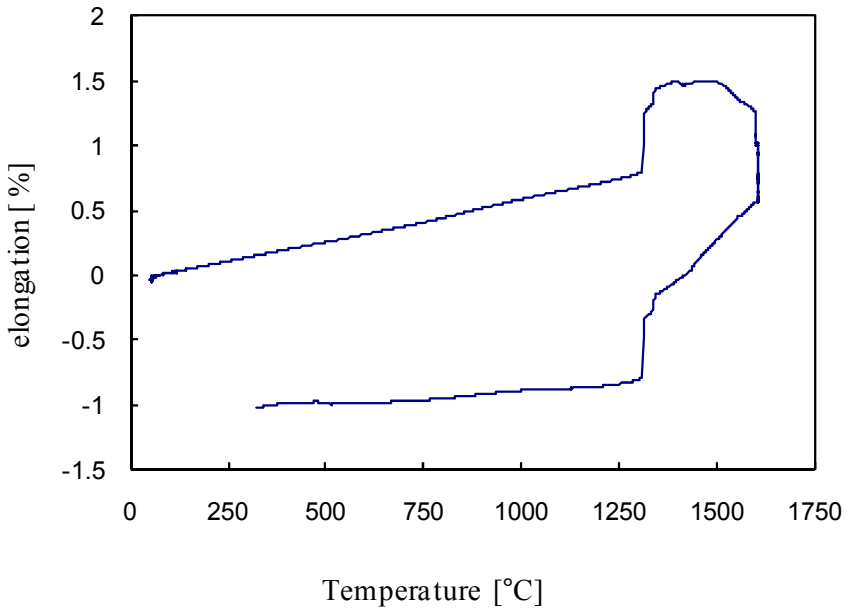

Fig. 3.7. Relative elongation of the ceramic absorber with respect to the temperature

The start of the expansion was observed at almost 70°C and obeys a linear behavior up to 1300°C. The heating curve jumps then rapidly and the behavior is not stable in the temperature range from 1300°C to 1600°C. During the cooling, the shrinkage becomes also linear and drops at 1300°C rapidly. Although this behavior should be investigated for potential changes in the material, the curve delivers the needed thermal expansion coefficient $\alpha = 5.38\ [1/10^6\,°C]$ and a remark to limit the range of mechanical tests to avoid misinterpretation of the results.

Thermal conductivity measurement

There are several methods for the experimental determination of the thermal conductivity of a bulk solid material. However, depending on the specific sample geometry, measurement equipment and the apparatus available, one has to determine the most appropriate technique. Among the conventional techniques (Steady State Method,

the Comparative Technique, the Radial Flow Method, etc.), there are two measurement technique available within the cooperation framework of the Graduate School: Laser-Flash Diffusivity [147] and Transient Hot Bridge (THB) technique. In the former one side of the sample is irradiated by use of a short laser pulse and at the opposite side of it, the temperature rise is monitored by an IR detector. The temperature rise over the time gives the basis for the calculation of the thermal diffusivity. Having the density and specific heat capacity of the sample, the thermal conductivity of the sample is calculable from the thermal diffusivity. The restriction here by the apparatus at hand is the relative small admitted sample geometry (thin disks or plates) of ca. 20 mm diameters. Due to the variety of pore size up to 4 mm it is impossible to create a representative sample for this measurement.

The THB technique gives more freedom in case of sample geometry. The technique, developed at Physikalisch-Technische Bundesanstalt, Germany, is an evolution of the Transient Hot Strip (THS) technique, i.e., Gustafsson's method [148-150] . The THS is known as a method for measuring the thermal conductivity of solids [151]. A thin metal strip, completely embedded inside the material under test simultaneously acts as a Joul heater and resistance thermometer. Its temperature dependent voltage drop in time is a measure of the transport property mentioned. It soon turned out that, due to its larger cross-section area, the strip has the drawback of a smaller electrical resistance than a wire. Thus, the temperature-dependent voltage signal is much smaller. Therefore, often nanovoltmeters are required to measure the output signal. The THB method preserves all advantages of the strip but avoids its major drawbacks. It uses multiple strips on polyimide foil sensor which confines its temperature range of application to 240°C. Eight strips are connected to a symmetrical Wheatstone Bridge to provide effective thermal and electrical self-compensations Fig. 3.8.

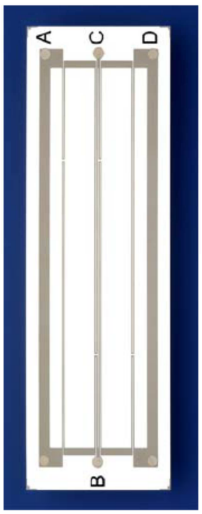

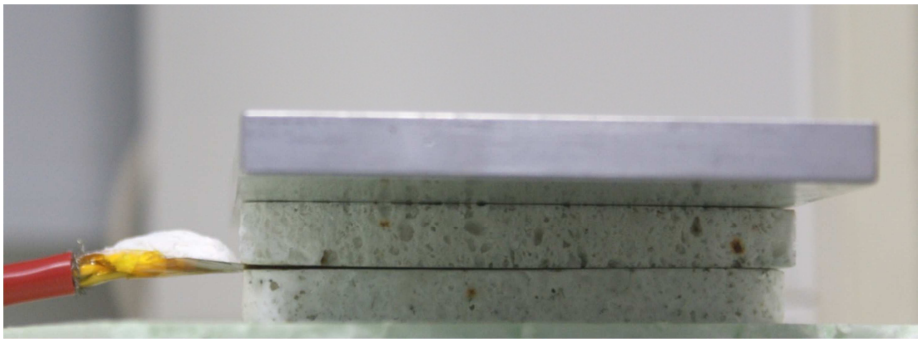

Fig 3.8. (left) Lay out of the transient hot bridge sensor. B and C are current sources, A-D are solder pads[150]; (right) measurement set-up

The layout of the sensor consists of four tandem strips in parallel. Each tandem strip comes in two individual strips, a short and a long one. Two of the tandems are located very close to each other at the center of the sensor and one additional tandem on either edge. All eight strips are symmetrically switched for an equal-resistance Wheatstone Bridge. At uniform temperature, the circuit is initially balanced. With an electric current, the pair wise unequally spaced strips establish a predefined inhomogeneous temperature profile that turns the bridge into an unbalanced condition. From now on, the sensor produces an almost offset-free output signal of high sensitivity. This voltage rise in time is a measure of the thermal conductivity, thermal diffusivity, and volumetric specific heat of the surrounding specimen. The signal is virtually free of thermal electromotive forces because no external bridge resistors are needed. Each single strip is meander-shaped to give it a higher electrical resistivity. The segmentation into tandems compensates for the so-called end effect, i.e., the temperature drop at both ends of a linear or strip-shaped heater. In contrast to those bridges having some of their resistors located remotely from the measuring area, a THB sensor is completely surrounded by the specimen. Thus, no errors are introduced by the wiring of the bridge or any (external) noise pick-up.

The sample used for this method was a plate of 100 mm length, 50 mm width and 10 mm height. The Plot of the voltage drop versus the logarithm of time is a S-shaped curve, from which the quality of the measurement is estimated and also the thermal conductivity is calculated [148], Fig. 3.9. The measurement was performed by the department of Thermodynamics at the University of Bremen.

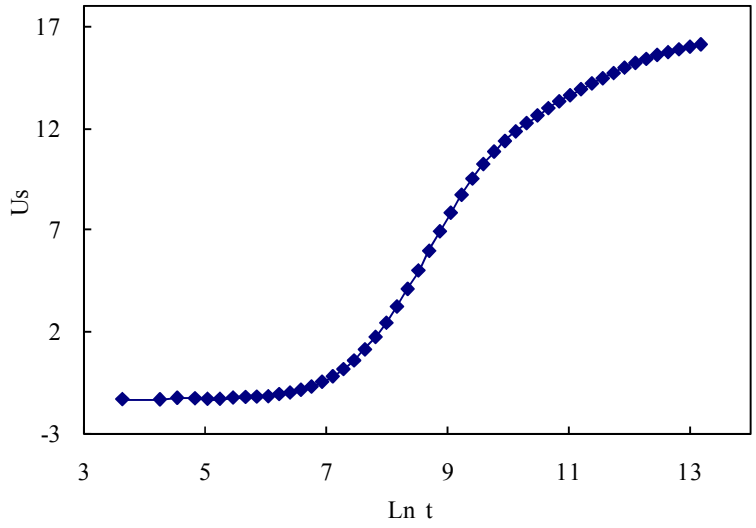

Fig. 3.9. Plot of the voltage drop versus the logarithm of time in THB method

Seven tests were carried out at room temperature, which give a mean value of 0.4323 W/m.K with a relative error of 4.9 % for the thermal conductivity. Owing to some technical problems, a measurement for higher temperature up to 225°C (temperature limit of the sensor) was not possible. Nevertheless, the technique is very promising in case of rapid estimation of the thermal conductivity of research samples. The characterization of this porous absorber respecting the thermal conductivity over a temperature range up to 1600°C by a third party out of the Graduate School was not supported. Furthermore, the porous absorber is still under continuous improvement concerning material development and acoustic behavior, so that such a characterization does not make a good financial sense.

Specific heat capacity

The specific heat capacity of the porous absorber was determined by the modulated differential scanning calorimetry (MDSC). In this method, the specimen is exposed to a cyclic heating profile, a sinusoidal oscillation overlaid on the linear ramp [152-153]. The MDSC provides several advantages including separation of the reversing and non-reversing characteristics of thermal events, increased sensitivity for subtle transitions and direct measurement of heat capacity. The latter capability is quite important (as it will be shown by the prediction of the material properties), because heat capacity and thermal conductivity are related properties.

For the measurement, a thin ceramic specimen (h<0.5 mm) was prepared by grinding a bigger specimen. As a result, the heat capacity of the ceramic matrix will be obtained. The experiment was performed by Faserinstitut e.V. in Bremen with a heating rate of 5 °C/min at 10 °C temperature intervals from 70 °C up to 220 °C, modulated by +/−0.50 °C at every 10 seconds. The mean value of the specific heat capacity for five repetitions over the measured temperature is depicted in Fig. 3.10.

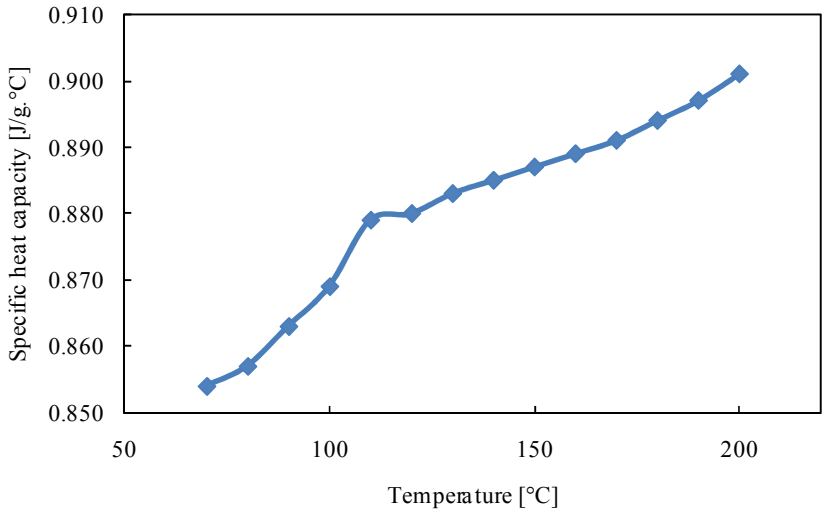

Fig. 3.10. Specific heat capacity of the matrix of the porous absorber

There is an almost linear increase of the specific heat capacity over the temperature. A qualitative prediction of this property for different volume fractions is performed in the material modeling section.

MATERIAL MODELING

Depending on the experimental procedure and limitations, either the property of the porous specimen or the properties of ceramic matrix are available. As first objective of this section, the required properties can be predicted with the use of mean-field analytical material modeling. In Table 3.5 these available properties are listed. The second objective of this study is to provide an insight into the change of the material behavior of the porous absorber with respect to the change in structural quantities. This insight is of a great importance regarding material development, material optimization, experiment cost and time reduction.

Table 3.5: Determined properties either for porous ceramic or for ceramic matrix

Measuring method / equipment	Property	Porous ceramic	Ceramic matrix
Compression test	Modulus of elasticity	X	
Bending test	Modulus of rupture	X	
THB	Thermal conductivity	X	
MDSC	Heat capacity		X
Helium pycnometry	Density		X
Dilatometer	Thermal expansion coefficient	X	

A number of 48 structure variations for the porous absorber with various volume fractions, pore form, fully aligned distribution or randomly oriented pores in 2D or 3D are studied. Fig. 3.11 shows the structure parameter varied in this study.

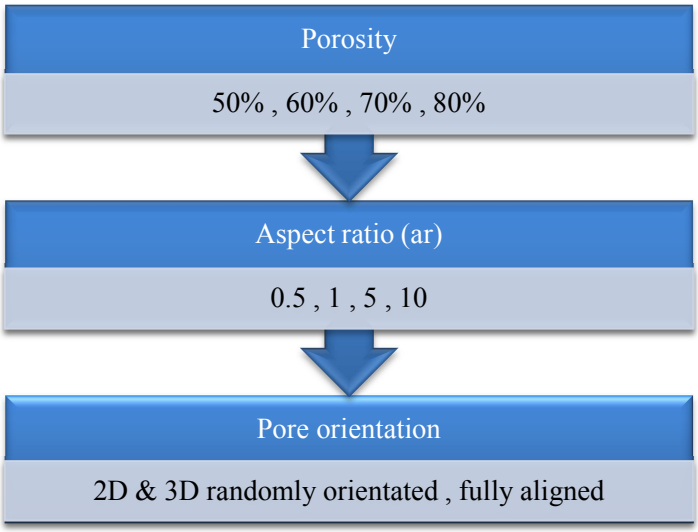

Fig. 3.11. Structure parameters for the parameter study

The porosity values were chosen according to the acoustic investigations on ceramic sound absorber [138]. Low airflow resistance is reached by a high grade of pore connectivity (open porosity), which itself is a function of the solid content in the slurry. The pore form observed by µ-CT scan and also cross-section scan of the specimen (Fig. 3.2) is a combination of ellipsoidal pores with the given aspect ratios (length along the axis of revolution over the in-plane diameter orthogonal to the axis of revolution of an ellipsoid). For each porosity value, an analysis was carried out by changing the aspect ratio and pore orientations according to the value of Table 3.5. As discussed in the specimen preparation section, the freezing of the specimen on all sides gives almost a homogeneous pore distribution over the specimen volume. Nevertheless, the study of 2D random pore or rather fully aligned (fixed) orientation, based on different cooling conditions, give a qualitative prediction of the elastic properties of the porous absorber. With the fixed orientation, the pores in the representative volume element under study are aligned in the same direction. Two spherical angles define the orientation vector **P** as is

shown in Fig. 3.12. The fixed orientation in this study is in the direction of axis 1 ($\theta = 0°, \varphi = 90°$). In 2D random orientation, the pores are oriented in the (1,2)-plane, whereas for random 3D they are oriented in all three dimensions.

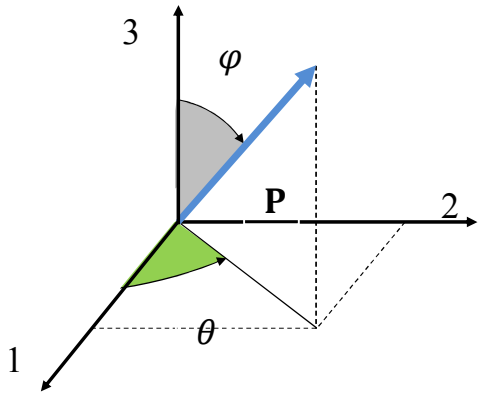

Fig. 3.12. Coordinate axis for the orientation

The macroscopic response of the porous ceramic to a loading is computed based on the homogenization of the response of each phase (here ceramic matrix and air inclusions) to the same loading. For this comparative study the Mori-Tanaka homogenization scheme is implemented. For two-phase elastic materials the Mori-Tanaka scheme delivers a good prediction in practice over a wide range of volume fractions, but in the theory, it is restricted to volume fractions less than 25%. The air inclusions in this modeling are considered as void phase, say, zero stiffness and no material assignment for the pores. The real inclusion size in these schemes is beneficial only in case of an existing coating phase around the inclusions, then, the inclusion radius is used to compute the volume fraction of the coating phase.

At first, Poisson`s ratio of the porous ceramic and the modulus of elasticity of the ceramic matrix were estimated. Due to technical limitations, theses value could not be determined experimentally. For this purpose, the modulus of elasticity calculated from the compressive test number six (4.10 GPa) is taken into account. The reason for choosing this value was because of the good match (10 % difference) between the

displacement measured by laser intensometer and the one measured by the indirect measurement system of the universal testing machine. The stress-strain curve of this test was taken as a reference for the estimation. Since both elastic properties of the matrix were unknown, Poisson`s ratio was set primarily to 0.2, a value taken from literature. Hence, there is just one unknown parameter to vary in order to match the experimental curve. A sensitivity analysis was also made to study the influence of Poisson`s ratio on the material response under compression. It is also assumed that the pore with 74% volume fraction had an aspect ratio of 1 and a 3D random orientation. The parameter study was run under a uniaxial compressive loading (quasi-static loading rate) with a peak strain of 0.002. The match is depicted in Fig. 3.13.

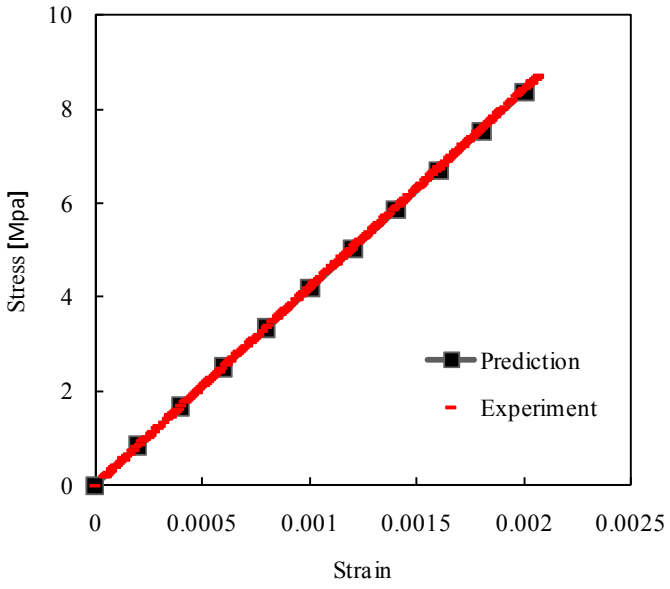

Fig. 3.13. Match of the prediction stress-strain curve on the experiment

The predicted stress-strain curve fits the experimental one and here by gives a reverse engineered value of 28 GPa for the modulus of elasticity of the ceramic matrix. Reminding the assumption of Poisson`s ratio to be 0.2, the modulus of elasticity was also calculated for typical values of Poisson`s ratio for different kinds of ceramics, Table 3.6.

Table 3.6. Calculated modulus of elasticity of porous ceramic for different Poisson`s ratios

Poisson`s ratio	0.14	0.20	0.22	0.26
Calculated modulus of elasticity [GPa]	4.21	4.10	4.18	4.17

The relative error of almost 2.6% for $\nu = 0.14$ and 1.6% for $\nu = 0.26$ is acceptable for this calculation. The dependence of Poisson`s ratio on the porosity is studied analytically and shown in Fig. 3.14. It is difficult to obtain this dependency experimentally, because it is not possible to vary Poisson`s ratio of the solid independently. Another reason is the known difficulty of accurate measurements of this property at moderate to high porosities.

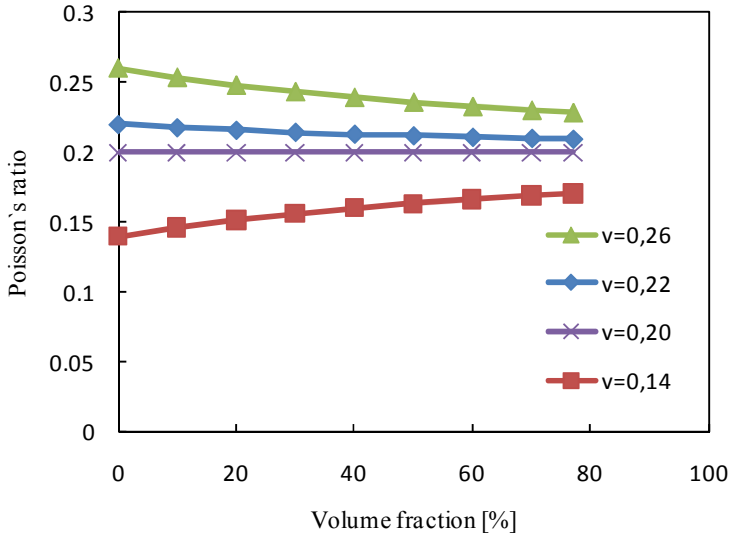

Fig. 3.14. Poisson`s ratio's change over porosity

The diagram exhibits a general trend of Poisson's ratio over porosity which converges to the value 0.2. This means that for the case, where Poisson`s ration of the nonporous material equals this convergence value, Poisson`s ratio of the porous material stays unchanged over porosity. Although, this qualitative behavior should be confirmed with

the help of experimental data, which itself is a controversial issue [67]. Large scattering by the determination of the Poisson`s ratio and small amount of experimental data at high porosity are two major difficulties for this controversy. This study just reopens another chapter in the further experimental characterization of this porous sound absorbing ceramic. Further studies in this section are based on these two calculated elastic properties of the ceramic matrix (nonporous material): $E = 28\,\mathrm{GPa}$ and $\nu = 0.2$.

Results of the material modeling show different influences of microstructure on the material stiffness. Generally, the modulus of elasticity and the shear modulus of the sound absorbing ceramic present nonlinear trends over porosity (uniaxial compression), Fig. 3.15. The pores here are considered 3D randomly oriented in the RVE.

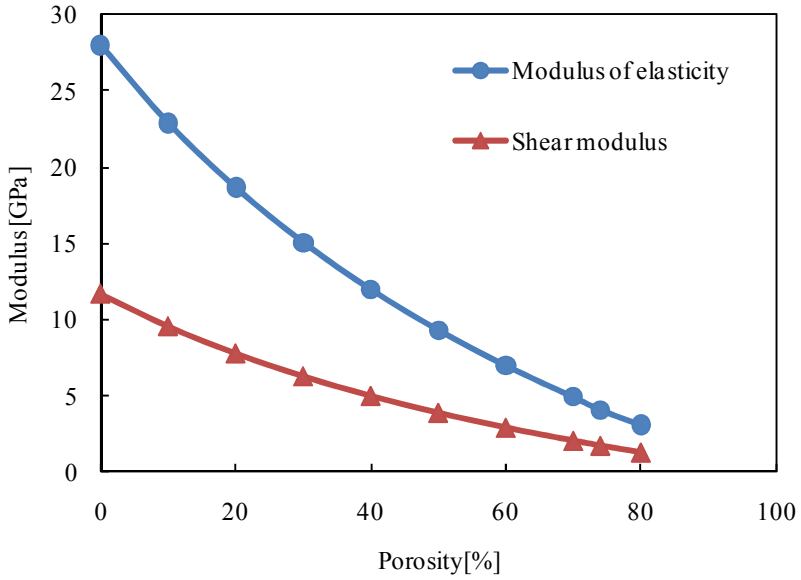

Fig. 3.15. Prediction of modulus of elasticity and shear over porosity

Different morphologies (namely 3D random, 2D in-plane random and fully aligned orientation) and different aspect ratios have also been taken into consideration. In Fig. 3.16a to 3.16c the estimates of the modulus of elasticity of the porous ceramic absorber are shown.

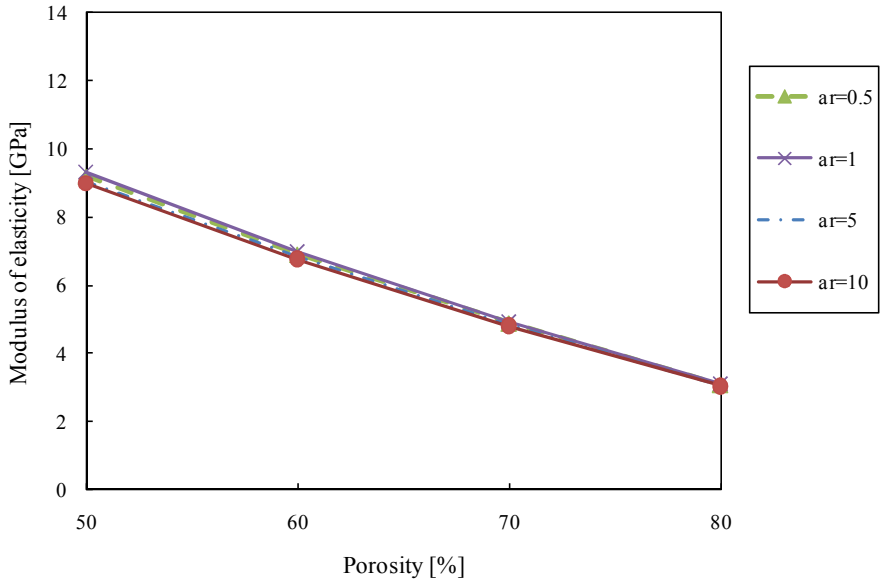

Fig. 3.16a. Modulus of elasticity vs. porosity with 3D random oriented pores and different aspect ratios

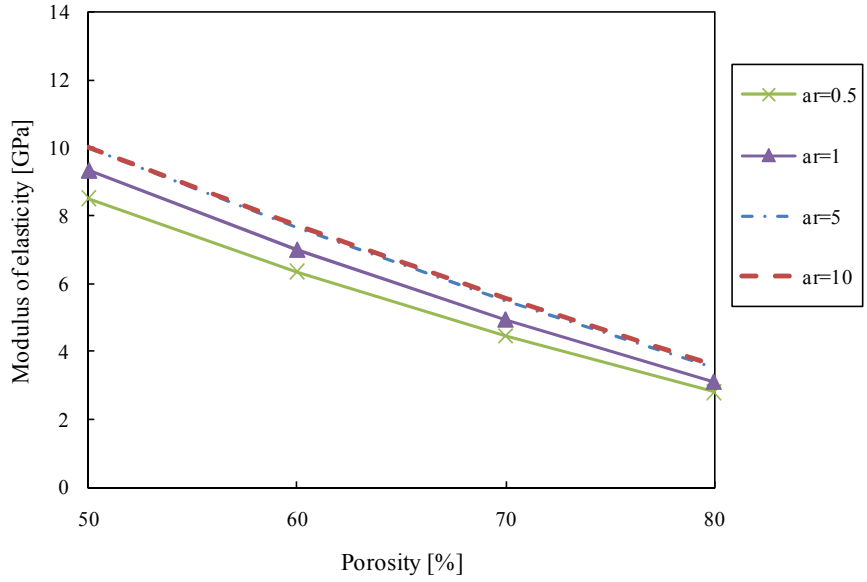

Fig. 3.16b. Modulus of elasticity vs. porosity with 2D random oriented pores and different aspect ratios

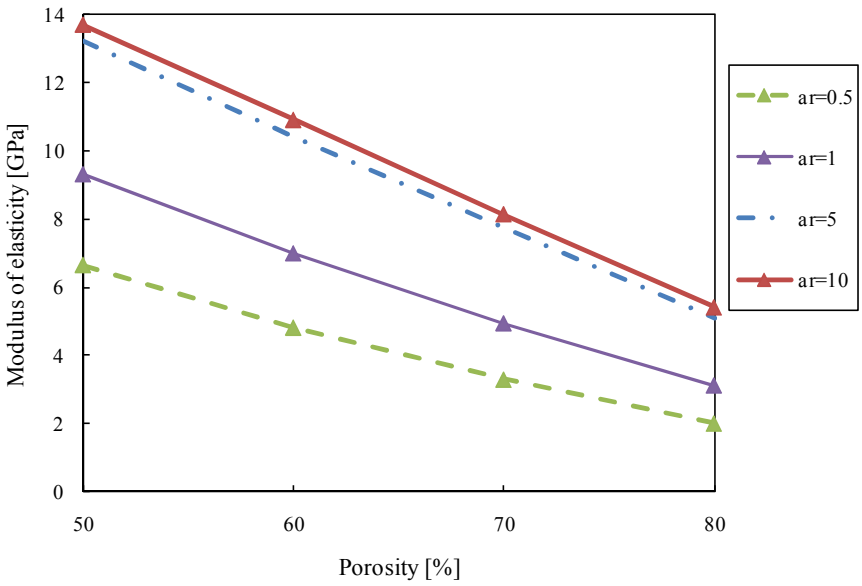

Fig. 3.16c. Modulus of elasticity vs. porosity with fully aligned pores along axis 1 and different aspect ratios

It is observed that with all three orientation types, the stiffness remains unchanged for a certain porosity range and the aspect ratio of ar=1. For other aspect ratios the estimated modulus of elasticity differs considerably with orientation. The stiffness in (1,2)-plane and along axis 1 was enhanced by increasing the aspect ratio with 2D random and fixed orientation. In case of 3D random orientation of the pores, the stiffness decreases as the aspect ratio increases. The shear modulus in 3D random orientation, in-plane and along axis 1 behaves in the same manner. Meanwhile, the shear modulus and the modulus of elasticity in the direction perpendicular to axis 1 diminish by both 2D random and fixed orientation (see Appendix A.8-A.16). Based on this study, one could state that, firstly, trying to produce a porous ceramic with nearly homogeneous pore distribution waves the further consideration of aspect ratios of the pores. Secondly, in order to enhance the stiffness of the ceramic at the high porosity values for certain kind of loadings, it may be suitable to manipulate the process to get appropriate pore orientation. The validation of these, however, is left to experiments.

The measured thermal conductivity of ceramics with 74% porosity at room temperature (T=26°C) is 0.4232 [W/m.K] which lies within a reasonable rage according to literature for thermal insulation. However, in order to find the thermal conductivity of the ceramic matrix, this material property also has to be reverse engineered from a thermal analysis. The same procedure as with the modulus of elasticity of ceramic matrices was carried out here. By adjusting different values for the thermal conductivity of ceramic matrices and running the thermal analysis with a thermal load in form of a temperature gradient of 1°C, the calculated thermal conductivity of the porous ceramic is matched to the experimental values. This gives a thermal conductivity of 2.28 [W/m.K] for the ceramic matrix. The thermal analysis used here is based on Fourier`s constitutive law. The first law of thermodynamics in equation format is as follows:

$$\rho c \frac{dT}{dt} = -\text{div}\,\mathbf{q} + r \tag{3.17}$$

where ρ, c, T, t, $\mathbf{q}$ and r are the density, the specific heat capacity, the temperature, the time, the heat flux and the volumetric heat supply, respectively. According to Fourier`s law, in case of sole thermal conductivity, the heat flux can be expressed as:

$$\mathbf{q} = -k^{th}\nabla T \tag{3.18}$$

where k^{th} is the thermal conductivity coefficient. Considering anisotropic composite materials, a thermal-conductivity tensor is used to characterize the material conductivity. The thermal conductivity of the composite varies with microstructure of the composite, the inclusion orientation distribution and the thermal conductivity are different between each phase.

In order to characterize the thermal behavior of the porous absorber in a qualitative manner, the structural parameters in Table 3.5 are used for a series of analysis. Fig. 3.17a to Fig.3.17c depicts an almost linear behavior of thermal conductivity over porosity for different pore orientations and aspect ratios.

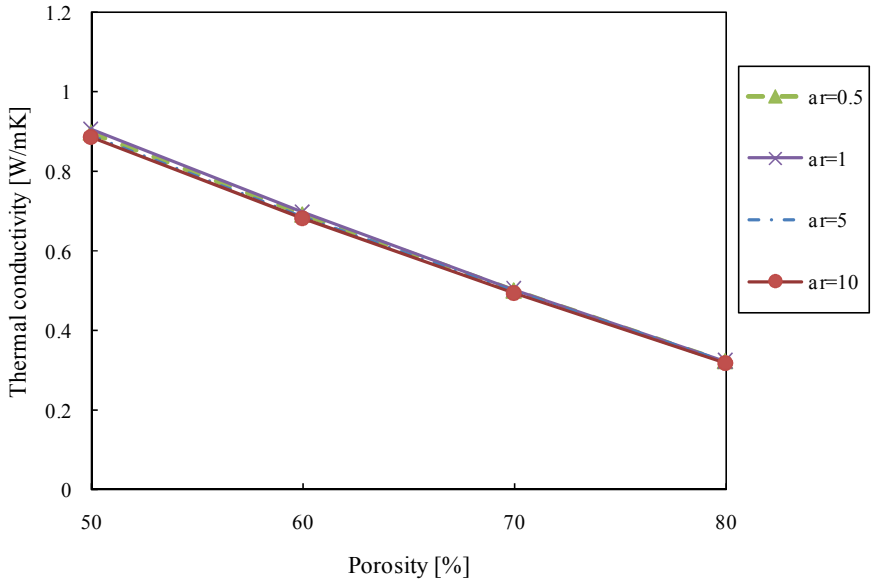

Fig. 3.17a. Thermal conductivity vs. porosity with 3D random pore orientation and different aspect ratios

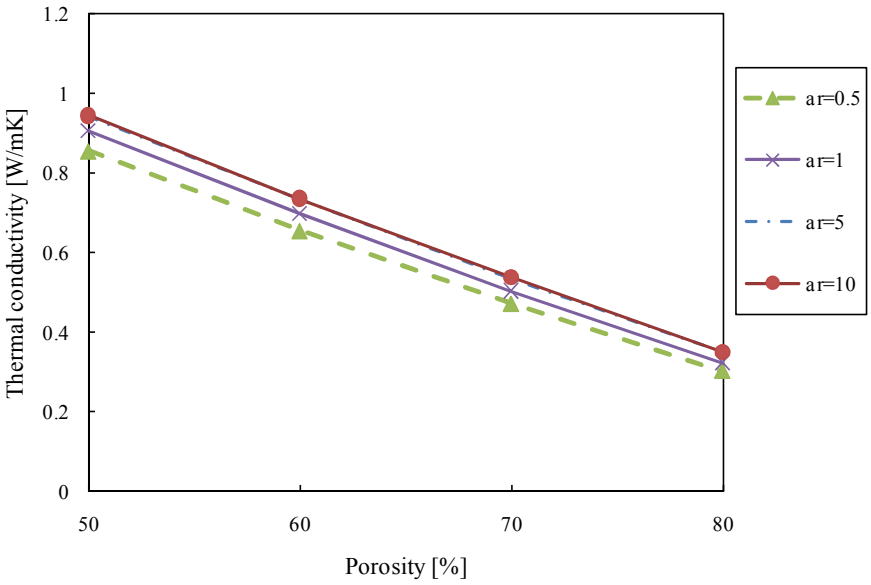

Fig. 3.17b. Thermal conductivity vs. porosity with 2D random pore orientation of pores and different aspect ratios

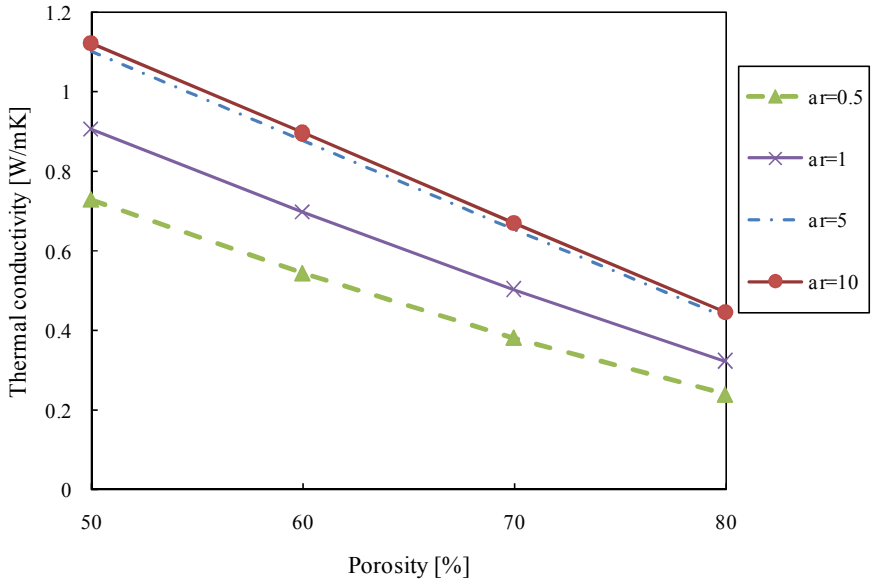

Fig. 3.17c. Thermal conductivity vs. porosity with fixed pore orientation along axis 1 and different aspect ratios

Depending on the pore orientations, the thermal conductivity changes considerably with the aspect ratios. In the case of 3D random pore orientation, the influence of the aspect ratio is in general insignificant, but a slight decrease in the thermal conductivity has been observed. In the (1,2)-plane, along the temperature gradient, a much more pronounced increase in thermal conductivity is reachable by moving toward higher aspect ratios. Further, the analysis shows a decrease in the thermal conductivity in the perpendicular direction to the direction of the temperature gradient.

The material modeling in this section was used primarily to show the qualitative behavior of the porous sound absorbing under study. Losing the technical limitations by the experimental characterization would open a door to implementation of the material modeling not only as a tool for qualitative investigation, but also as a tool for quantitative prediction of the mechanical and thermal behavior of this ceramic. This also would make the experiments more straightforward and decrease the costs and effort for the design and material investigation to be carried out.

4 Numerical Investigation

This chapter deals with simulation and damage analyses of porous ceramic sound absorbers. Investigations are performed firstly at micro scale with direct finite-element simulation of representative volume elements (RVE) and then, at macro scale, with the simulation of the real size ceramic tile, both with the help of finite-element package ABAQUS version 6.10-2. For the damage analysis a degradation model is implemented in a predefined user-subroutine of ABAQUS. It is based on the three dimensional rupture criterion (see chapter 2) and describes pure brittle damage under mechanical, static and quasi-static loadings.

Profound analyses of the damage behavior with respect to some microstructure parameters like porosity prerequisites the knowledge of compressive and tensile strengths of the ceramic matrix, which is still not easily available. These can be reverse engineered from the determined porous ceramic compressive and tensile strengths based on an analytical approach. Once these strengths are obtained, one is able to compute the critical loading of a RVE with arbitrary combination of porosity, pore shape and pore orientation using direct finite-element simulations with the implemented subroutine. The computed critical loading serves subsequently as ultimate stress for the real size ceramic tile.

MODELING OF DAMAGE

Recalling the instability criterion from equation (2.21) of chapter 2 as

$$Y \leq Y_c \,,$$

the criterion physically states that instability is imminent when the released energy due to the stiffness loss becomes equal or greater than the required energy for creation of new damage surfaces. Moreover, pure brittle damage refers either to the absence of plastic strains or to neglecting the permanent micro strains. The general law of kinetic damage considers the damage in both cases as zero and therefore the stability criterion becomes simultaneously the rupture criterion as equation (2.25) shows

$$Y = \frac{\sigma^{*2}}{2E} = \frac{\sigma_u^2}{2E}.$$

The user-subroutine UMAT has been used for implementation of this damage model. The stiffness degradation regime is further applied for pure brittle damage due to its numerical benefits. Once the rupture occurs, the ceramic material in a damaged area is not able to bear any further loading. In order to reproduce it in the model, the element associated with the damaged integration point should be eliminated. Since the element elimination is not allowed by ABAQUS implicit and the abrupt reduction of material stiffness to a certain low level (e.g. 10% stiffness), which declares the element uncapable of load bearing, a linear stiffness degradation with a constant degradation rate of 5% is implemented in the damage model. The degradation rate of 5% is adopted based on the parameter study carried out on RVEs with different porosity (ranges from 30% to 80%) considering element types (linear (C3D4) and quadratic (C3D10) tetrahedral), number of elements and the computation time. For a mesh with quadratic elements, large degradation rates (10% - 20%) impede the computation convergence which lies firstly in generation of high stiffness gradient between the damaged and undamaged integration points of an element or between neighboring elements. Secondly, the imposed instability due to the stiffness degradation should reach the equilibrium state which needs accurate incrementation and long computation time. Increasing the number of quadratic elements to the level of 200.000 (or above), the degradation rate should be decreased accordingly and one may expect long computation times. Likewise, large degradation rates cause high stiffness gradients between neighboring linear elements and disturb the equilibrium state. For a number of linear elements above 500.000, again low degradation rates should be adopted and long computation times should be expected for each RVE.

The ceramic matrix shows isotropy. Therefore, the stiffness matrix components read

$$C_{11} = C_{22} = C_{33} = \frac{(1-\nu)E}{(1+\nu)(1-2\nu)} \; ;$$

$$C_{12} = C_{13} = C_{21} = C_{23} = C_{31} = C_{32} = \frac{\nu\, E}{(1+\nu)(1-2\nu)};$$

$$C_{44} = C_{55} = C_{66} = \frac{E}{(1+\nu)}.$$

A damage indicator is introduced as

$$DI = 1 - (0.05 * SDV3) \tag{4.1}$$

where $SDV3$ refers to a state variable in UMAT which counts the number of stiffness degradation at each integration point. It takes the values from 0 for undamaged condition to 18 for the case of 5% degradation rate and means stiffness reduction to a final level of 10% stiffness. This is how the limitations by element elimination in ABAQUS implicit as well as abrupt stiffness reduction to 10% are circumvented. The stiffness matrix of the ceramic matrix is will be reduced to

$$C = \begin{bmatrix} DI\ C_{11} & DI\ C_{12} & DI\ C_{13} & 0 & 0 & 0 \\ DI\ C_{21} & DI\ C_{22} & DI\ C_{23} & 0 & 0 & 0 \\ DI\ C_{31} & DI\ C_{32} & DI\ C_{33} & 0 & 0 & 0 \\ 0 & 0 & 0 & DIC_{44} & 0 & 0 \\ 0 & 0 & 0 & 0 & DI\ C_{55} & 0 \\ 0 & 0 & 0 & 0 & 0 & DI\ C_{66} \end{bmatrix}.$$

Fig. 4.1 illustrates one increment in the UMAT calculation for one integration point. From an equilibrium at time t_n, ABAQUS performs an incremental loading with the time increment Δt as well as an initial guess $\Delta\varepsilon^{n}$ for the strain increment. The user-subroutine UMAT updates the stress state according to the constitutive law and supplies ABAQUS with a new stress tensor as well as with the derivative of stress with respect to the strain increment. Having this information, a new guess for the strain increment is calculated and the whole procedure is iterated until convergence is reached. ABAQUS supplies UMAT at an equilibrium time t_n with time increment, total strain increment, total strain for the strain increment, calculated stress by the previous increment. After building the isotropic stiffness matrix and calculating the critical strain-energy-density-release rate Y_c it will be checked by calling the "Check Failure" subroutine, if there is prior damage for this integration point($SDV \neq 0$). If no prior damage is detected ($SDV = 0$), the stress will be updated and the strain-energy-release rate for the integration point will be calculated. Subsequently a check of the instability condition will be performed. Does the integration

point fulfill this condition, it will be labeled as damaged and the degradation counter becomes 1.

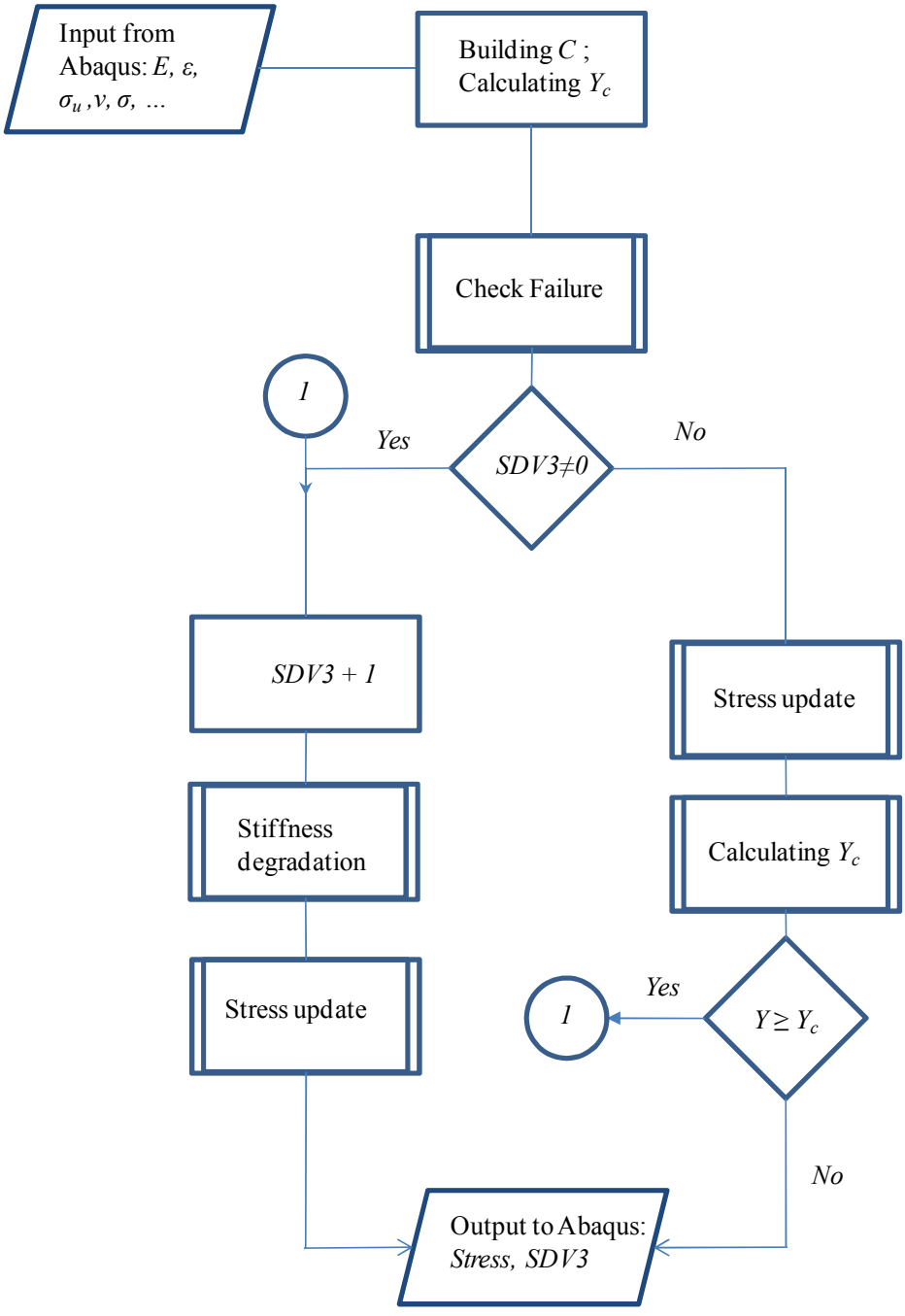

Fig. 4.1. UMAT calculation for a integration point within a time increment

Otherwise the degradation counter which remains zero and the stress will be passed to ABAQUS for this integration point and the check pursue for the next integration point. After labeling the damaged integration point, stiffness reduction takes place in the "Stiffness degradation" subroutine as introduced above. Further, the stresses will be updated and passed with new degradation counters to ABAQUS. It should be mentioned here that once an integration point fulfills the instability condition, it will remain damaged and by each time incremet its stiffness will be reduced by 5% until it reaches 10% of the stiffness of the sound matrix. The user-subroutine can be found in Appendix A.18.

DIRECT FINITE-ELEMENT SIMULATION OF RVES

In this section, direct finite-element simulations at micro scale are performed for different RVE's in order to study the micro fields in a detailed general manner. The introduced sound absorbing ceramic, however, represents a complex microstructure due to a large pore size range (0.2 to 4 mm), pore interpenetration and different pore shapes. In order to reach a good mesh and realistic user's time, some geometrical simplifications are made to the RVE's microstructures. The effect of microstructure parameters is therefore studied separately. The four porosity values (50% - 60% -70% -74%) are chosen according to the acoustic investigations on sound absorbing ceramic [138]. By each RVE just one microstructure parameter is taken into account. Bazant [154] defines the RVE as the smallest material element whose failure causes failure of the whole structure. For the RVE size, he proposes, based on the microstructural simulation and testing, a rough estimate of triple of maximum inhomogenity size (almost 4 mm pore size for the porous ceramic sound absorber). According to Lemaitre [127] the physical size of a RVE for monolithic alumina is at least 0.07 mm. Therefore a RVE size of 10 mm × 10 mm × 10 mm has been chosen. This edge length of 10 mm with pore size less than 2 mm in the RVE also allows a correlation with the ratio of cylindrical sample size of 20 mm to the largest pore diameter, which lies between 5 and 6. The RVEs in this contribution are

generated by the Digimat-FE module of the DIGIMAT software suite version 4.0 [135]. The workflow of pure brittle damage analysis of a RVE is shown in Fig. 4.2.

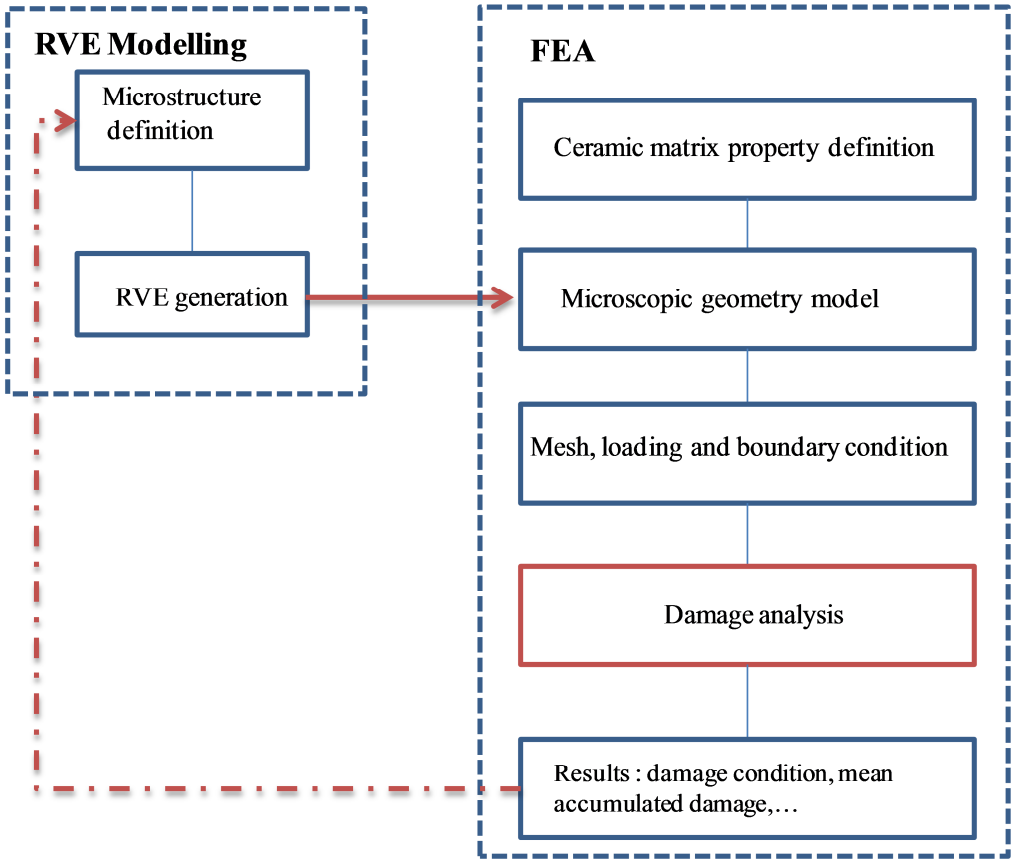

Fig. 4.2. Workflow of pure brittle damage analysis of RVE

Firstly the microstructure specifications, namely phase, porosity, coating, pore size, pore shape, pore orientation, clustering and pore interpenetration are set for a RVE. In a further step the RVE is generated and the geometry is exported to ABAQUS. In ABAQUS, after defining the modulus of elasticity, Poisson's ratio and the failure strength (ultimate stress) of the ceramic matrix, the material parameters are then assigned to the imported RVE. Followed by tetrahedral meshing, compression (or tension) and specific boundary condition are defined and the damage analysis will be started by coupling the described UMAT-Subroutine for the solution. Finally, according to the

analysis results, the microstructure parameters are varied to reinforce the RVE and avoid instability condition.

Element type selection

The choice of the element type due to the complex geometry of RVEs is tetrahedral elements. Quadratic (C3D10) tetrahedral elements give reasonable results for small-displacement problems without contacts, whereas linear (C3D4) tetrahedral elements under the condition of extremely large number provide accurate results [155]. This is examined on a RVE (70% porosity, average spherical pore size of 1.7 and 3D randomly pore orientation) which is subjected to a uniform pressure of 30 MPa and clamped from the bottom side as shown in Fig. 4.3.

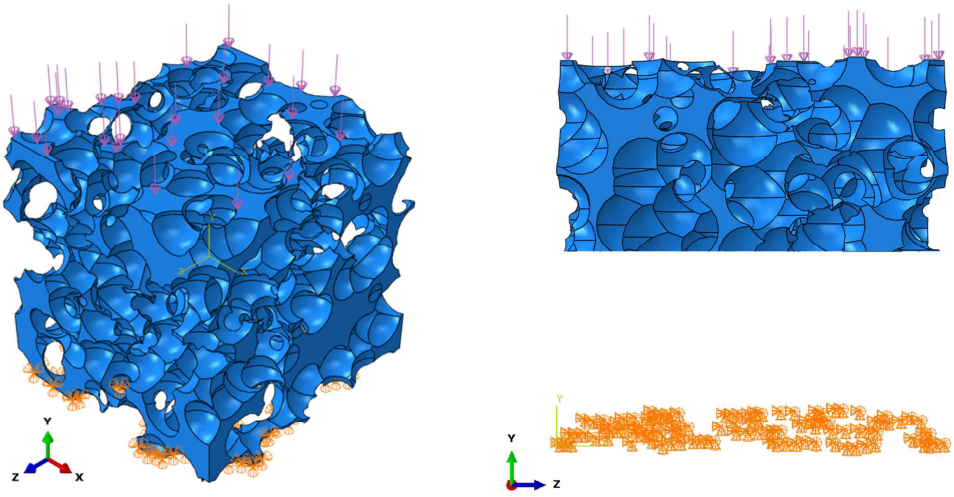

Fig. 4.3. A RVE model of 70% porosity under compression (left); A section view of the clamped restraint and the loading

Four cases are considered here: equal element number and equal degrees of freedom (DOF). For the former case, a mesh of 256924 tetrahedral elements is constructed, which gives a total number of 187140 degrees of freedom for linear and 1,259,973 degrees of freedom for quadratic elements. For a problem with a size of 358600-358800 degrees of freedom, both linear and quadratic tetrahedral meshes provide 516319 and 65383

elements respectively. All three mentioned meshes as well as results of the damage analysis for each case are shown in Fig. 4.4.

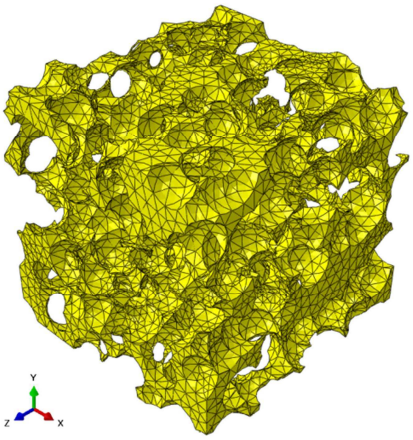

(a) Quadratic mesh with 65383 elements

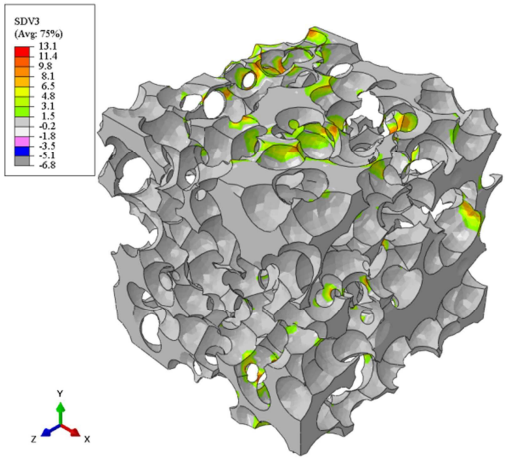

(b) Pure brittle damage condition with 65383 quadratic elements

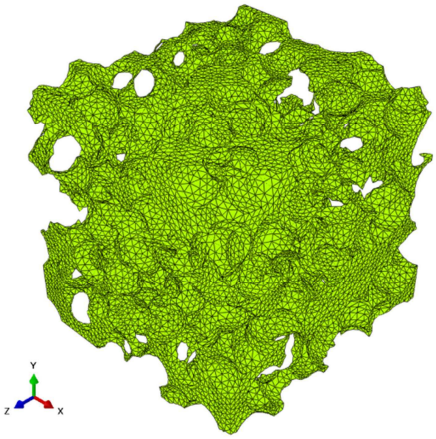

(c) Mesh with 256924 linear & quadratic elements

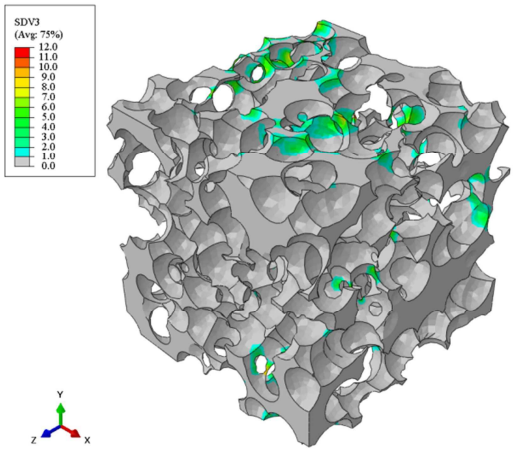

(d) Pure brittle damage condition with 256924 linear elements

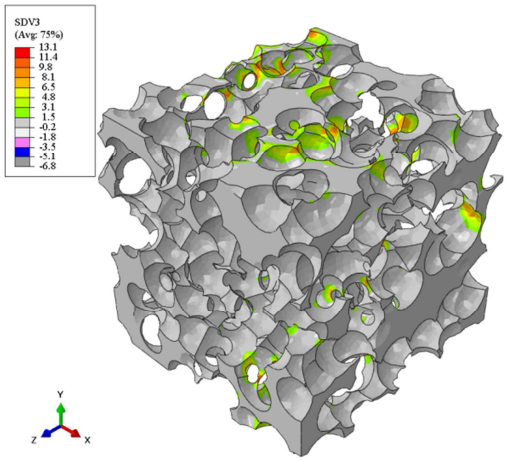

(e) Pure brittle damage condition with 256924 quadratic elements

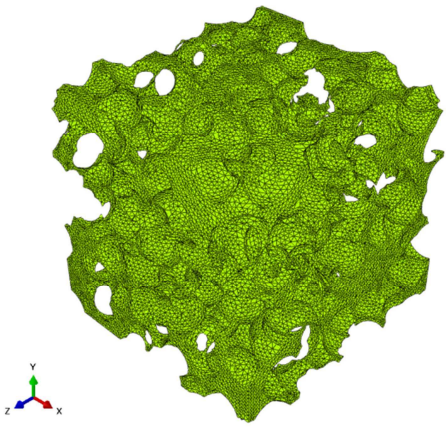

(f) Mesh with 516319 linear elements

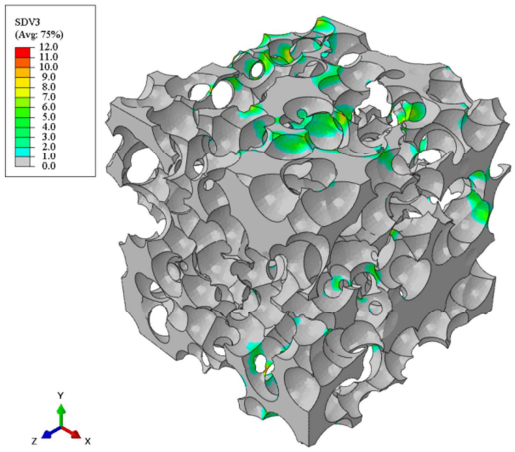

(e) Pure brittle damage condition with 516319 linear elements

Fig. 4.4. Influence of using linear and quadratic tetrahedral elements and element number on the corresponding analysis results

Qualitatively, in all mesh variations, the same damaged areas can be detected. Going further into detail, no qualitative and quantitative difference was observed in the results with 516319 and 256924 linear elements. In case of quadratic elements, an increase in the number of elements on the one hand reduces the element distortion due to bad tetrahedral quality and improves the damage tracking in the graphical presentation. On the other

hand, it increases the problem size and the associated CPU time. Nevertheless, in both meshes with quadratic tetrahedral elements, it is not convenient to track the rupture graphically. Delving into a damaged element, it will be clear that the instability has not occurred at all four integration points of the quadratic element. Large stiffness gradients have been observed between the respective integration points, too. As it can be seen later in this chapter, this effect will appear further in the diagram of the mean accumulated damage over the total solution time. It is calculated as the sum of multiplication of $SDV3$ at each integration point with the element volume over the sum of volume of all elements. Therefore the calculated mean accumulated damage by quadratic tetrahedral element is less than the one by linear element due to larger element volume with four integration points. Table 4.1 provides an overview on the four studied cases with the needed CPU time.

Table 4.1. An overview of different element type, element number and associated calculation time

	Number of elements	**Degrees of freedom**	**CPU time (sec)**	**Number of distorted elements**
Quadratic tetrahedral	256924	1259973	21579	1022
Linear tetrahedral	256924	187140	1597.8	1022
Quadratic tetrahedral	65383	358,617	1779.8	1293
Linear tetrahedral	516319	358,776	3829.7	860

The computation times are measured on a computer with Intel Core (TM) 2 Quad CPU Q9400 @ 2.66 GHz and 8 GB of memory. For the following simulations on the RVEs the use of linear tetrahedral element with very fine mesh is preferred to quadratic

tetrahedral element because of a better graphical damage traction and more accurate mean accumulated damage calculation.

SIMULATION OF THE COMPRESSIVE TEST AND VALIDATION OF THE ANALYSIS

In this section, the compressive test is simulated on the RVE with 74% porosity. As a validation of the method, an analogy will be drawn between the compression strength and the computed critical pressure for the RVE. For this, an RVE of 74% porosity is generated which contains spherical pores with 1.7 mm in diameter with 3D random orientation. Pore interpenetration is also allowed. The measured compressive load at the time of failure lies between 1146 N and 3698 N (see Appendix A.2). Assuming a homogeneous pore distribution on the nominal load bearing area of 307.7 mm^2, the actual load bearing area is about 80 mm^2 ((1-0.74) × 307.7 mm^2). Average of the compression bounds divided by the actual load bearing area gives a pressure of 31 MPa. The RVE is then subjected to a uniform pressure of magnitude 30 MPa and is clamped from the bottom side as shown in Fig. 4.5.

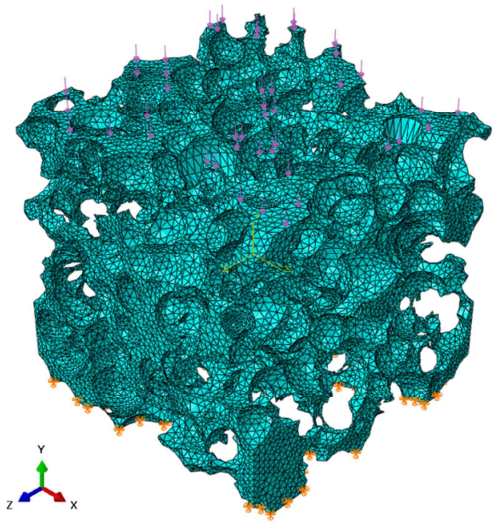

Fig. 4.5. The RVE model of sound absorbing ceramic under compression

At this point it should be reminded that the ultimate stress of a ceramic matrix is still unknown. Without this material parameter, one cannot predict the damage condition at micro scale for the RVE. The question at the micro scale is: How can we determine within reasonable accuracy the ultimate stress (strength) of the matrix with the knowledge of porosity, pore shape, pore size and the compressive strength of porous ceramic? An answer to this question is made by adopting the Generalized Mixture Rule (GMR) proposed by Ji et. al. [66] for the study of mechanical properties of porous materials in terms of the constituent's properties, porosity and microstructure. He has expressed the effects of microstructure by scaling fractal parameter J, which indeed represents size distribution, shape, continuity and connectivity of the constituting phases. The formula reads as:

$$\frac{M_C}{M_S} = (1-\varphi)^{\frac{1}{J}} = V_S^{\frac{1}{J}} = \left(\frac{\rho_C}{\rho_S}\right)^{\frac{1}{J}} \tag{4.2}$$

where M_C , M_S and φ are specific property of the composite, specific property of solid (here ceramic matrix) and the porosity. Further, ρ_C and ρ_S are the densities of the porous and nonporous materials, whereas V_S is the volume fraction of the matrix. The parameter J takes a value between 0 and 1, where $J = 0$ represents the case where the specific property of the porous material vanishes regardless of the porosity, and $J = 1$ is for the porous material with long cylindrical or hexagonal pores aligned in the stress direction. For long cylindrical pores which are perpendicular to the stress direction, the recommended value for J is 1/3 and for porous material for isolate perfectly spherical pores, Ji et. al. suggests a value of 0.5. Existence of intergranular, continuous, channel pores or cavities in comparison to the intragranular, isolated and rounded pores decreases the value of J [66]. Considering porous solids, some mechanical properties - porosity correlation equations like the one of Gibson-Ashby [72] and Phani expression [73] - can be derived from this generalized formula [66]. This approach, however, still needs some physical validity and a profound analysis in terms of analytical mechanics due to its unclear physical meaning [66].

Before adopting this generalized formula, its applicability is examined with the material property set at hand. Recalling reverse engineering of the modulus of elasticity of ceramic matrix and, on its basis, the forward computation of the modulus of elasticity for different porosity values, the diagram of modulus of elasticity ratio $\frac{E_C}{E_S}$ over the porosity can be plotted as shown in Fig. 4.6

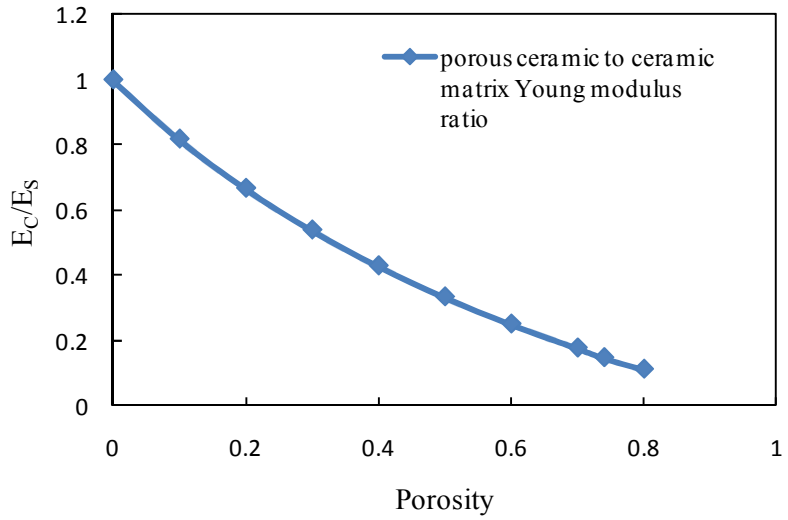

Fig. 4.6. Porous ceramic to ceramic matrix Young modulus ratio over porosity

Substitution of $\frac{E_C}{E_S}$ and φ in the equation (4.2) and solving it for J ($J_{cal.1}$) as well as solving the equation (4.2) for unknown φ and J delivers the following two sets of values, listed in Table 4.2. The latter was calculated with the mathematical package Mathematica. From the available real responses, the very set of $\varphi_{cal.}$ and $J_{cal.2}$ has been chosen, in which the value of $\varphi_{cal.}$ is near to the real porosity.

Table 4.2. Values of φ and J for different porosity based on different calculation

Porosity (φ)	$\frac{E_C}{E_S}$	$J_{cal.1}$	Relative error $(1-\frac{\varphi_{cal.}}{\varphi})$	$\varphi_{cal.}$	$J_{cal.2}$	Relative error $(1-\frac{\varphi_{cal.}}{\varphi})$
0.5	0.333	0.62	4 %	0.42	0.5	16 %
0.6	0.250	0.66	1 %	0.50	0.5	16.6 %
0.7	0.176	0.69	0.4 %	0.58	0.5	17.1 %
0.74	0.146	0.7	1 %	0.61	0.5	17.5 %
0.8	0.111	0.73	3 %	0.66	0.5	17.5 %

The right hand side of the table shows a constant value for J and different porosity with relative error of 16 % to 17.5 % to the actual porosities, where as in the left hand side of the table, different values for J with a relative error of 0.4% to 4% for certain properties are calculated. The different values of J have a mean of 0.68 and standard deviation of 0.074. For both cases, at this point, there is no comparative value of J for such microstructure with pore interpenetration and high porosity. Further, there is also no physical reason behind the fact that the calculated values of J scatter around 0.68. That is also what Ji et. al has stated, too, and will be left in this contribution to a profound experimental study. Nevertheless, the value of 0.68 could be assigned to J in the case of study of the modulus of elasticity over the whole porosity range. Equation (4.2) with the mean value 0.68 for $J_{cal.1}$ is plotted against the diagram of Fig. 4.6 in Fig. 4.7. It represents a reasonable fit to the relative Young's modulus curve over porosity.

Ji et. al. states further that the values of the scaling fractal parameter J for properties like shear, Young's and bulk moduli as well as Poisson's ratio could be different for a porous solid with a constant microstructure. As an example, for a titanium aluminide (Ti-24Al-11Nb) with porosity under 40%, he observed and reported different values of J (ranging from $J = 0.134$ to $J = 0.550$) for relative elastic properties such as the modulus of elasticity, Poisson's ratio, bulk modulus and shear modulus.

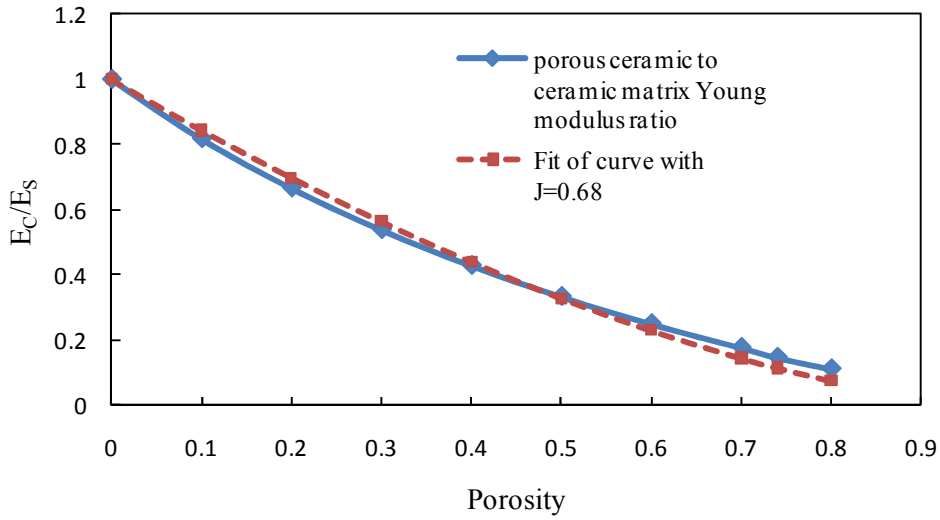

Fig. 4.6. Relative Young's modulus over porosity and its fit curve

With the knowledge of this discrepancy in the GMR, for the property strength a value for J should be determined. The only experimental value for strength is the one of 74% porous ceramic, and thus it is not possible to fit a curve in order to obtain a value for J. Moreover, from reverse engineering in chapter 3, one cannot predict the strength of a porous compound with a different porosity. Therefore an assumption should be made here for the value of J for relative strength $\frac{\sigma_C}{\sigma_{SU}}$ (σ_{SU} is the ultimate strength of the ceramic matrix). In a couple of results presented by Ji. et. al. the value of J for relative strength over porosity was lower than the one for relative modulus of elasticity over porosity. On this basis, the calculated value of $J_{cal.2}$ is taken as scaling fractal parameter for study of material strength. Substitution of φ=0.74, $J = 0.5$ and $\sigma_C = 8.6$ MPa (Table 3.3) in the equation (4.2) delivers a (at this stage) fictive value of 118 MPa for the compressive ultimate strength of ceramic matrix. In analogy to this, the ultimate tensile strength of ceramic matrix is calculated, knowing φ=0.74, $J = 0.5$ and $\sigma_C = 2.7$ MPa (Table 3.3), and amounts to 40 MPa. Based on these qualitative determined material parameters, we are now able to run the damage analysis on the RVE. For the analysis, the compression load (30 MPa) is subjected in a linear manner during the first solution step ($t = 1$ s). In

the second step, the pressure is held constant over 5 seconds during the solution. The aim is to study the behavior of mean accumulated damage. Fig. 4.7 shows the damage condition at various times.

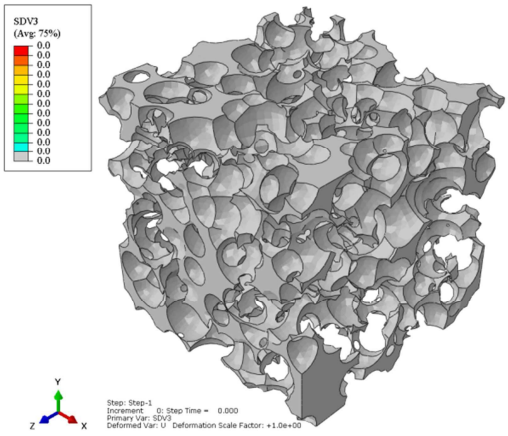

t = 0 s

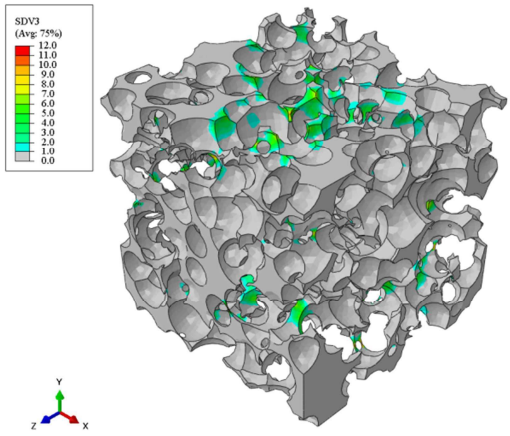

t = 1 s

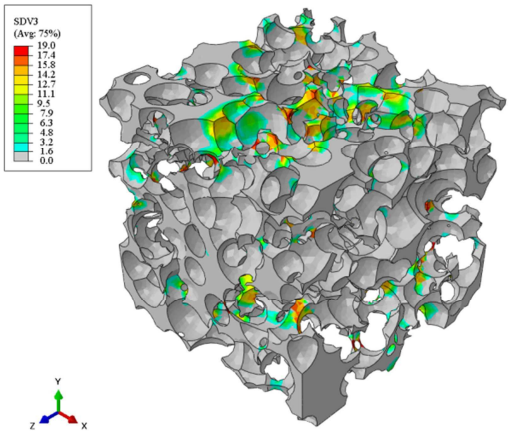

t = 2 s

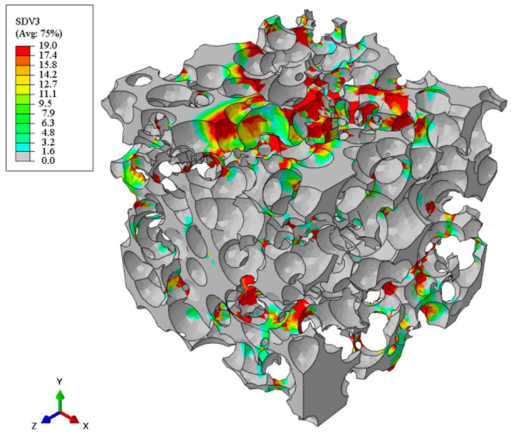

t = 3 s

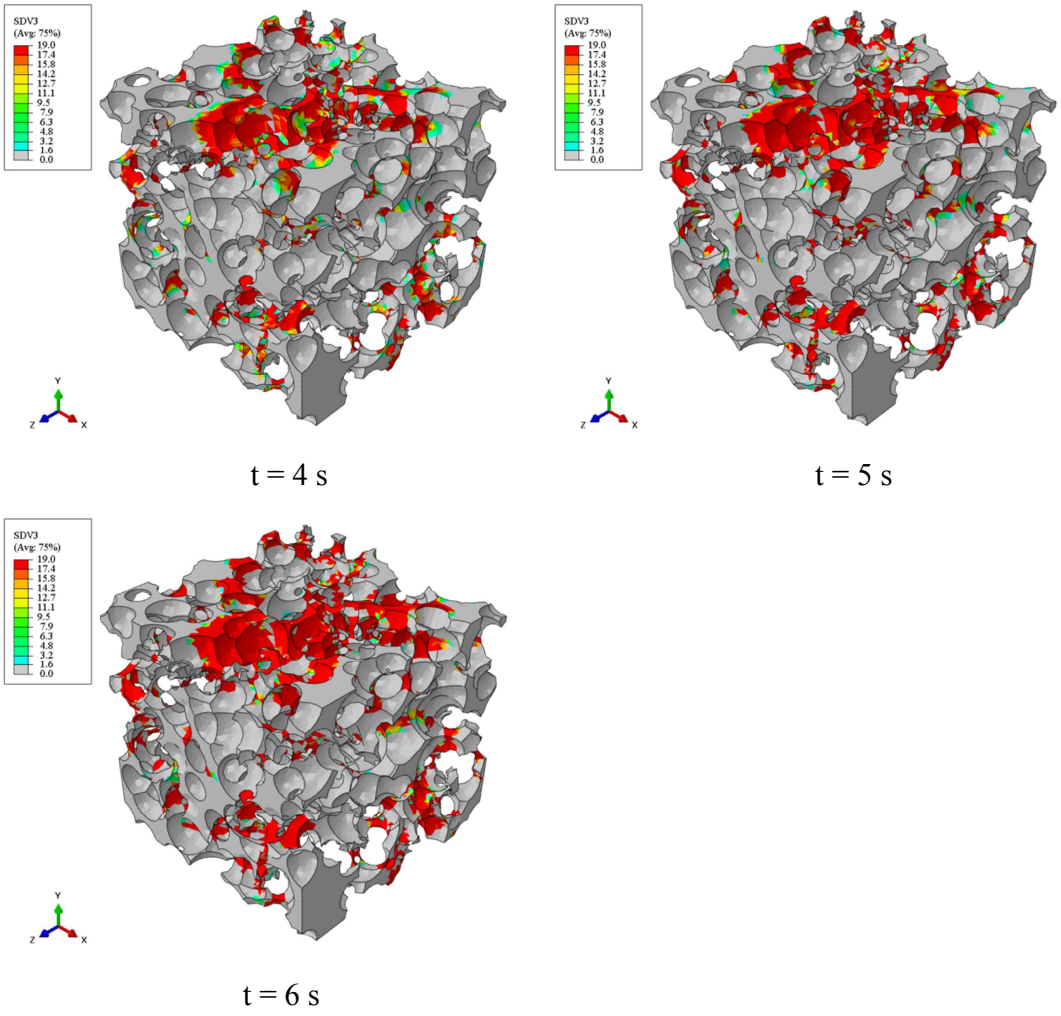

Fig. 4.6. Progress of pure brittle damage in the RVE of sound absorbing ceramic under compression

Two things can be observed clearly in the series above: progress of damage in the RVE and degradation of the stiffness in the damaged area. The legend points at the state variable which counts the number of stiffness degradations. Multiplication of its value with the degradation rate of 5% delivers the amount of stiffness degradation. Red color marks the areas with 10 % of the original stiffness. Physically, these are ruptured areas which are only able to carry reduced loading. The diagram of mean accumulated damage over time is plotted in Fig. 4.7.

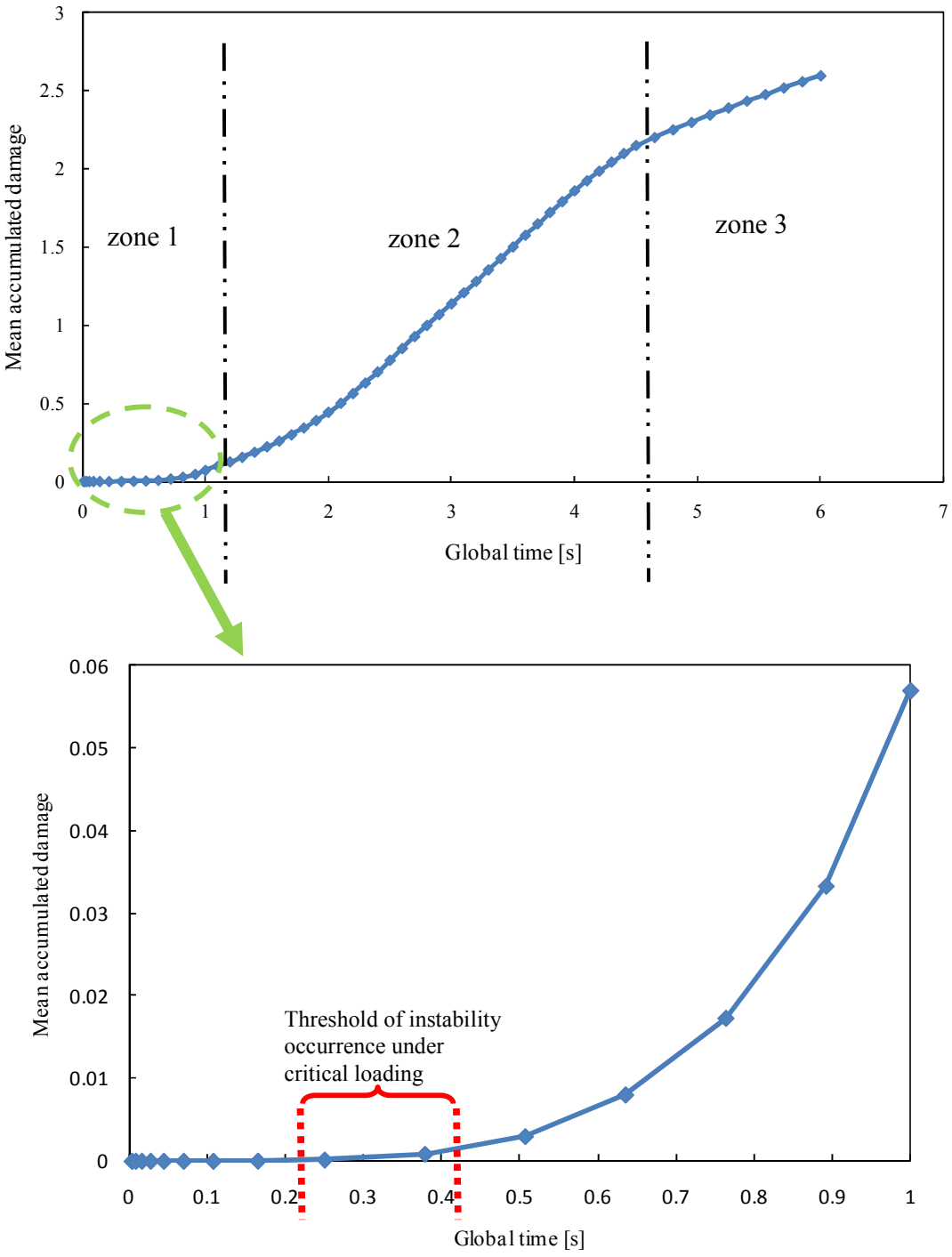

Fig. 4.7. Damage progress over computation time (top); localization of damage initiation threshold and critical loading (bottom)

The S-shaped plot can be divided in three zones. In the first zone, the pressure reaches a level which initiates the local instability in the material and thus initiating the pure brittle damage. This level of loading is named as critical loading. Generally, the condition of rupture is reached abruptly, and depending on the loading and material properties it can be occurred in zone 1 or 2. It means that the observed behavior in zone 2 or 3 does not have necessarily any analogous physical interpretation and could be considered here for the demonstration of the functionality of the user-subroutine. In zone 2, the damage progresses to other areas and also the load bearing capacity diminishes. Further computation shows in zone 3 a tendency to a condition where the mean accumulated damage remains constant as it is expected to be. Zooming out the zone 1 in the bottom plot of Fig. 4.7 shows clearly at what time the mean accumulated damage begins to deviate from the zero line. The marked up range (0.251 s - 0.379 s) expresses the time increments at which the exerted pressure reaches the critical value and the instability occurs. Fig. 4.8 shows again the bottom plot of Fig. 4.7 with smaller time increment.

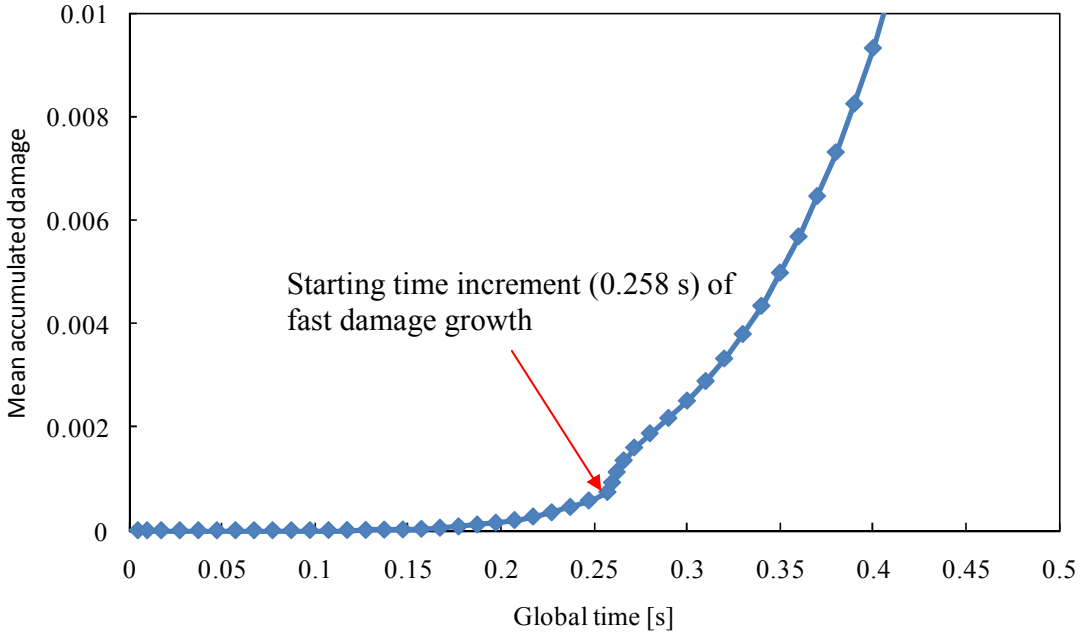

Fig. 4.8. Plot of mean accumulated damage over computation time with smaller time increment

Through smaller incrementation, this time range shrinks around the time value 0.258 s with sharp damage accumulation slope, which represents a compression of 7.74 MPa. This compression is the very critical strength of the ceramic RVE with 74% and its value reproduces the mean value of experimental compressive strength of 7.68 MPa with a relative error of 0.7%. In comparison to the value $\sigma_C = 8.6$ MPa , it gives a relative error of 10 %, which is reasonable in consideration of the assumptions and uncertainties by the prediction of unknown material parameters. Table 4.3 opposes the computed critical values to the mean values of strengths from experiment for different statistical distributions.

Table 4.3. Computed and experimental determined values of compressive strength

Distributions	**Compressive strength**	**Computed critical Pressure [Mpa]**
Normal	$\bar{R} = 7.68$ MPa	7.74
Weibull (least squares)	$R_0 = 8.6$ MPa	
Weibull (ML)	$R_0 = 8.54$ MPa	
Weibull (ML & biasing factor)	$R_0 = 8.84$ MPa	
Type I extreme value	$\mu = 6.43$ MPa	

This correlation between the computed and experimental compressive strength validates the analysis. The RVE is then subjected to a tensile load of 10 MPa. The results of damage condition are shown in Fig. 4.9.

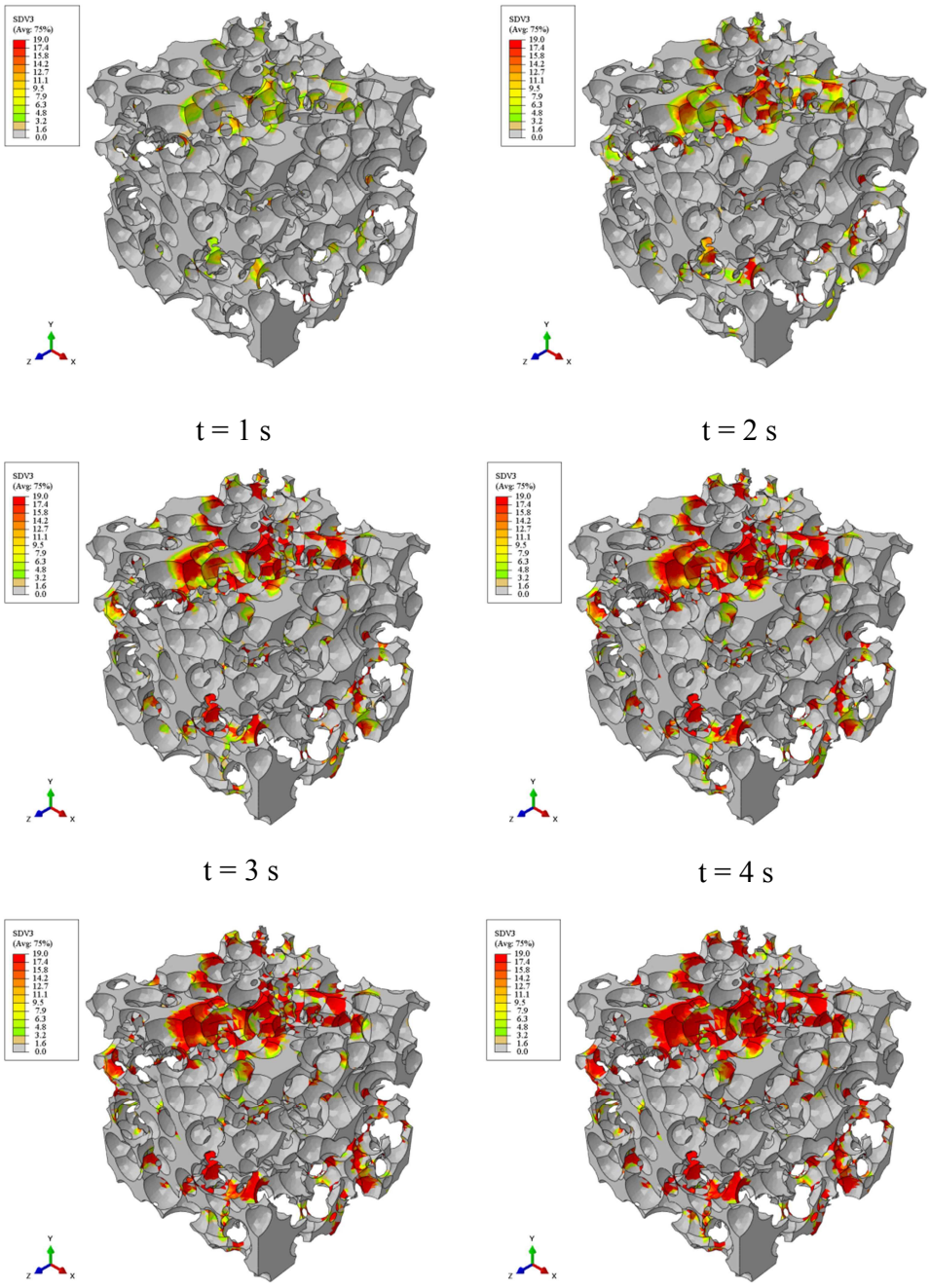

Fig. 4.9. Progress of pure brittle damage in the ceramic RVE under tension

Both progression of damage and degradation of stiffness under tension can be easily observed in Fig.4.9. For a comparison between both damage progress under compression and tension, it is better to plot the mean accumulated damage over the global computation time as shown in Fig. 4.10.

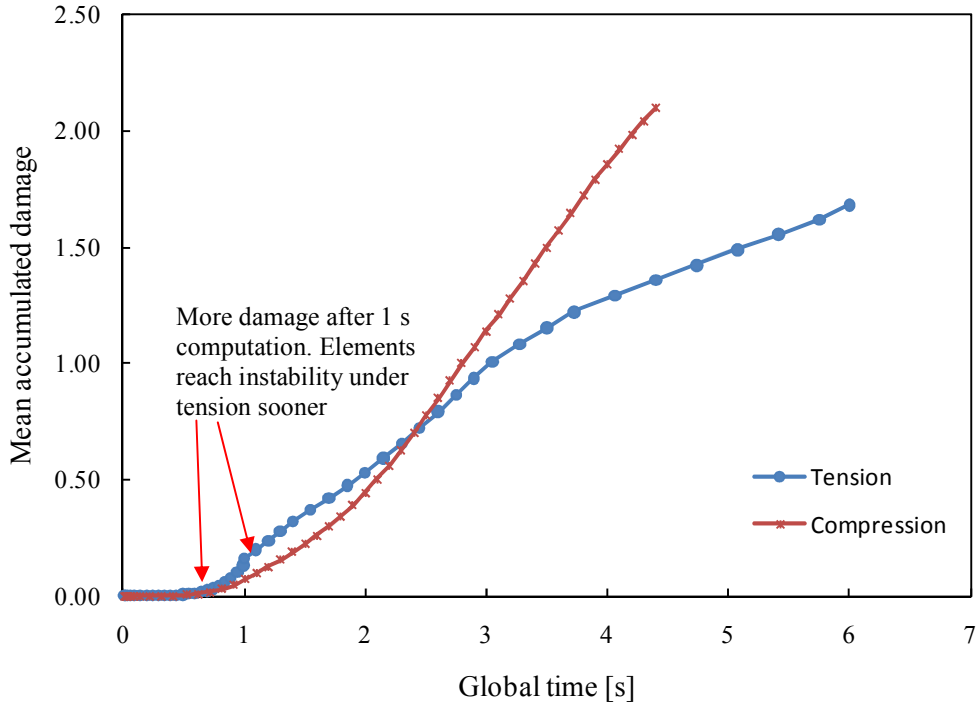

Fig. 4.10. Plot of damage progress under tension and compression

The progression of damage under tension is quite different from the one under compression. After 1 s computation, the mean accumulated damage under 10 MPa tensile load is considerably higher than the mean accumulated damage under pressure of 30 MPa. Further, at time t=1s the tension curves bend and rise with milder slope until the second and third bends at t=3 s and t=4 s. This behavior under tension is due to the microstructure. As a benchmark simulation for the user-subroutine, a monolithic ceramic RVE is subjected with the same material property under tension and compression. The plot of mean accumulated damage over time under both loadings is shown in Fig 4.11.

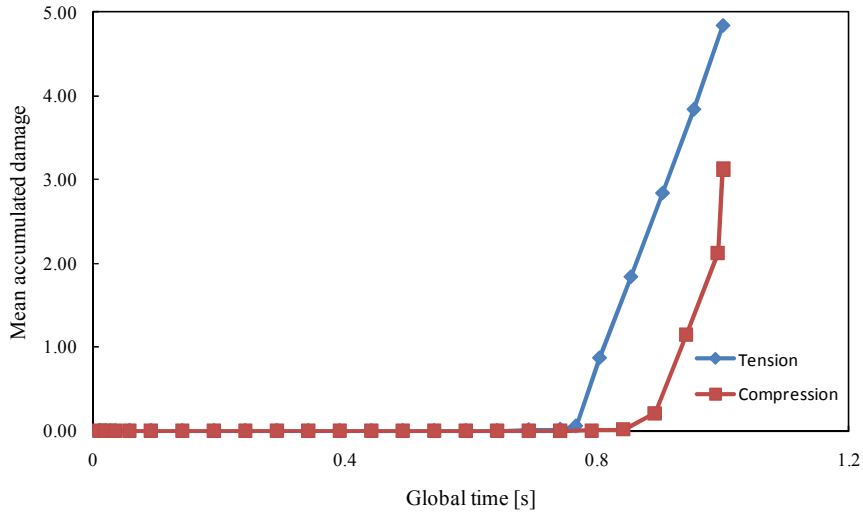

Fig. 4.11. Damage progress under tension and compression for a monolithic RVE

The slope of the blue curve in Fig. 4.11 is as it can be expected steeper than the slope of the red curve under compression. Here, the damage threshold is reached sooner under tension. Magnification of the Fig. 4.10 within 1 s computation time is depicted in Fig. 4.12.

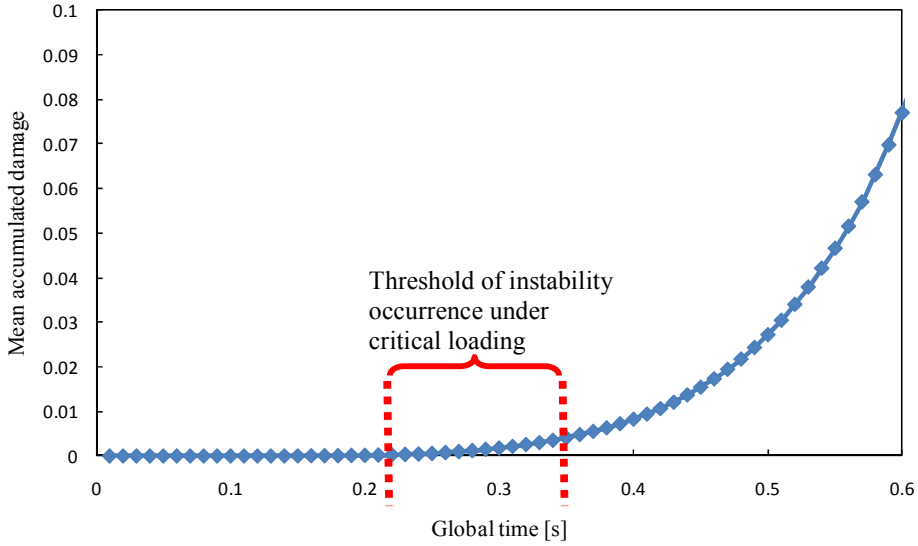

Fig. 4.12. Localization of rupture initiation threshold and critical loading

The marked up threshold lies between 0.251 s and 0.340 s which corresponds to tensile loading of 2.51 MPa and 3.4 MPa, respectively. This also confirms the correlation between critical tensile loading and tensile strength (rupture strength) from Table 3.3. Now, with the validation of the analysis, the influence of the microstructure parameters is investigated in five case studies, as listed in Table 4.4. For each case study one microstructure parameter varies which makes a total of 19 different RVEs.

Table 4.4. RVE's specifications of different case studies

RVE Case study	Porosity [%]	Pore size [mm]	Pore orientation
I	50 – 60 – 70	1.7	3D random
II	50	1.7 – 2.12 – 2.67	3D random
III	50	2.12	In loading direction : 2D random; aligned
			Perpendicular to loading direction: 2D random; fixed (along axis 1)
			3D random
IV	70	1.7 – 2.12 – 2.67	3D random
V	70	2.12	In loading direction : 2D random; fixed (along axis 1)
			Perpendicular to loading direction: 2D random; aligned
			3D random

In order to compare the influence of the microstructure quantitatively, the amount of mean accumulated damage after 1 s computation has been taken as quantitative comparable value, provided the RVEs have equal number of elements. Therefore, the mesh of each case study is so adjusted, that they contain almost the same number of elements for each RVE. The results of the case studies of Table 4.4 is presented in Table

4.5, in which PS stands for pore size, NE for number of elements, 2DP for 2D random orientation perpendicular to loading direction, FA for fixed orientation aligned axis 1 and the loading direction, MAD for mean accumulated damage and FP for fixed orientation along axis 1 and perpendicular to loading direction.

Table 4.5. Influence of microstructure on mean accumulated damage

Porosity 50%	PS=1.70 mm	PS=2.12 mm	PS=2.67 mm
MAD	0.0163	0.0386	0.0416
NE	248676	248769	248713
Porosity 70%	PS=1.70 mm	PS=2.12 mm	PS=2.67 mm
MAD	0.241	0.287	1.76
NE	248574	248551	248687

Porosity 50%	2D	2DP	FA	FP
MAD	0.117	0.267	0.239	0.494
NE	248766	248766	248771	248771
Porosity 70%	2D	2DP	FA	FP
MAD	0.364	0.947	0.497	0.561
NE	194341	194341	195109	195109

Over a certain porosity value, more damage is observed by bigger pores. The influence of porosity for a certain pore size, however, is more significant than the one of the pore size. At 70% porosity there is a big jump in the value of the mean accumulated damage from pore size 2.12 mm to pore size 2.67 mm, which lies in the interpenetration of more pores and consequently generation of more narrow struts. Further, changing the pore orientation from 3D random to 2D random (2D, 2DP) or even fixed orientation along one axis (FA,FP) do not reduce the damage. The damage is even more pronounced if the orientation of pores is perpendicular to the loading direction. Recalling from chapter 3, the mean field homogenization analysis predicted a higher modulus of elasticity for 2D

random orientation and fixed pore orientation aligned in the loading direction than the case of 3D random orientation. Though, for both cases, the calculated damage is more than in the case with 3D random pore orientation. This highlights the role of the investigation at the micro scale. The graphical presentations of the discussed results as well as the plot of mean accumulated damage are left to Appendix A.17 to A.31. Though, as a graphical example for this section, the damage condition of the case study I is presented in Fig. 4.13.

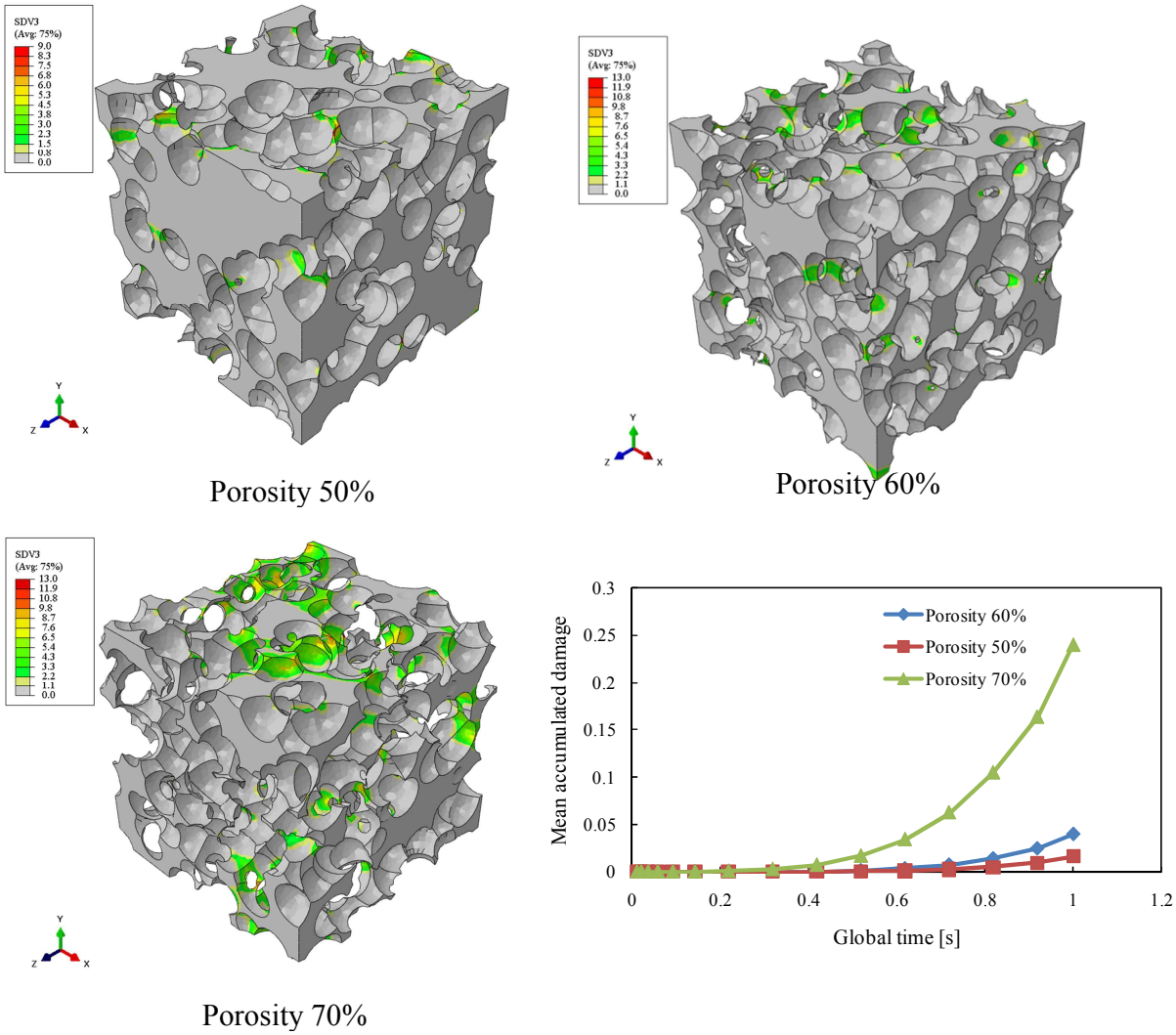

Fig. 4.13. Influence of porosity on the pure brittle damage of the RVEs

The drastic increase in the mean accumulated damage for the 70% porous RVE underlines the influence of the porosity. In order to reach this range of porosity, the pore interpenetration increase considerably and as a result, a complex geometry with narrow load bearing struts is generated. In order to exert more loads on the material, one could think of reinforcing the matrix with short fibers or of generating a structure with graded porosity.

SIMULATION ON THE REAL SIZE CERAMIC LINING TILE

In this section, it is of the interest to investigate the damage condition of the real size porous sound absorbing ceramic which lines the combustion chamber of the experimental set-up at the Faculty of Combustion of the Center of Applied Space Technology and Microgravity (ZARM). Fig. 4.14 shows the cylindrical combustion lining (at the left) as well as the design of the experimental set-up lined with the ceramic absorbers.

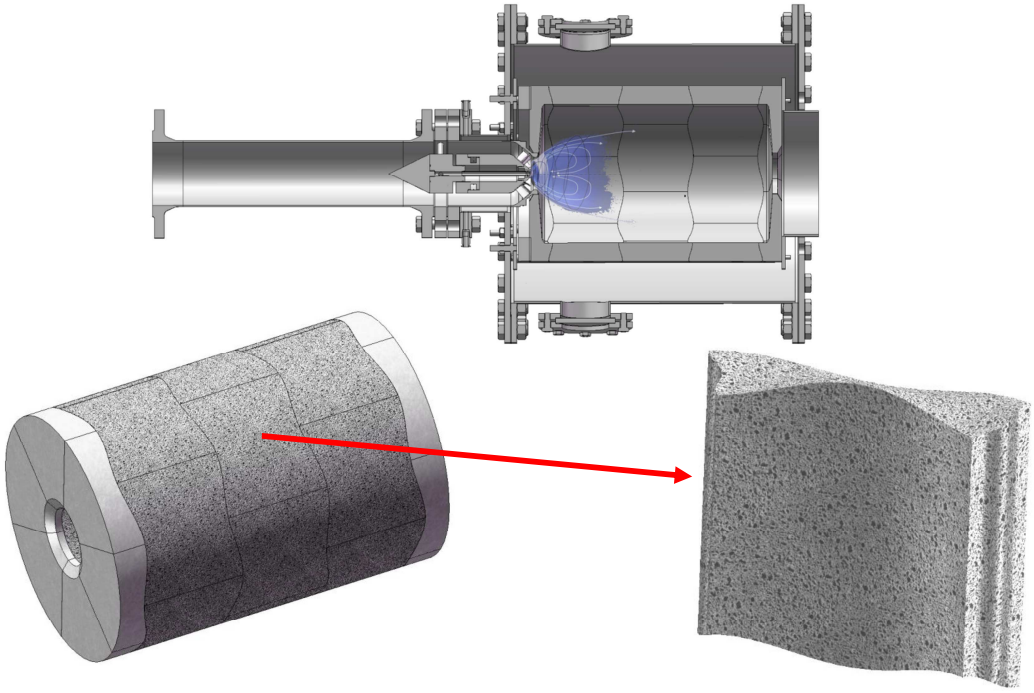

Fig. 4.14. Cylindrical combustion lining (bottom) and the design of the experimental set-up (top) [156]

The design allows thermal expansion of the cylindrical lining in axial and radial directions. A thermal analysis is carried out to see the temperature distribution in the lining tiles as well as to check the contact design of the lining tiles in terms of heat transfer. Having axial symmetric boundary conditions, the thermal loading is defined through adjusting film coefficients for hot air in the inner side and cooling air in the outer side building a temperature gradient of 1000°C over the thickness of lining tiles (30 mm). The result of the thermal analysis the actual contact design of lining tiles against the initial contact design with notch mechanism is presented in Fig. 4.15.

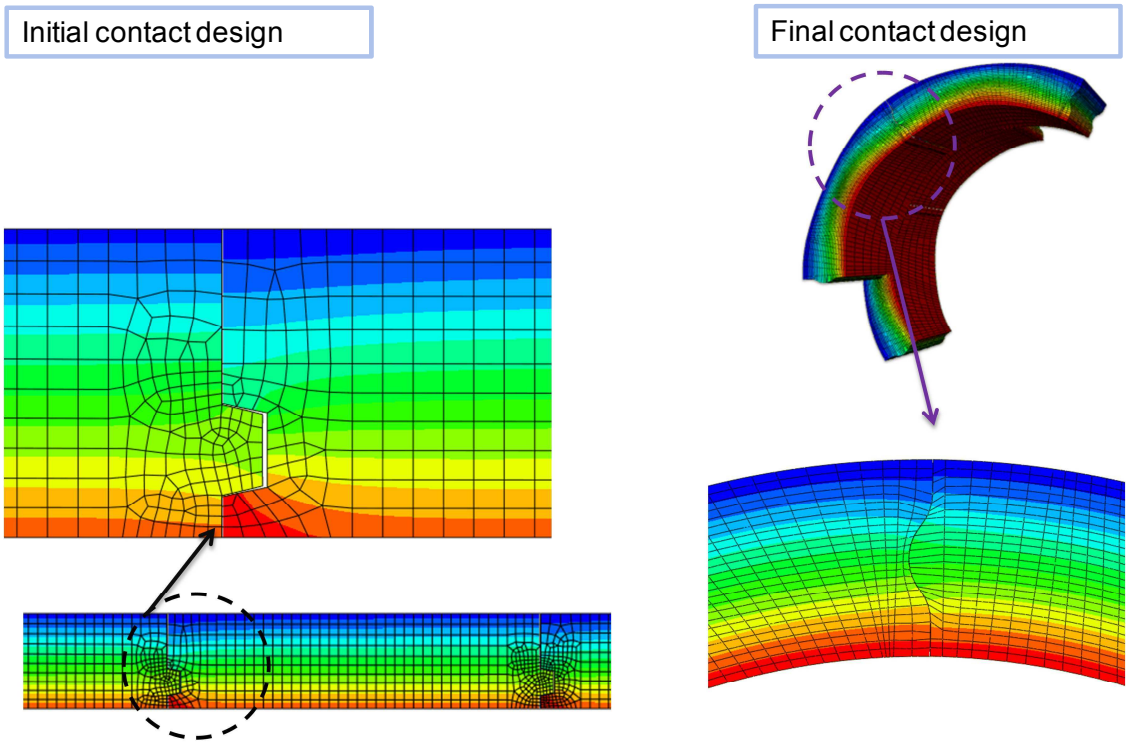

Fig. 4.15. Temperature distribution in initial and final lining lining tile contact design

The red color shows the hot front side of the lining tile for both designs. By the initial design, heat accumulation behind the notch is observed which is due to inappropriate positioning of the notch near the (hot) front of the lining tile. The actual design with sinusoidal free formed surface grants a very smooth heat transfer over the lining tile's

contact surfaces and hence there is not visible heat pile-up in the lining tiles. Taking the low thermal conductivity of these porous lining tiles, the design would be a good candidate for this application in terms of heat transfer.

The experimental set-up operates at the atmospheric pressure which means that the tiles are not directly under static overpressure. In case of sudden self excited thermoacoustic instability with high pressure amplitudes, undesirable Low Frequency Dynamics (LFD) are developed in the cylindrical combustion chamber which result in adverse mechanical loads on the tiles. Though, the study of damage behavior of the lining tiles is performed under static pressure conditions equivalent to the real dynamic loading condition. Under real geometrical boundary conditions, the critical pressure and areas under damage threat will be determined. The general workflow of damage analysis on the real size lining tiles is shown in Fig. 4.16.

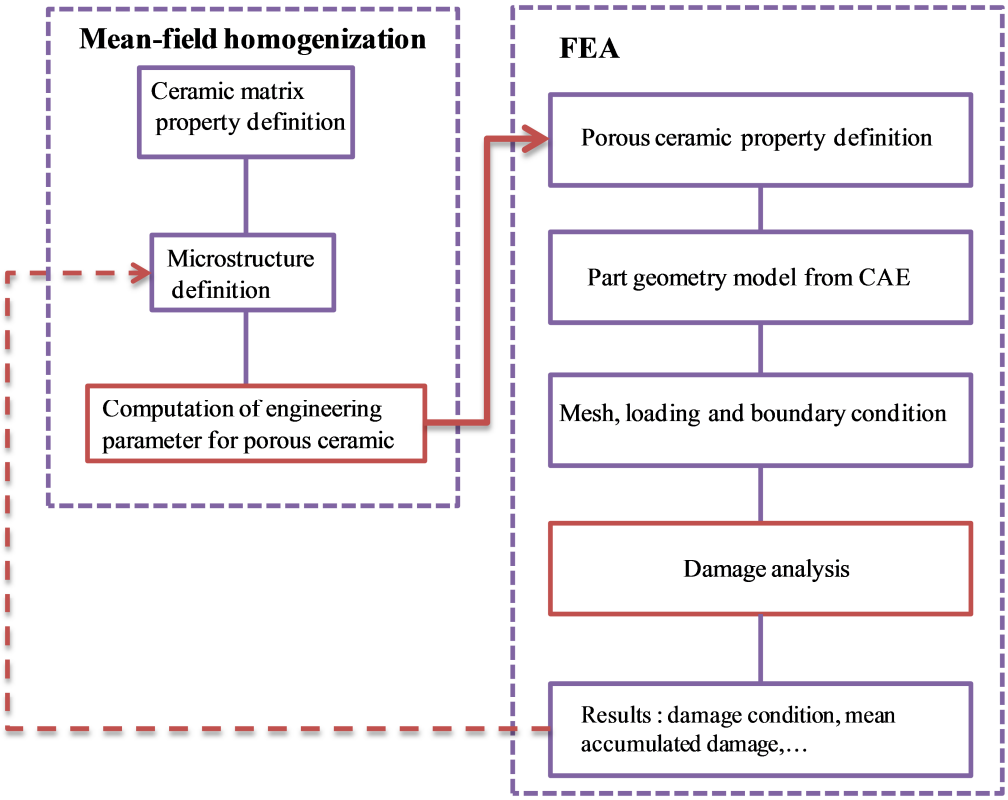

Fig. 4.16. Workflow of damage analysis and simulation on the real size ceramic lining tile

The application of the mean field homogenization method beside the finite element analysis (FEA) supports by the reverse engineering for the unknown material properties based on the available experimental properties, as well as allows the virtual compounding of different porous ceramics for the use in real size simulations. For the pure brittle damage analysis of the latter case, however, the ultimate strength of the compounded porous ceramic is still needed and should be determined from experiments. In order to avoid a wide range of experiments for the determination of the strength of different porous ceramic compounds, one may recall the GMR method used in the previous chapter. By performing experiments for some compounds of different porosity, and with the knowledge of the strength of ceramic matrix, the scale fractal parameter J would be determined. Subsequently, the ultimate strength for other compounds is predictable with reasonable accuracy for the pure brittle damage analysis at macro scale.

With the knowledge of the microstructure as well as the properties of the ceramic matrix from both experiment and reverse engineering, the engineering parameter for the sound absorbing lining tile at macro scale can be predicted through the mean field homogenization method. It means that the study on the real size ceramic lining tile considers the lining tiles as being homogenous. According to the pore orientation, the engineering parameters are given in ABAQUS for isotropic, transversely isotropic, orthotropic and fully anisotropic cases. For this ceramic the isotropic engineering parameters are considered due to the 3D random orientation of the pores. Table 4.6 lists the material properties of the 74% porous sound absorbing ceramic under study.

Table 4.6. Material property of porous sound absorbing ceramic

Property	$\mathbf{E = 4100\ MPa}$	$\boldsymbol{\nu = 0.20}$	$\boldsymbol{\sigma_U = 8.6\ MPa}$
Method of determination	Compression test	Reverse engineering	Compression test

After assigning the material properties to the geometry model as shown in Fig 4.17, the axial symmetry condition has been chosen and a pressure of 10 bar is subjected to the model as a start pressure for the determination of the critical loading for tiles.

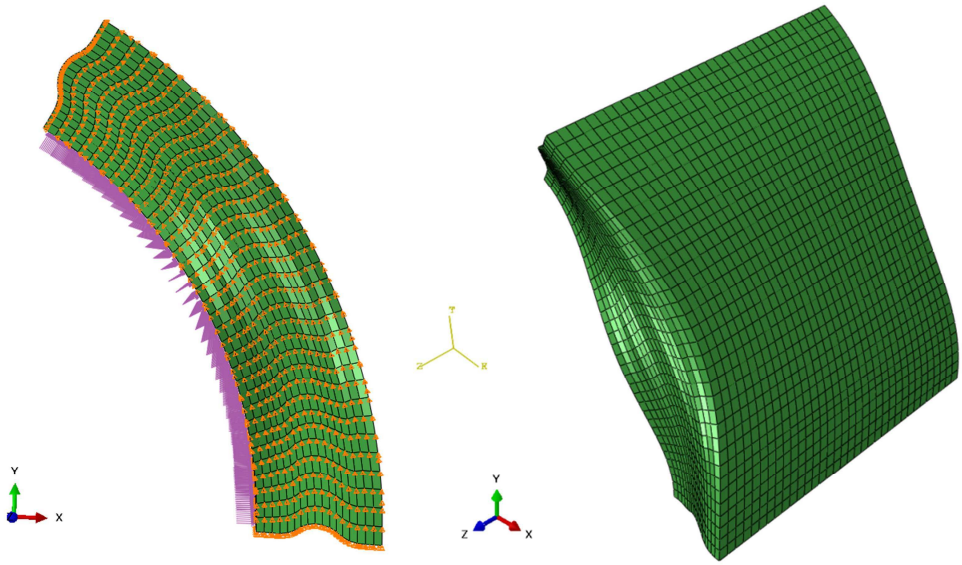

Fig. 4.17. Axial symmetry boundary condition (left) and mesh of the model (right)

The mesh includes 19652 brick elements of type C3D8. The first sign of damage is observed under 1.8 MPa pressure on the lining tile as shown in Fig. 4.18.

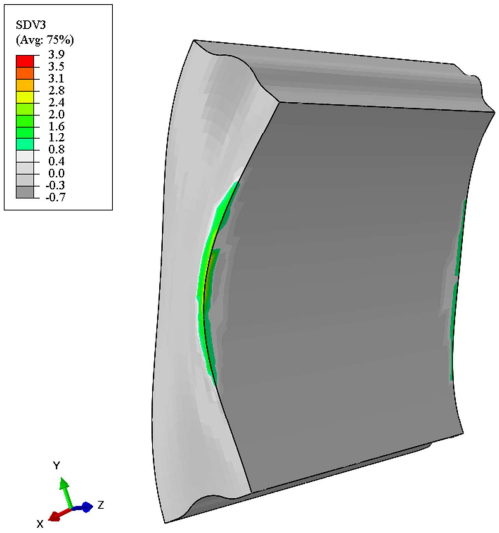

Fig. 4.18. First sign of damage in the lining tile under a pressure of 1.8 MPa

The damage initiation at both edges is due to the lack of material support by the neighboring tiles, which is the case in the real construction. Further increase of the pressure initiates brittle damage in the whole inner side of the tile, as Fig. 4.19 depicts for pressures up to 3MPa.

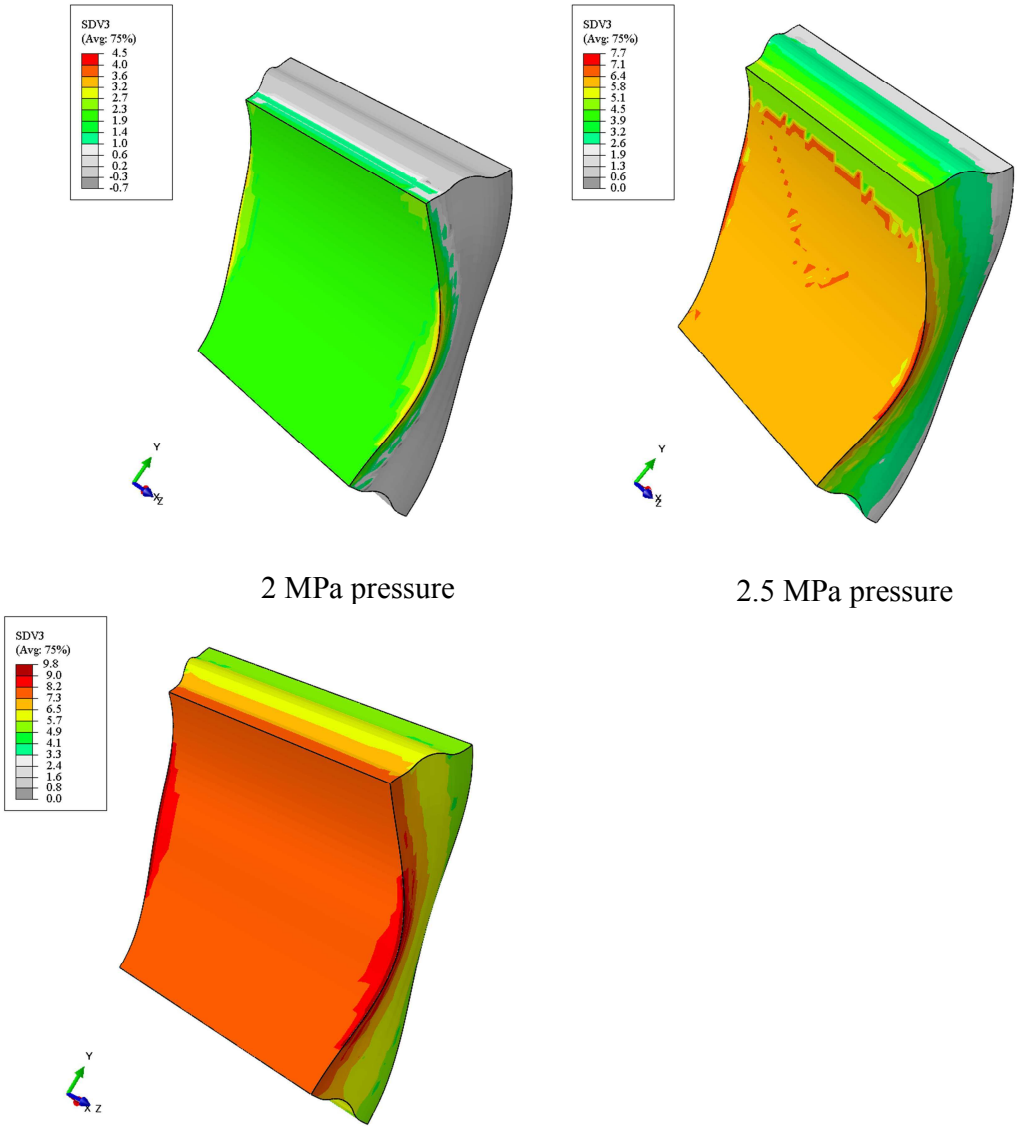

2 MPa pressure

2.5 MPa pressure

3 MPa pressure

Fig. 4.19. Progress of pure brittle damage in the lining tile due to pressure increase

In the case of a pressure 2 MPa as well as 3MPa, the damage is distributed uniformly in the whole inner side of the lining tile. Under 2.5 MPa pressure, however, it is visible how the red areas with higher number of stiffness degradation build up and finally, with a pressure increase to 3Mpa, distribute uniformly over the inner side of the lining tile. The plot of the mean accumulated damage under pressure in Fig. 4.20 proves the graphical presentation above.

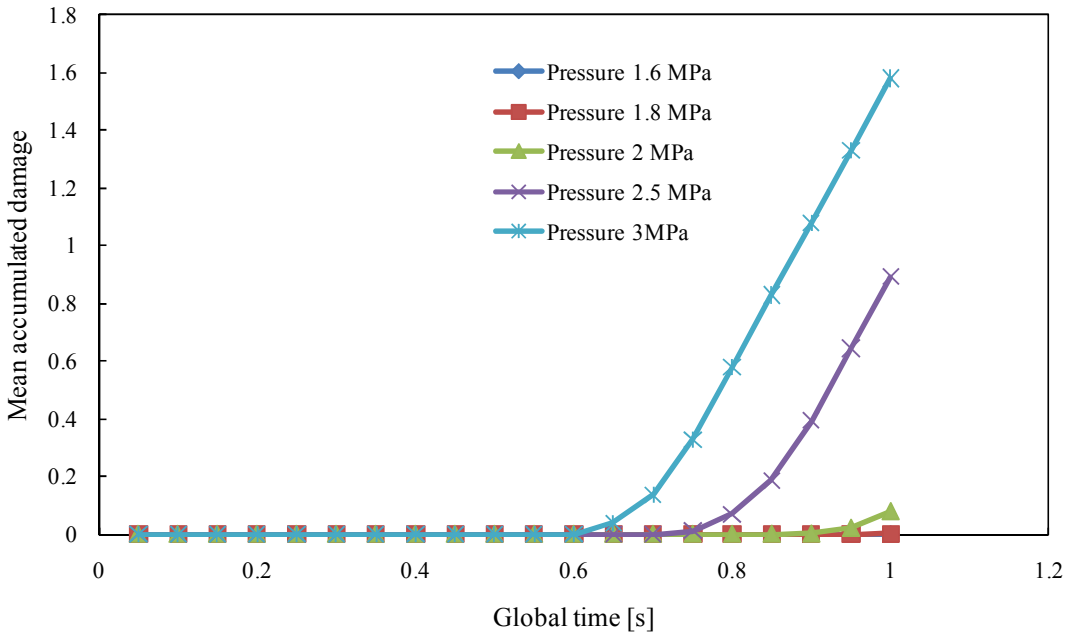

Fig. 4.20. Damage progress in a lining tile under different pressure

After initiation of damage under a pressure of 1.8 MPa, the damage progresses rapidly by further increase of pressure which is also expectable for the lining tile. Taking the lack of material support behind both edges of the lining tile as well as considering the plot in Fig. 4.20, it would be more appropriate to accept the pressure of 2 MPa as the critical pressure for the lining tile.

The simulation on the real size sound absorbing ceramic lining tile proves the applicability of the lining tile design in terms of heat transfer and predicts the critical

pressure under which pure brittle damage in the lining tile initiates with the existing boundary condition in the experimental set-up.

Summary

Implementation of sound dissipation and passive damping properties in the isolating ceramic has become of great importance due to their potential application areas as liners in the combustion chamber of gas turbines or in exhaust silencers, and thus intrigued a new wave of investigations in areas of material development, material characterization, modeling and numerical simulation. A new production technique based on the freeze gelation process provides near-net-shape sound absorbing ceramic components containing high fraction of open porosity. The components present in contrast to the traditional fibrous sound absorbing materials a combination of good sound absorption, high temperature resistance, chemical inertness and material strength.

The present investigation is concerned with this new porous sound absorbing ceramic and focuses on its mechanical behavior with consideration of microstructural parameters like porosity, pore size, pore orientation; and predicts the pure brittle damage of this ceramic material at micro and macro scale. It studies the applicability of such ceramics as insulation liners for the combustion chambers and gives insight into further material improvements in terms of mechanical strength.

At the first stage, the physical, mechanical and thermal properties of the new ceramic material are characterized through a series of tests and measurements. Compression tests at both room and high temperature as well as four-point bending tests at room temperature determine the compressive and bending strengths as well as the modulus of elasticity and the material behavior at increasing temperature. A considerable, almost nearly linear decrease of compressive strength was observed with increasing temperature. The reason for this behavior is due to the behavior of the glass content of the material during the temperature increase. Furthermore, the fits of fracture strengths of the material to the Normal, Weibull and Type I extreme value distributions are investigated. In the case of compression strengths, all the Weibull distributions and the Type I distribution fits the data considerably good, whereas the Normal distribution gives a relative poor fit. Considering the fracture strengths from the bending test, the Type I distribution fits the data much better than the other distributions. The fits of least squares

for both data sets are slightly better than the results from the maximum-likelihood method, which is preferable due to some statistical reasons. The comparison, however, is based on two sets of data and relative small number of tests, and thus the conclusion is tentative to be generalized for such porous ceramics.

The characterization is then expanded to other properties such as porosity, density, thermal conduction coefficients and thermal expansion coefficients. The fact is, depending on the experimental procedure and limitations, either the property of the porous specimen or the properties of ceramic matrix are available which are needed for further numerical investigation at both micro and macro scale. A resolution for this is the prediction of the unknown properties with the use of mean-field analytical material modeling. The method further provides an insight into the change of the material behavior of the porous absorber with respect to the change in structural quantities. This insight is of great importance regarding the material development, material optimization, experiment cost and time reduction.

Following the experimental characterization, the simulation and the damage analysis of the porous ceramic sound absorber are performed firstly at micro scale with a direct finite element simulation of the representative volume elements (RVE) and then at macro scale with the simulation of the real size ceramic lining tile, both with the help of the finite-element package ABAQUS. For the damage analyses, a degradation model is implemented in a predefined user-subroutine of ABAQUS. It is based on the three dimensional rupture criterion and describes the pure brittle damage under mechanical, static and quasi-static loadings. Once the rupture occurs, in the damaged area, the ceramic material is only able to bear reduced loading. This is implemented by a stiffness degradation regime for the pure brittle damage due to its numerical benefits.

Profound analyses of the damage behavior with respect to some microstructural parameters like porosity prerequisites the knowledge of compressive and tensile strengths of the ceramic matrix, which is not easily available through experiments. These are reverse engineered from the determined porous ceramic compressive and tensile strengths by an analytical approach based on the Generalized Mixture Rule (GMR). The

applicability of this approach is examined with the available material properties, which present a reasonable response within an acceptable relative error. This approach, however, still needs some physical validations and a profound analysis in terms of analytic mechanics and its physical meaning. The critical loading of a RVE can be computed from the knowledge of predicted ceramic matrix strengths with an arbitrary combination of porosity, pore size and pore orientation using direct finite-element simulations with the implemented subroutine. The computed critical loading serves as ultimate stress of the model for the real size ceramic lining tile.

The process of pure brittle damage analysis is further validated through the simulation of compressive tests on an RVE model with the same porosity and spherical pores as in the ceramic samples. The simulation results give a critical pressure for the whole RVE which can be easily correlated with the compressive strength determined from the tests. The same correlation is also made between the rupture strength and the critical tensile stress computed on the same RVE. A precise prediction in the wake of this modeling demands also calibration of the process with more experimental data at both room and high temperatures. On the real size lining tile, the thermal analysis proves the actual lining-tile design in terms of heat transfer. Under the geometrical boundary condition in the experimental set-up, the mechanical analysis determines the critical pressure under which the first signs of damage are observable.

The present results demonstrate the application potential of these sound absorbing ceramic as lining tile in terms of mechanical strengths, predict their brittle damage behavior considering the microstructure, and provide a base for further material developments and numerical investigations. The validation of applicability to line the combustion chambers in terms of sound absorption will be investigated with an experimental set-up at the Faculty of Combustion of the Center of Applied Space Technology and Microgravity (ZARM).

The experimental and numerical results in this contribution point at some further investigations regarding material developments and material behavior. Reinforcement of porous sound absorbing ceramic with short fibers or producing sound absorber with

graded porosity would present more strength and hence more attractive for the application at higher loading condition. The user-subroutine could be extended for the coupled computation of the thermoelastic behavior of ceramic sound absorbers. This work paves the way for further upcoming investigations in terms of thermal shock and creep behavior of porous sound absorbing ceramics.

Appendix

A.1 Temperature influence on the compressive strength

Temperature [°C]	Specimen	Force at failure [N]	Temperature [°C]	Specimen	Force at Failure [N]
200°C	CHT1*	2351	1100°C	CHT18	1247
	CHT2	2060		CHT19	1232
	CHT3	3028		CHT20	1192
	CHT4	1140		CHT21	598
	CHT5	1915		CHT22	592
600°C	CHT6	1957	1200°C	CHT23	491
	CHT7	1667		CHT24	1035
	CHT8	786		CHT25	825
	CHT9	1902		CHT26	933
900°C	CHT10	1615		CHT27	955
	CHT11	1559			
	CHT12	919			
1000°C	CHT13	443			
	CHT14	1117			
	CHT15	1000			
	CHT16	1422			
	CHT17	1266			

- CHT: Cylindrical specimen, High temperature

A.2 Results of the compression test at room temperature

Sample	Temperature [°C]	Diameter [mm]	Height [mm]	Load at failure [N]	Failure stress [MPa]	Modulus of elasticity [MPa]
CRTI1	23	19.8	24.9	3104	10.09	1845.50
CRTI2	23	19.8	24.9	3502	11.38	1344.90
CRTI3	24	19.8	24.9	3480	11.31	3171.40
CRTI4	23	19.8	24.8	1469	4.77	1437.80
CRTI5	23	19.8	24.8	2613	8.49	3452.30
CRTI6	23	19.8	24.8	3104	10.09	4101.60
CRTI7	23	19.8	24.8	3273	10.64	3895.10
CRTI8	23	19.8	24.8	1631	5.30	2443.20
CRTI9	23	19.8	24.8	1484	4.82	2054.90
CRTI10	24	19.8	24.8	1975	6.42	3579.90
CRTI11	24	19.8	24.8	3698	12.02	4821.10
CRTII1	23	19.8	24.8	2133	6.93	1636.30
CRTII2	23	19.8	24.8	1146	3.72	1862.60
CRTII3	23	19.8	24.8	2159	7.02	3164.50
CRTII4	23	19.8	24.8	2370	7.70	2120.40
CRTII5	24	19.8	24.6	1590	5.17	2049.60
CRTII6	23	19.8	24.6	2049	6.66	2362.90
CRTII7	23	19.8	24.6	2727	8.86	3190.60
CRTII8	23	19.8	24.6	1233	4.01	2106.70
CRTII9	23	19.8	24.6	2504	8.14	2689.20

A.3 Results of four-point bending test at room temperature

Sample	Width [mm]	Height [mm]	Area [mm^2]	Force [N]	Strength [MPa]
BRT01	14.40	10.27	147.89	73.23	5.06
BRT02	11.60	10.60	122.96	26.99	2.17
BRT03	11.70	10.60	124.02	62.88	5.02
BRT04	13.60	10.40	141.44	39.01	2.78
BRT05	11.90	10.30	122.57	36.04	3.00
BRT06	13.20	10.90	143.88	34.91	2.34
BRT07	13.20	11.10	146.52	38.30	2.47
BRT08	14.10	10.70	150.87	41.50	2.70
BRT09	12.50	10.00	125.00	35.26	2.96
BRT10	12.00	10.00	120.00	42.32	3.70
BRT11	11.80	10.20	120.36	31.89	2.73
BRT12	11.70	10.00	117.00	40.06	3.60
BRT13	13.00	10.70	139.10	34.84	2.46
BRT14	12.40	10.70	132.68	44.18	3.27
BRT15	12.40	11.03	136.77	34.86	2.43
BRT16	12.20	10.30	125.66	33.12	2.69
BRT17	11.70	8.70	101.79	33.56	3.98
BRT18	12.80	10.02	128.26	30.74	2.51
BRT19	12.40	9.50	117.80	39.98	3.75
BRT20	13.30	10.20	135.66	56.97	4.32
BRT21	11.30	10.20	115.26	28.03	2.50

A.4 Specific heat capacity of the ceramic matrix (Specimen HC01)

Temperature [°C]	Test C_P [J/g.°C]	Repeat 1 C_P [J/g.°C]	Repeat 2 C_P [J/g.°C]	Repeat 3 C_P [J/g.°C]	Repeat 4 C_P [J/g.°C]	Mean value C_P [J/g.°C]
70	0.856	0.858	0.817	0.822	0.920	0.854
80	0.868	0.862	0.800	0.834	0.923	0.857
90	0.874	0.868	0.806	0.840	0.927	0.863
100	0.874	0.882	0.802	0.841	0.944	0.869
110	0.884	0.882	0.829	0.846	0.952	0.879
120	0.892	0.883	0.824	0.854	0.949	0.880
130	0.893	0.886	0.825	0.856	0.953	0.883
140	0.896	0.885	0.828	0.860	0.956	0.885
150	0.899	0.888	0.829	0.862	0.958	0.887
160	0.899	0.889	0.831	0.864	0.963	0.889
170	0.901	0.892	0.832	0.865	0.965	0.891
180	0.903	0.894	0.838	0.867	0.970	0.894
190	0.907	0.895	0.839	0.869	0.976	0.897
200	0.910	0.899	0.842	0.873	0.981	0.901

A.5 Cumulative fracture versus bending strength

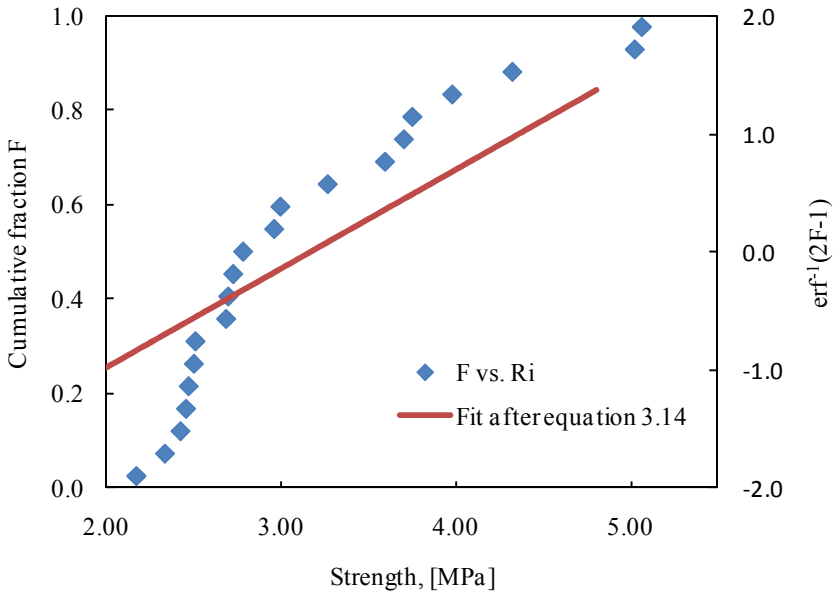

A.6 Weibull plot for bending strengths

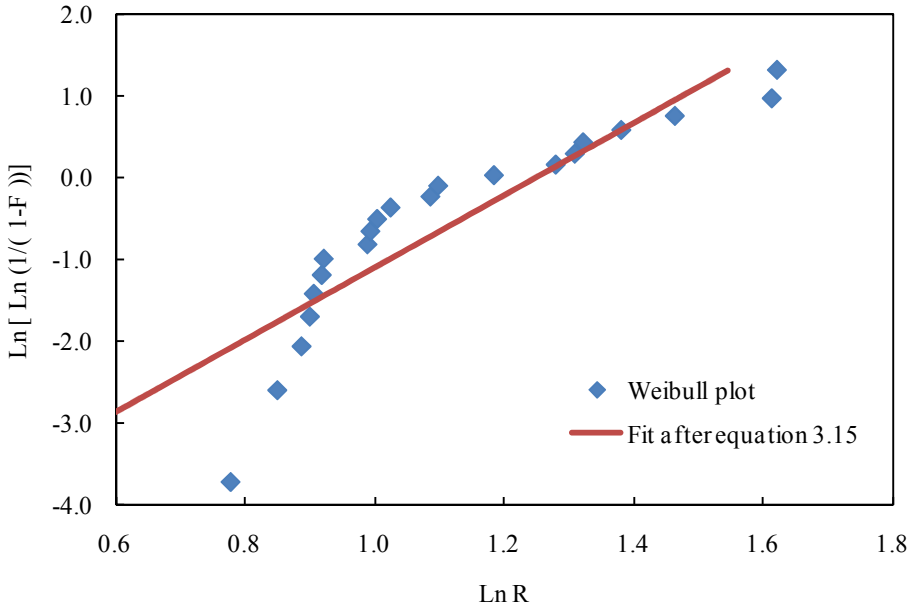

A.7 Type I extreme value plot for bending strengths

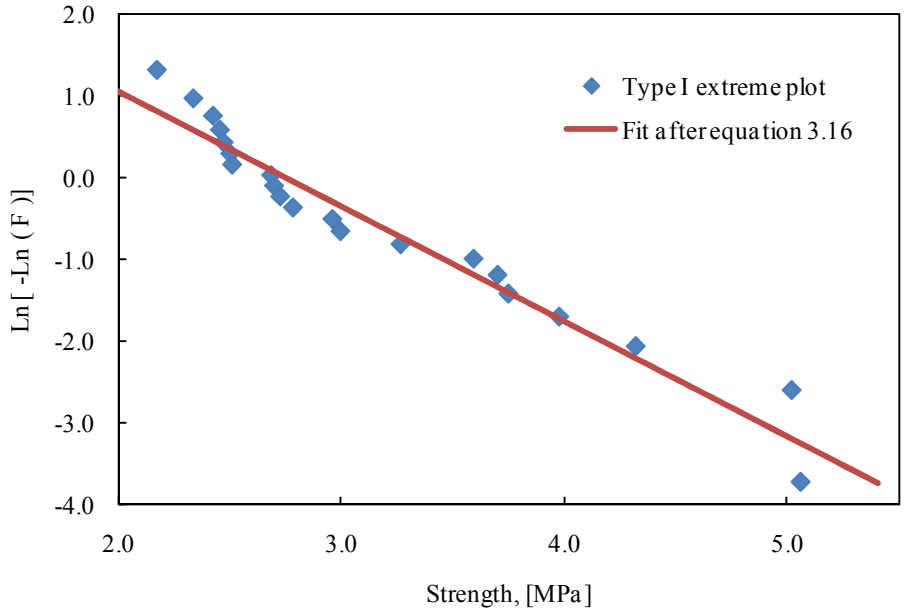

A.8 Shear modulus vs. porosity for fixed orientation of pore along axis 1 and different aspect ratios

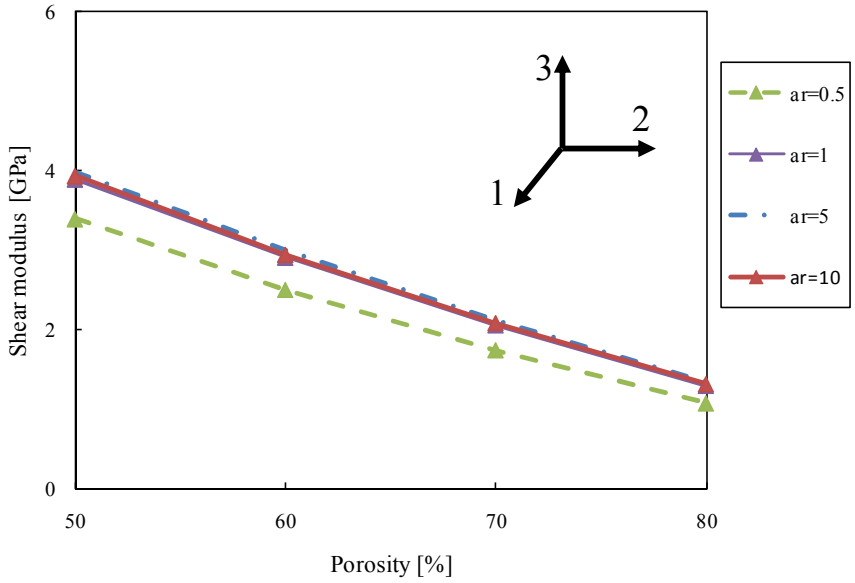

A.9 Shear modulus in plane-(1,2) vs. porosity for 2D random pore orientation and different aspect ratios

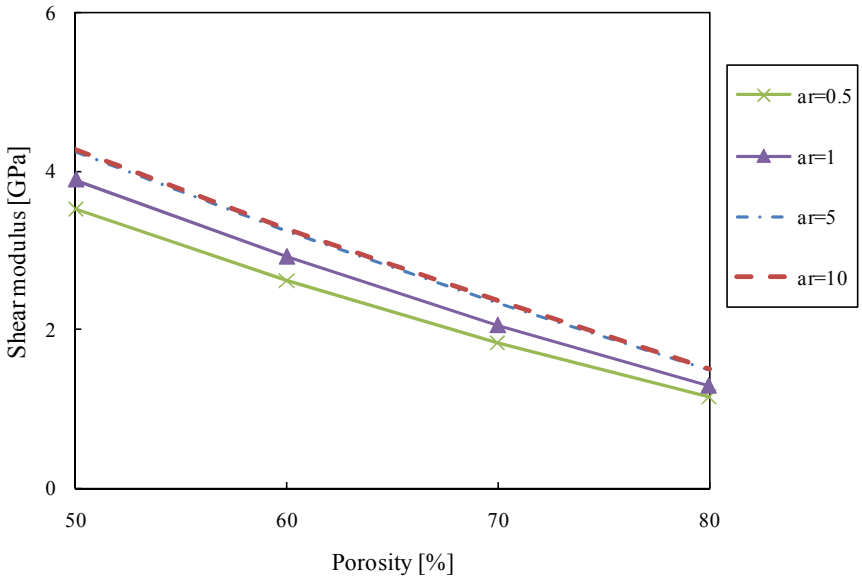

A.10 Shear modulus vs. porosity for 3D random pore orientation and different aspect ratios

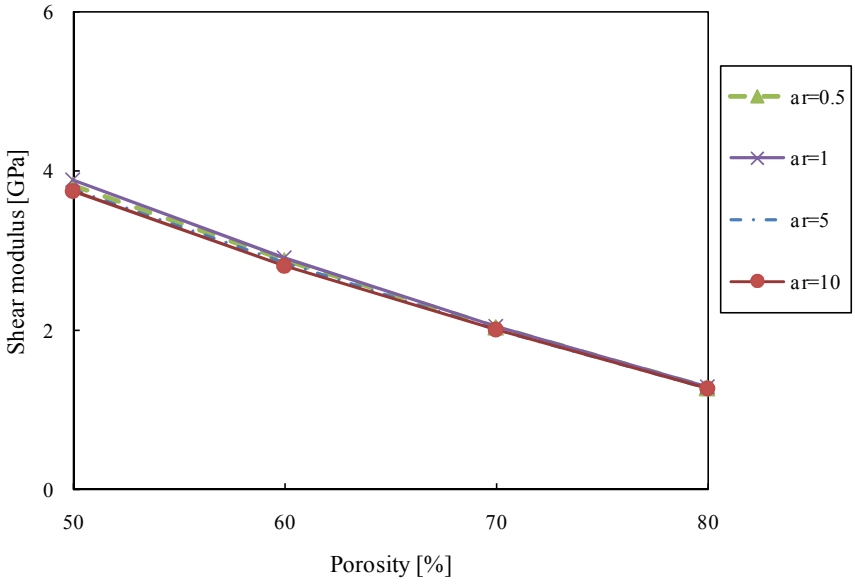

A.11 Shear modulus in plane perpendicular to axis 1 vs. porosity for fixed pore orientation along axis 1 and different aspect ratios

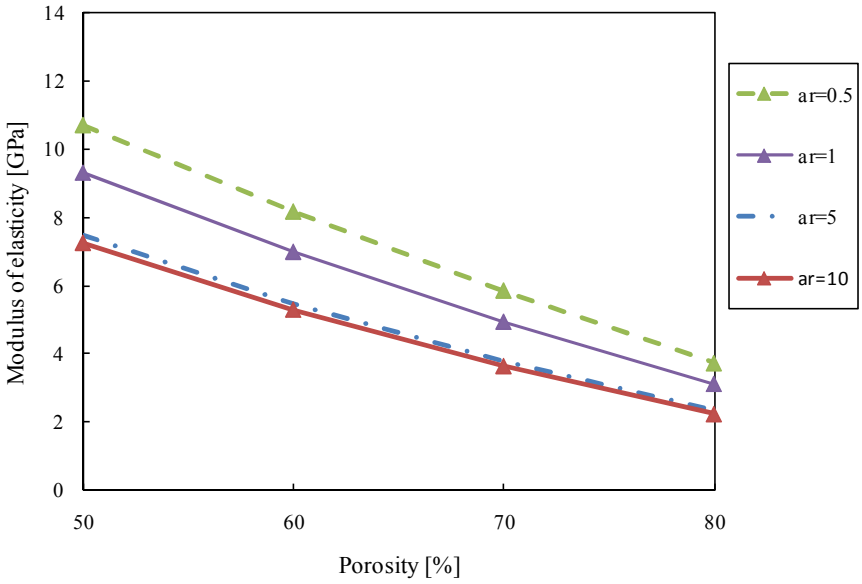

A.12 Shear modulus in plane orthogonal to the (1,2)-plane vs. porosity for 2D random pore orientation and different aspect ratios

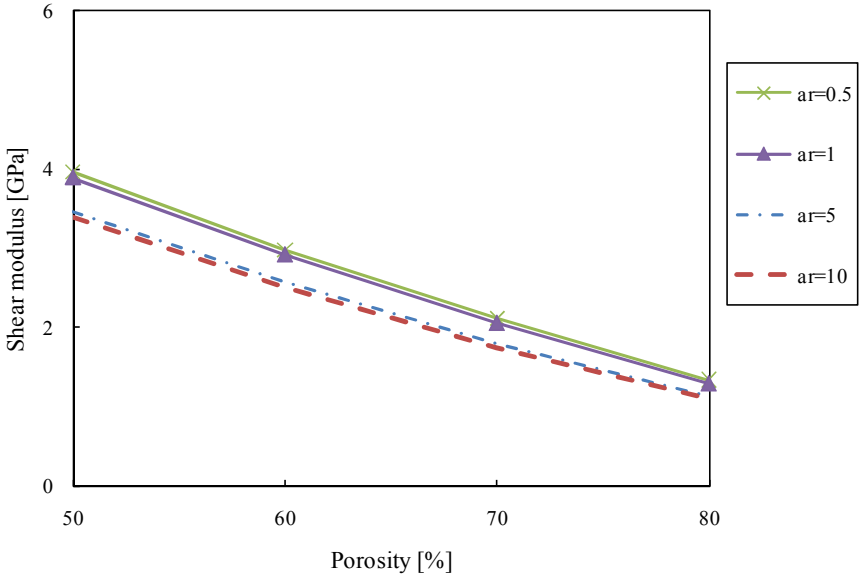

A.13 Modulus of elasticity perpendicular to loading direction vs. porosity for fixed pore orientation along axis 1 and different aspect ratios

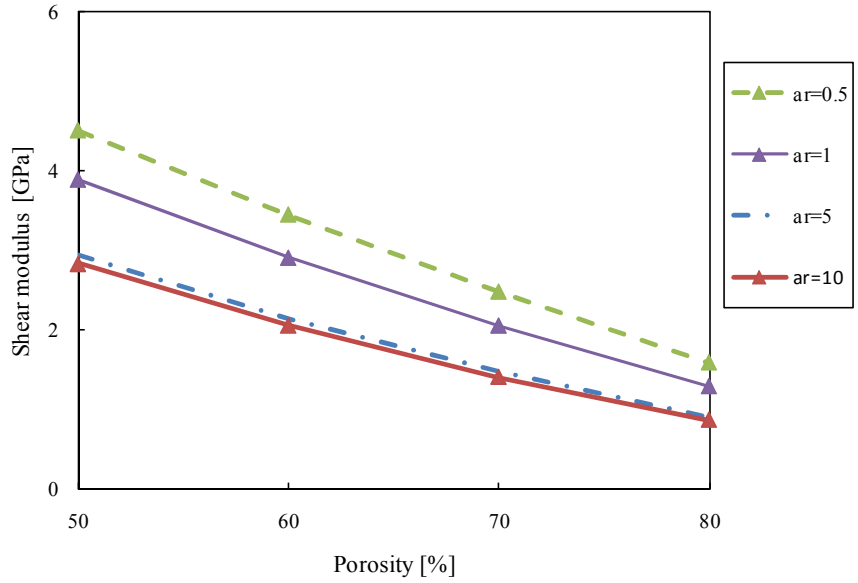

A.14 Modulus of elasticity along axis 3 vs. porosity for 2D random pore orientation and different aspect ratios

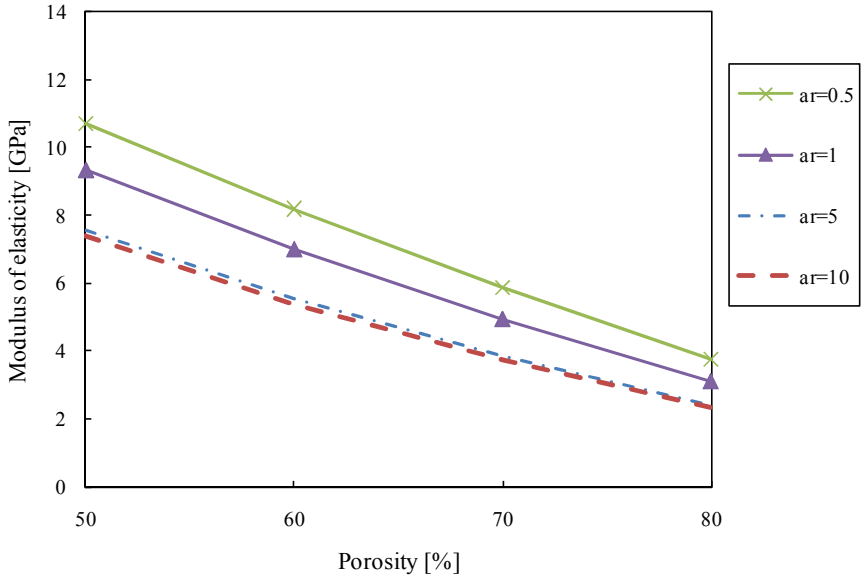

A.15 Thermal conductivity of the porous sound absorbing ceramic in direction perpendicular to the axis 1 vs. porosity for fixed pore orientation along axis 1 and different aspect ratios

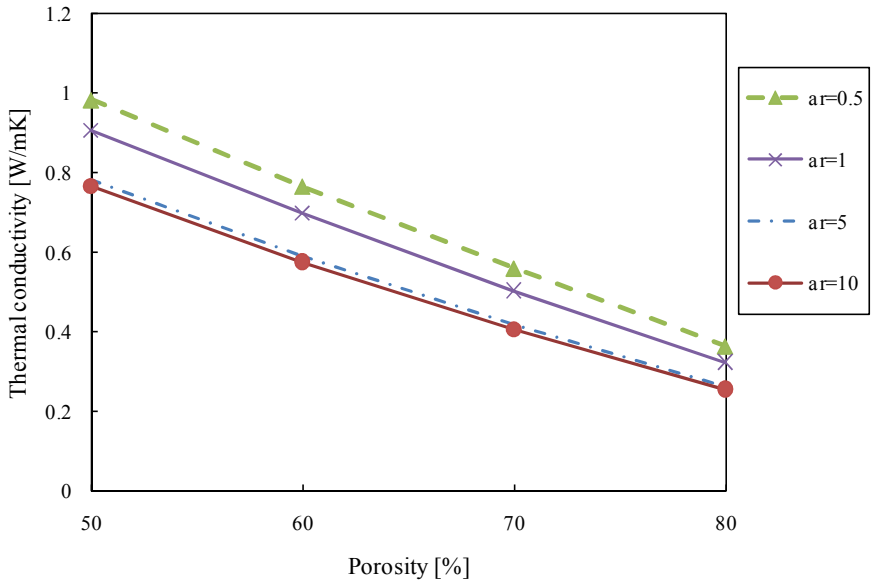

A.16 Thermal conductivity of the porous sound absorbing ceramic along axis 3 vs. porosity for 2D random pore orientation and different aspect ratios

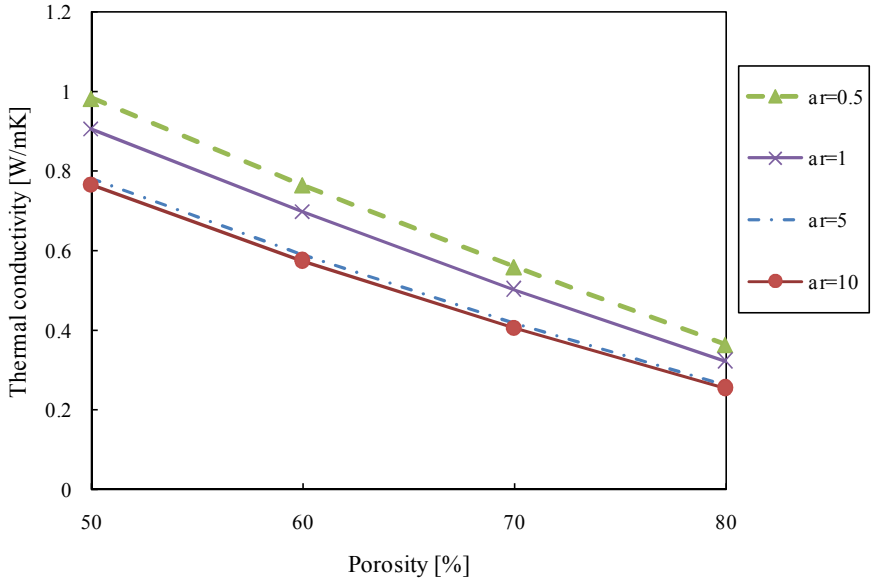

A.17 Pure brittle damage condition for RVE with PS=1.70 mm (50% porosity)

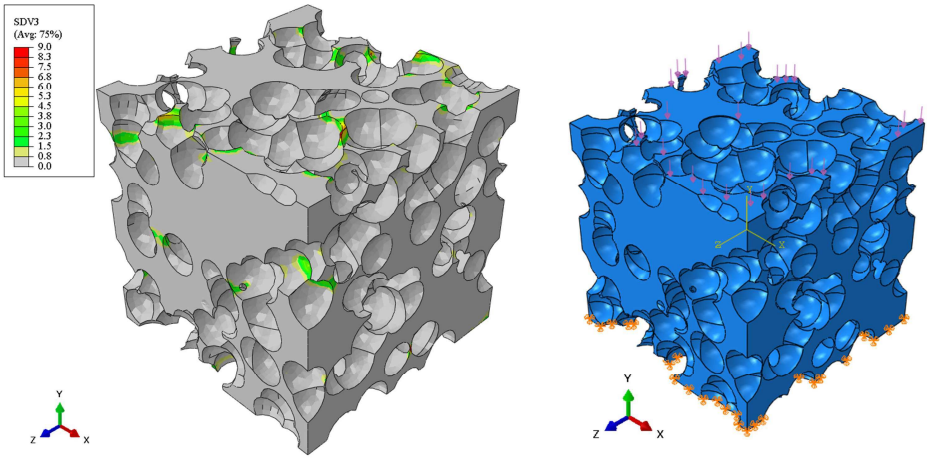

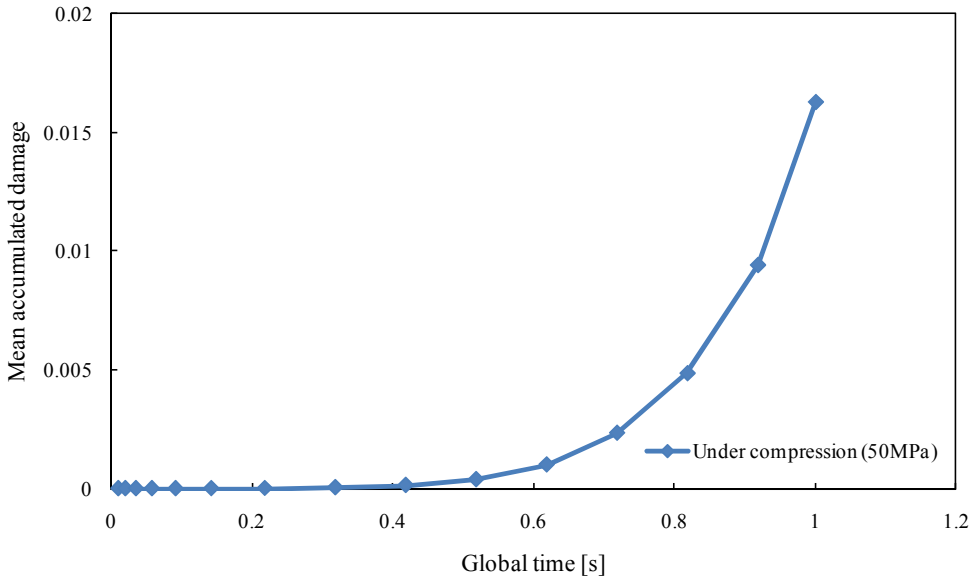

A.18 Pure brittle damage condition for RVE with PS=2.12 mm (50% porosity)

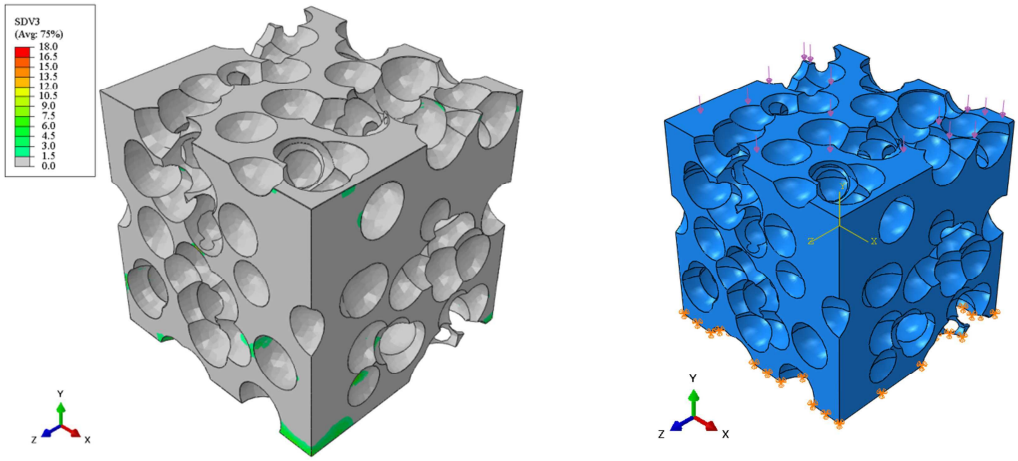

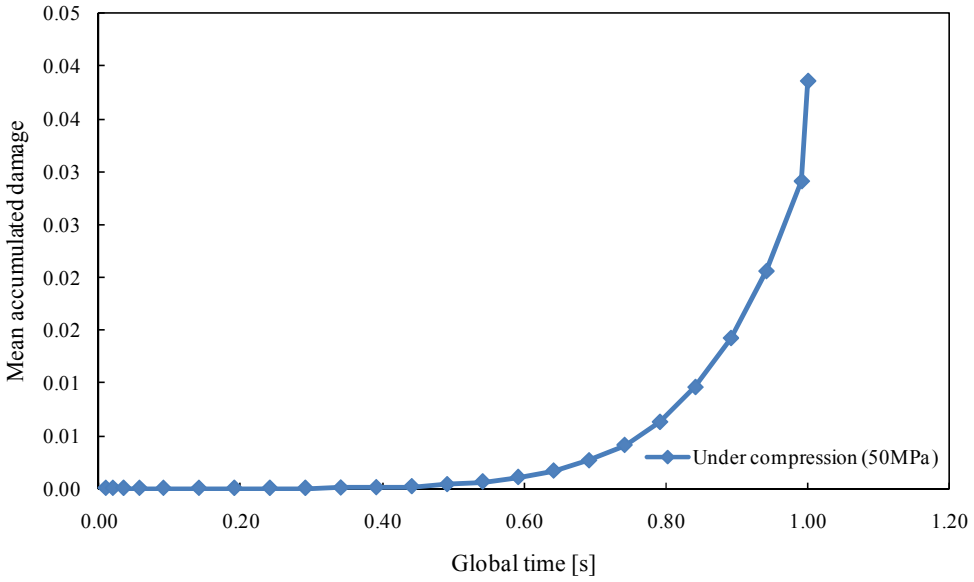

A.19 Pure brittle damage condition for RVE with PS=2.67 mm (50% porosity)

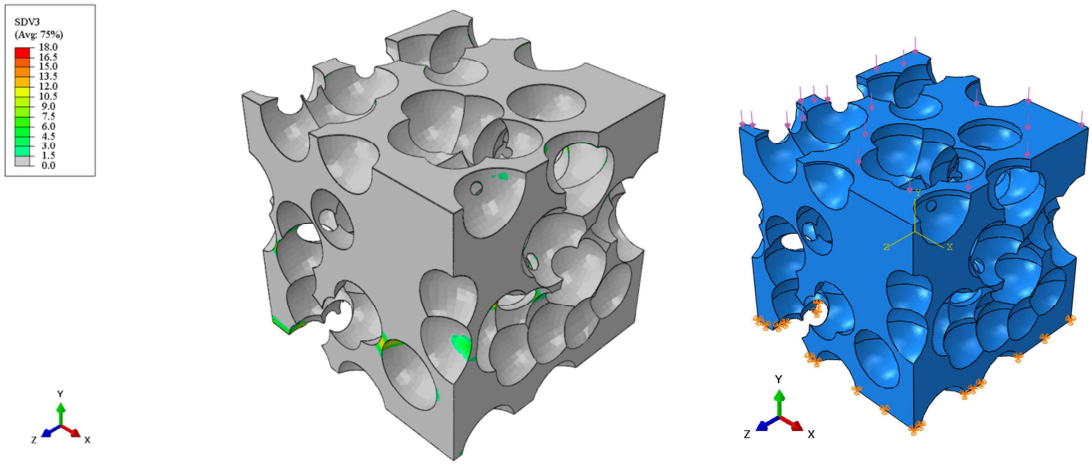

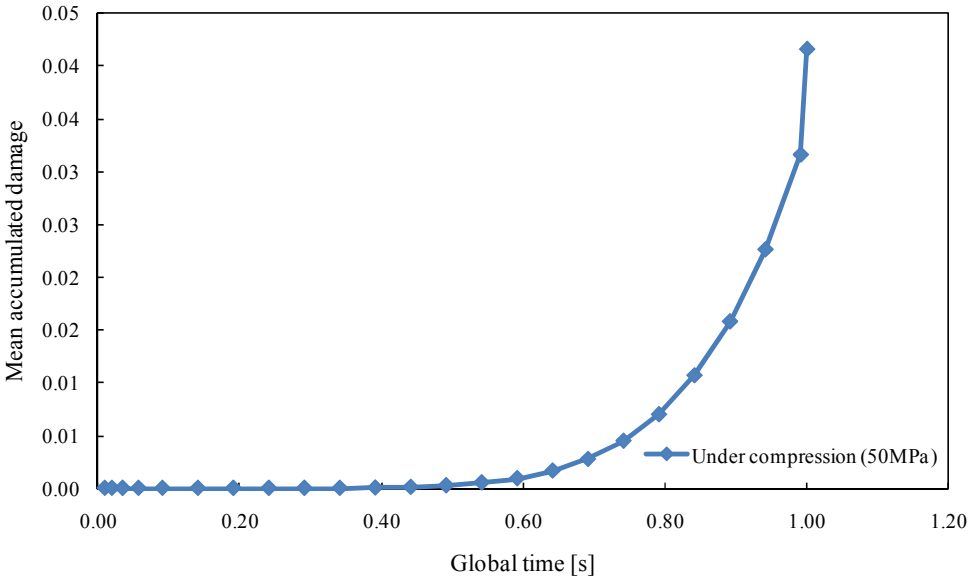

A.20 Pure brittle damage condition for RVE with PS=1.70 mm (70% porosity)

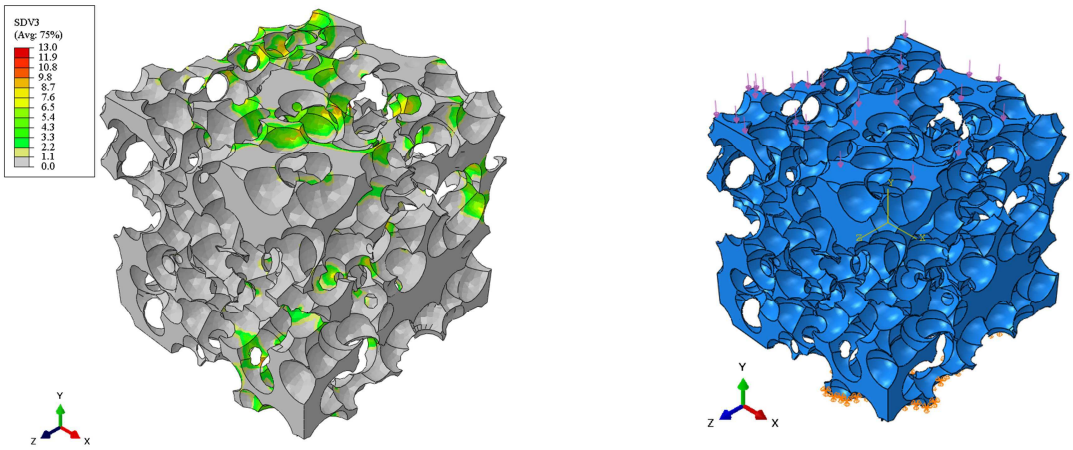

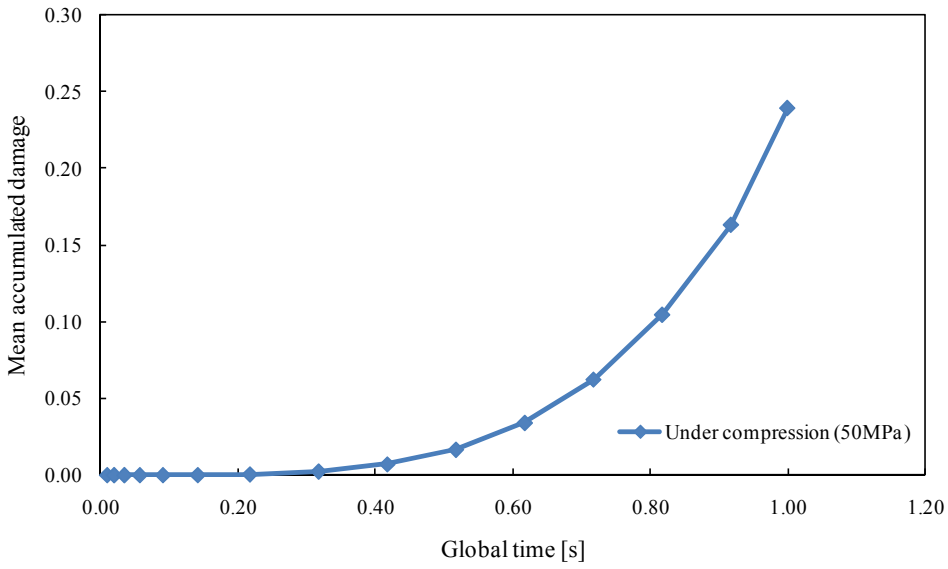

A.21 Pure brittle damage condition for RVE with PS=2.12 mm (70% porosity)

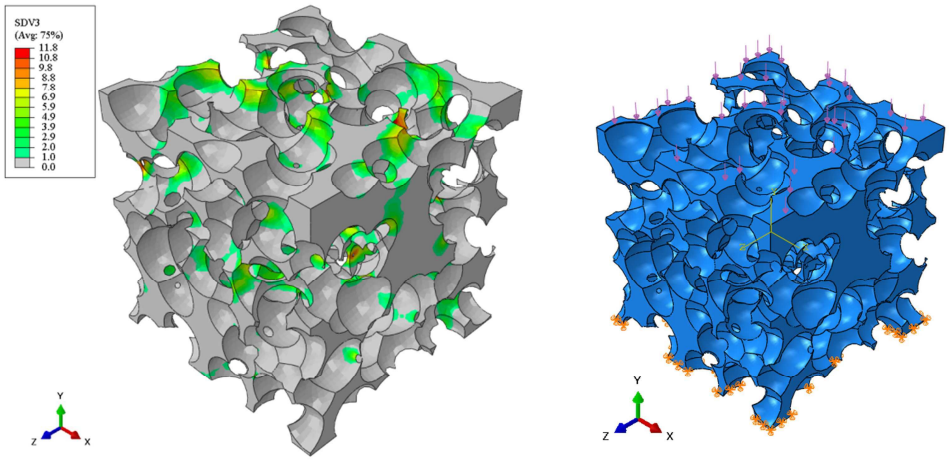

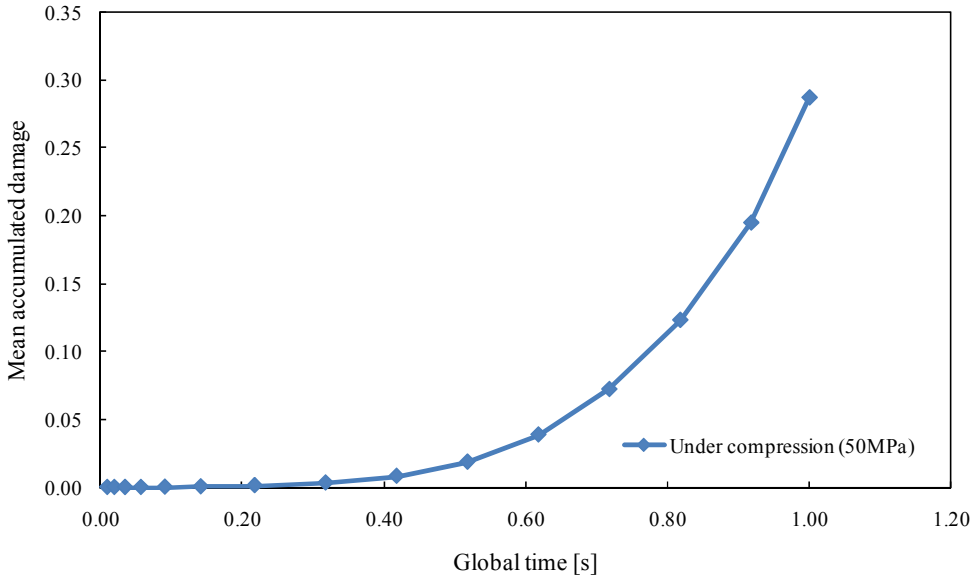

A.22 Pure brittle damage condition for RVE with PS=2.67 mm (70% porosity)

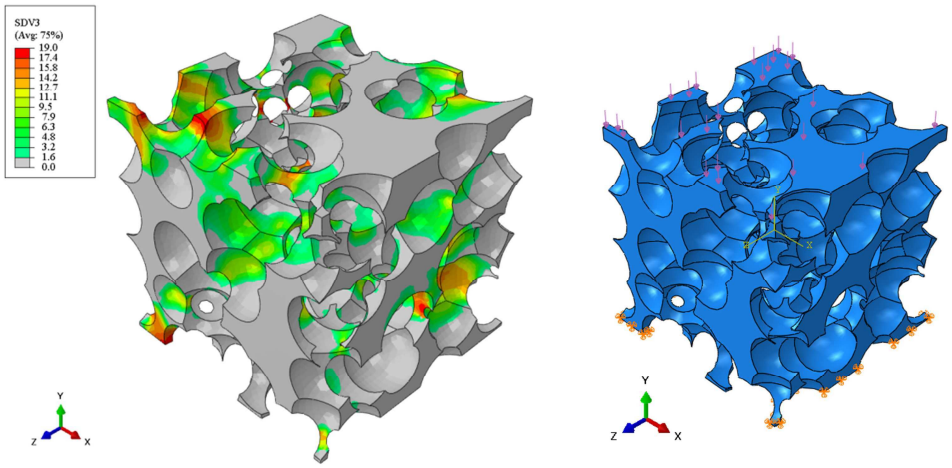

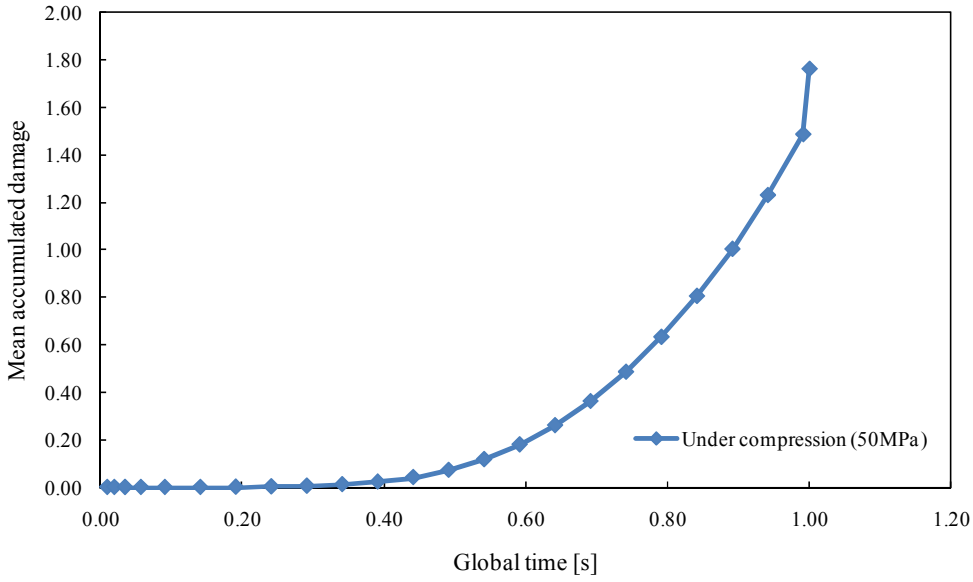

A.23 Pure brittle damage condition for RVE with 2D orientation along loading direction (50% porosity)

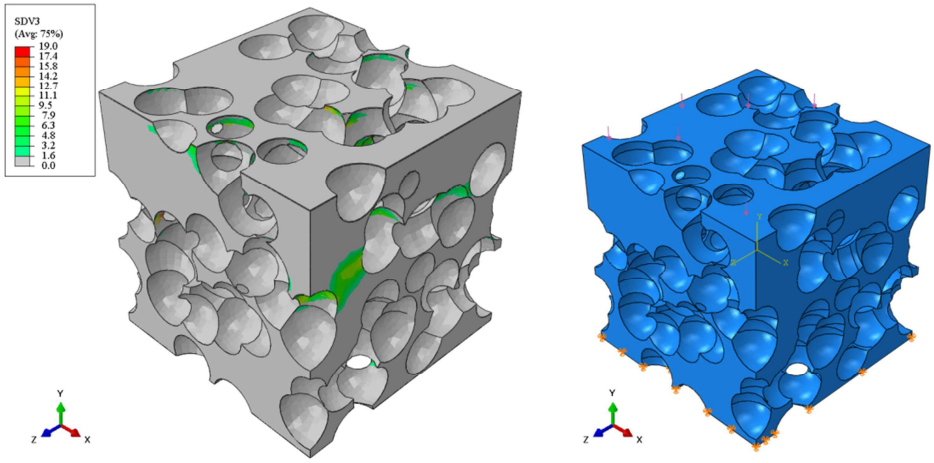

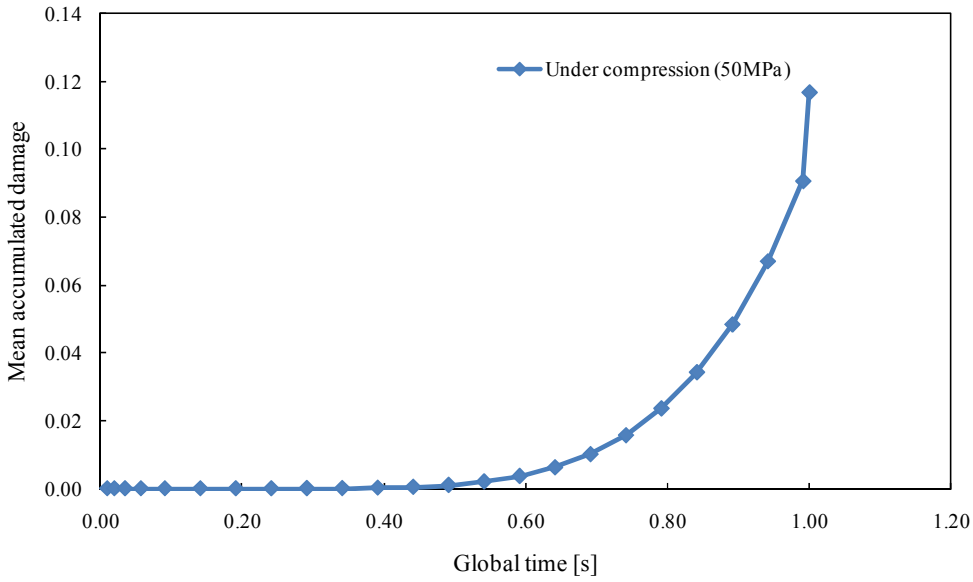

A.24 Pure brittle damage condition for RVE with 2D orientation perpendicular to loading direction (50% porosity)

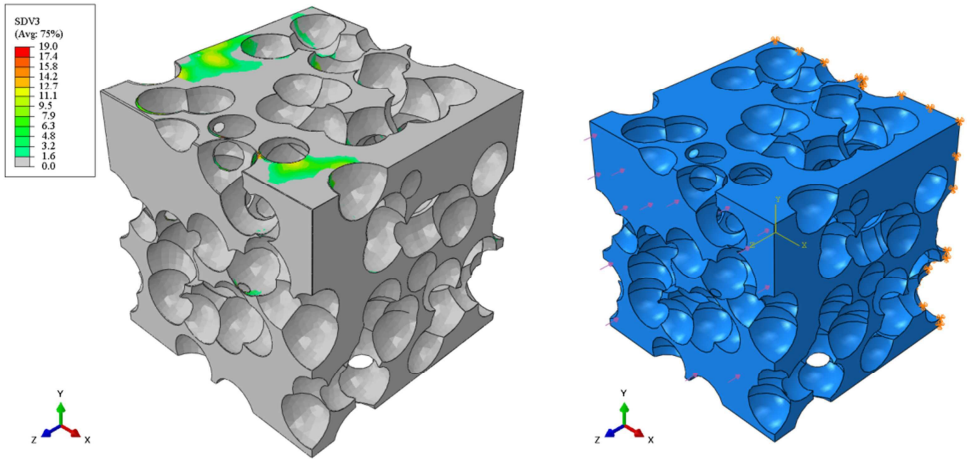

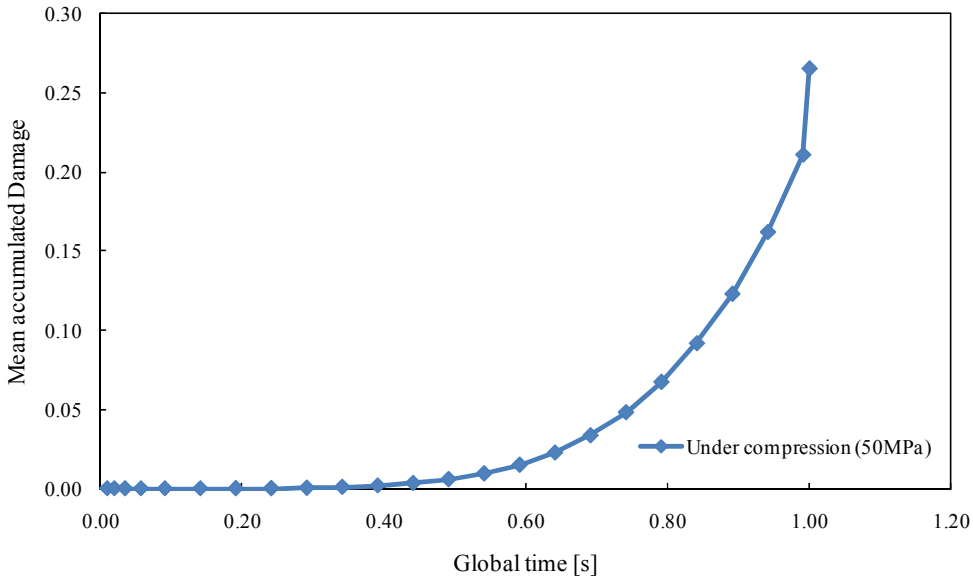

A.25 Pure brittle damage condition for RVE with fixed orientation along with loading direction (50% porosity)

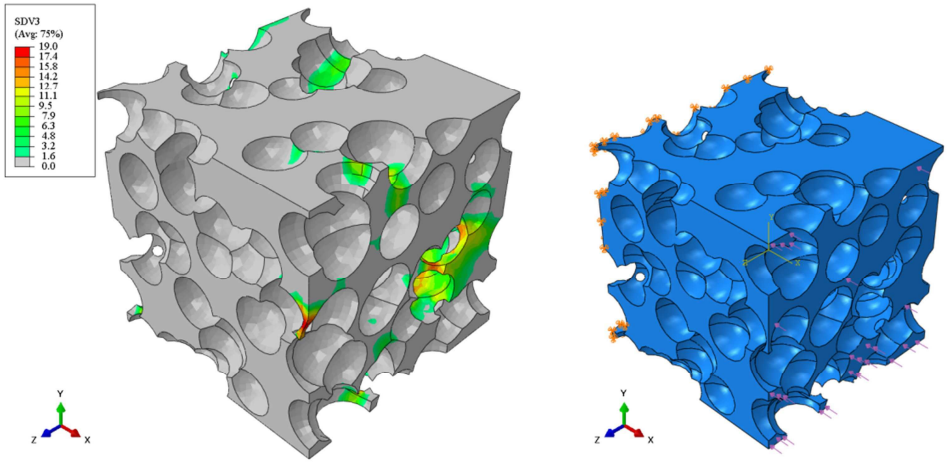

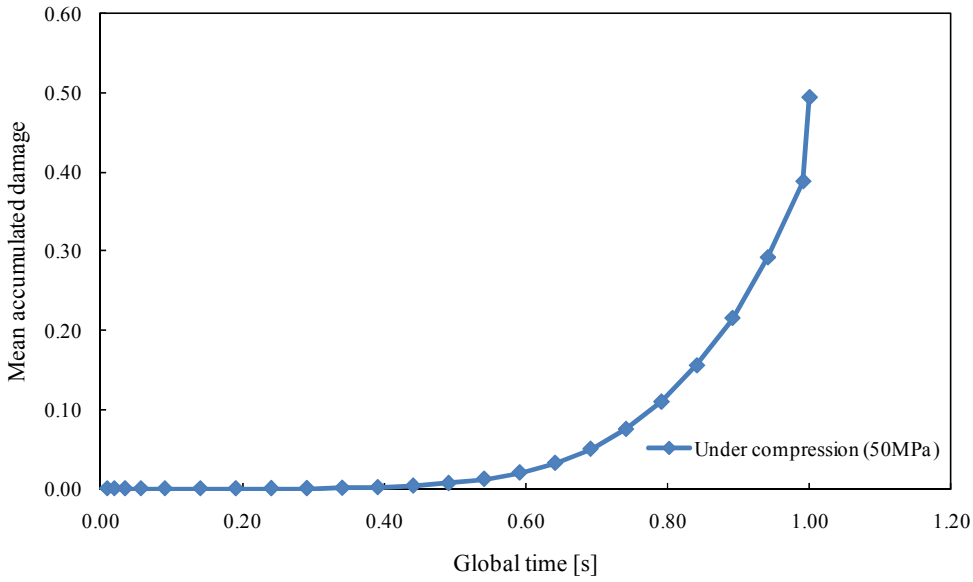

A.26 Pure brittle damage condition for RVE with fixed orientation perpendicular to loading direction (50% porosity)

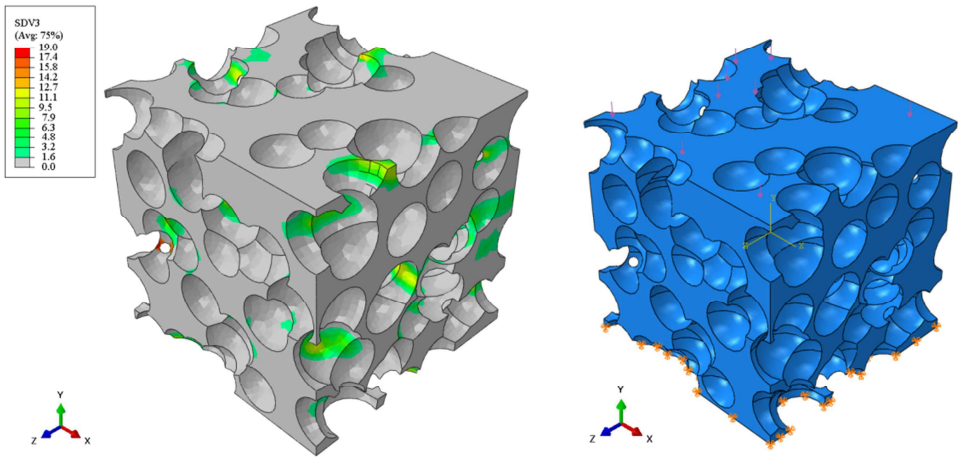

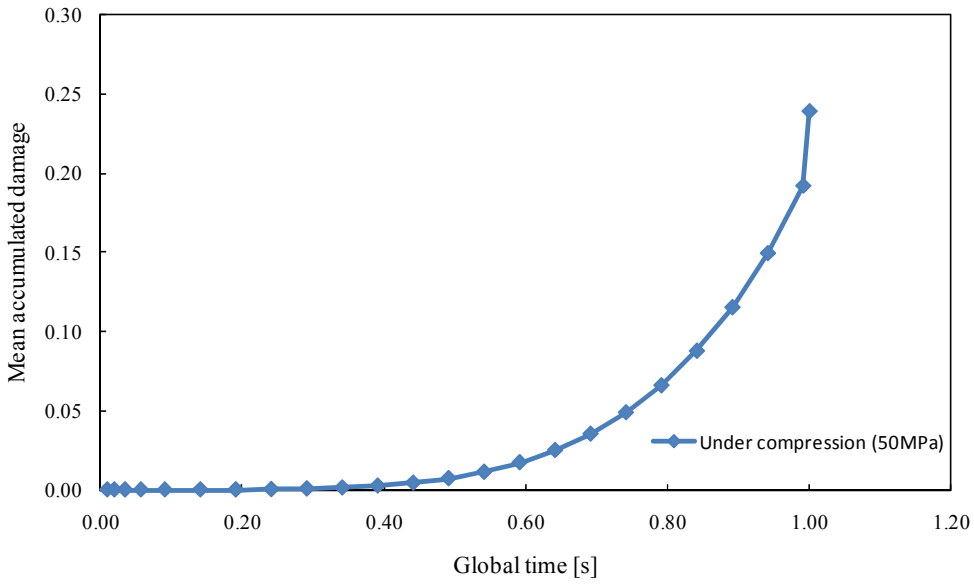

A.27 Pure brittle damage condition for RVE with 2D orientation along loading direction (70% porosity)

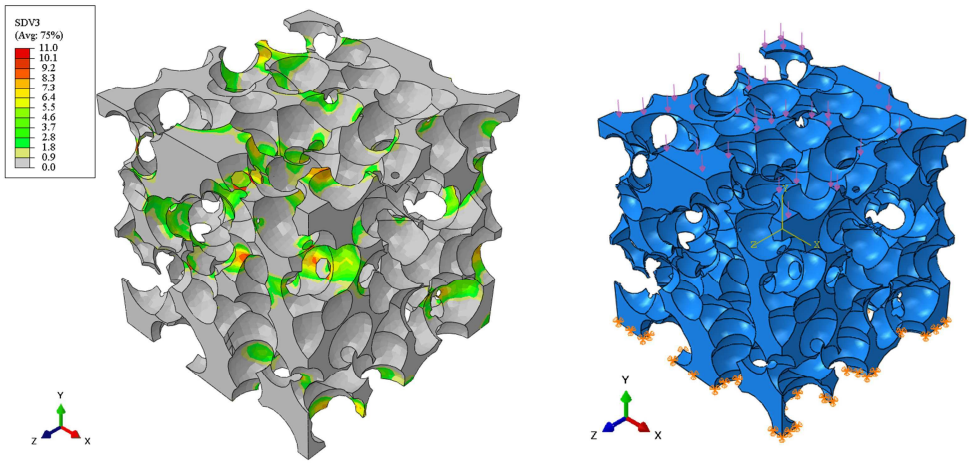

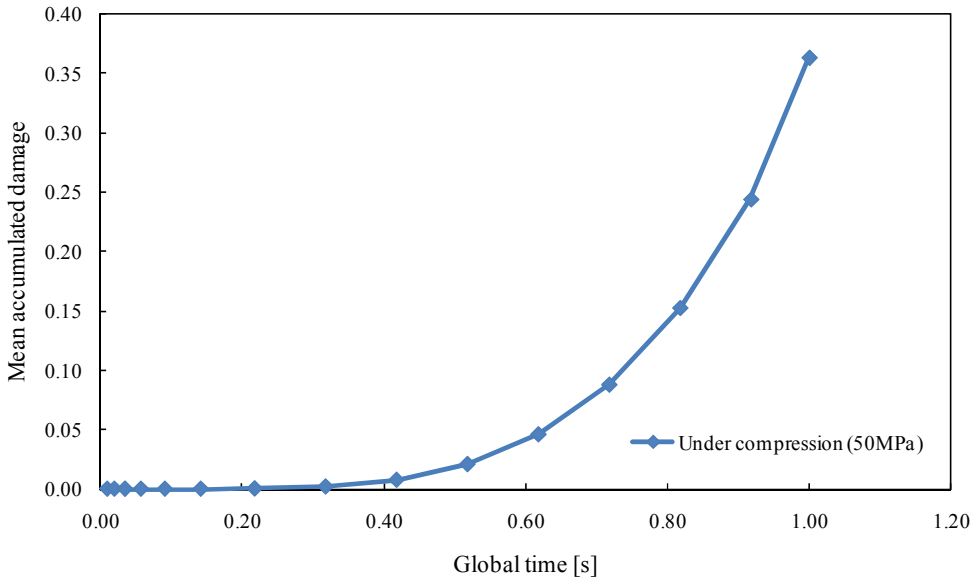

A.28 Pure brittle damage condition for RVE with 2D orientation perpendicular to loading direction (70% porosity)

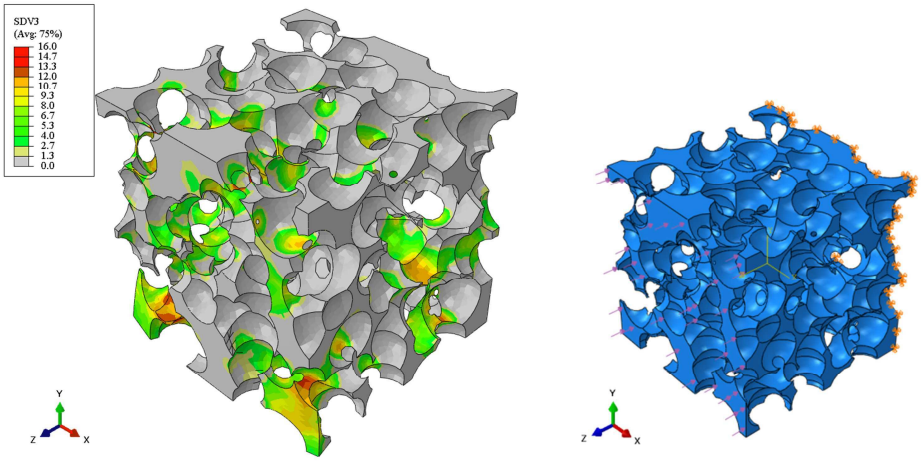

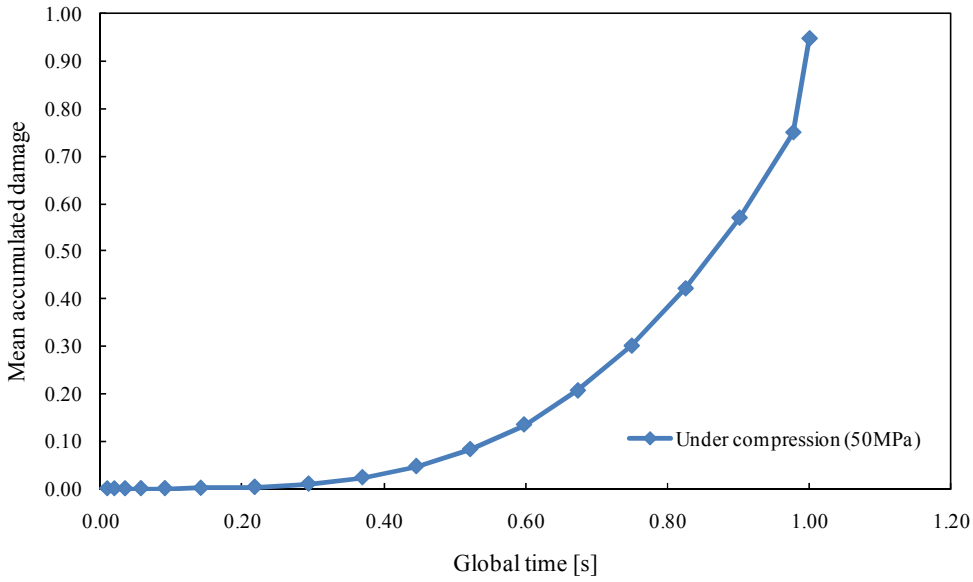

A.29 Pure brittle damage condition for RVE with fixed orientation along with loading direction (70% porosity)

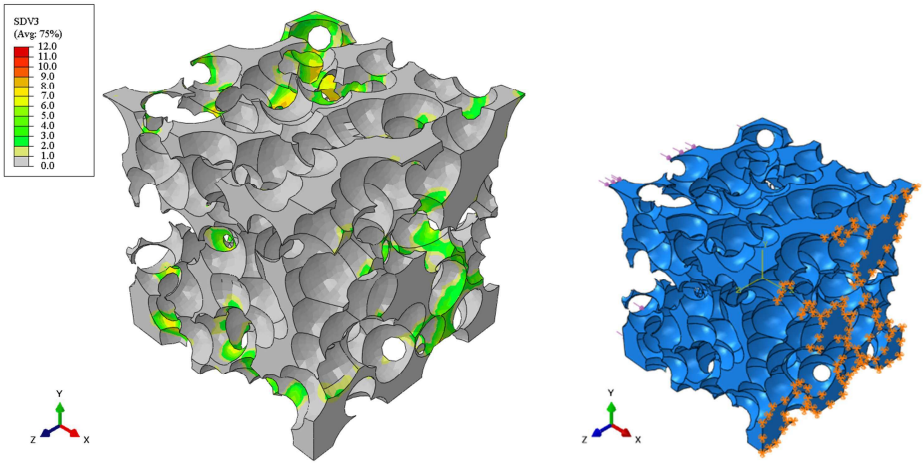

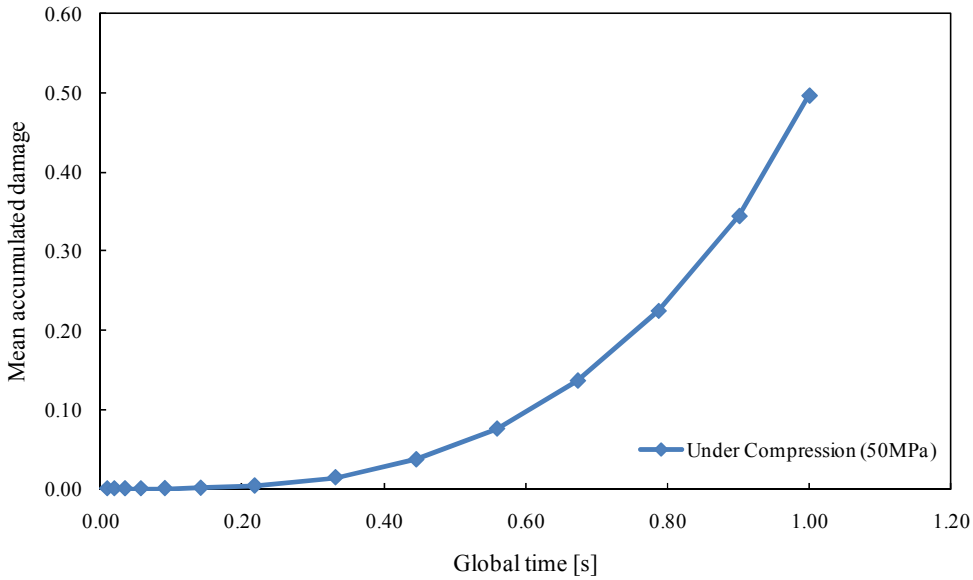

A.30 Pure brittle damage condition for RVE with fixed orientation perpendicular to loading direction (70% porosity)

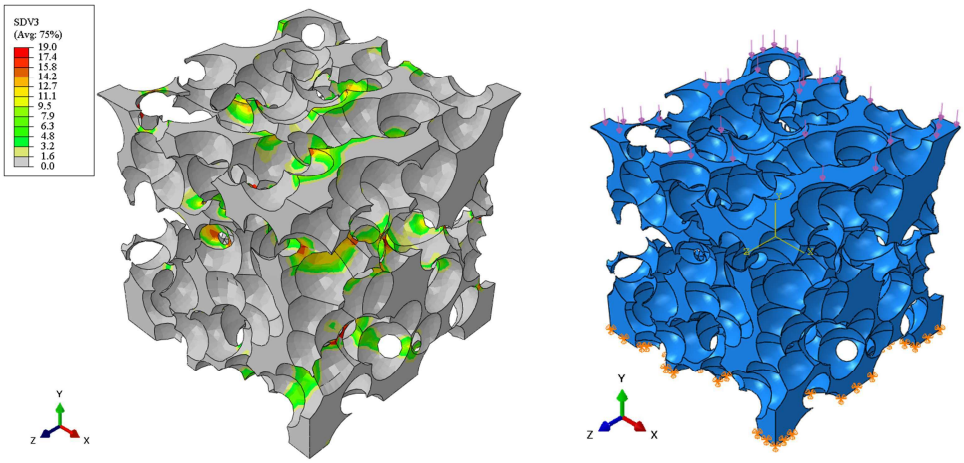

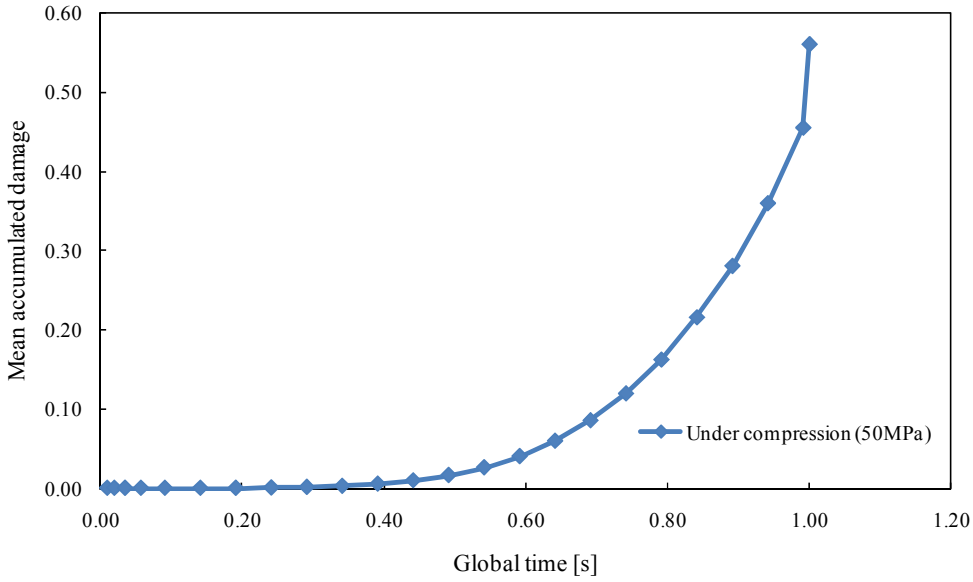

A.31 Pure brittle damage condition for RVE with PS=1.70 mm (60% porosity)

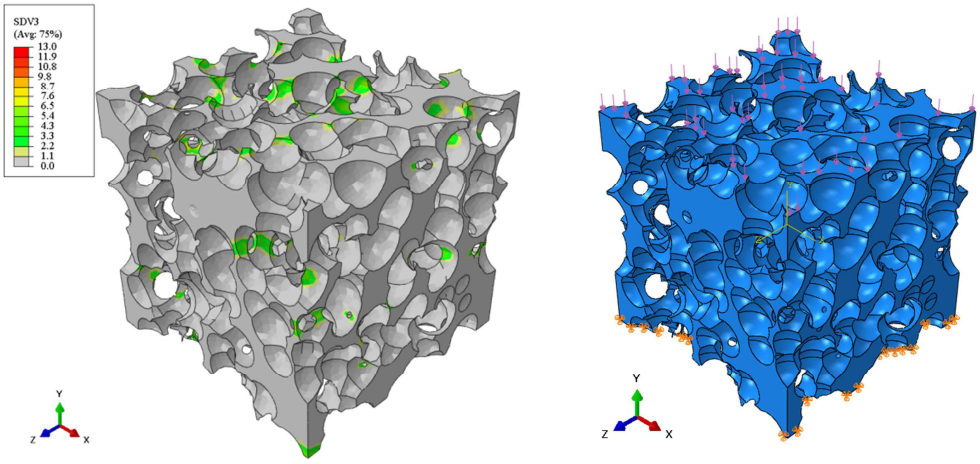

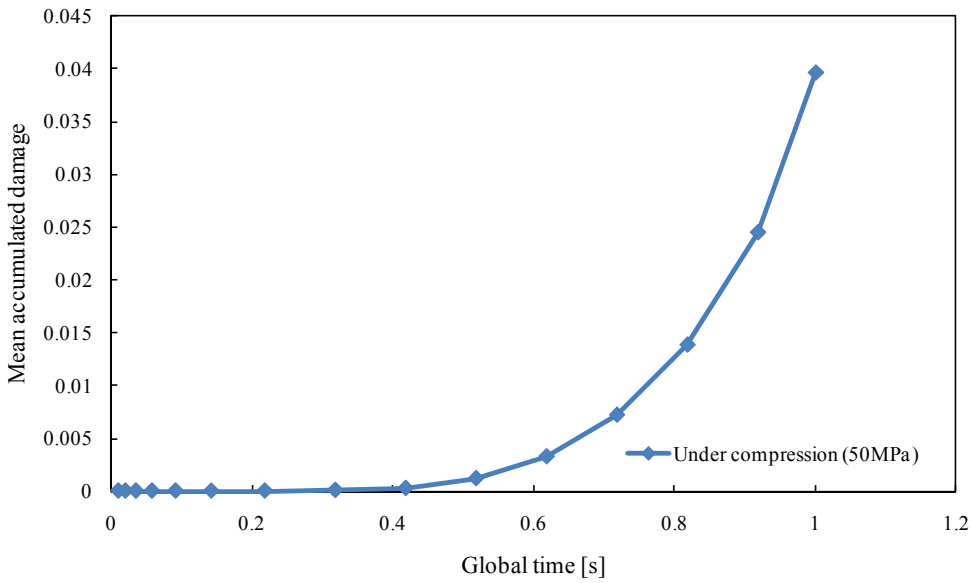

Bibliography

[1] J. Zeldovich, *The Oxidation of Nitrogen in Combustions and Explosions*, Acta Physicochimino USSR, **21 (4)**, (1946).

[2] G. Maier, *Gemischaufbereitung bei der mageren Vormischverbrennung in Gasturbinen: Entwicklungspotential und Grenzen*, Logos Verlag, Berlin, (2000).

[3] J. Meisl, *Minderung der Stickoxidemissionen durch Fett-Mager-Verbrennung unter Gasturbinenbedingungen*, Karlsruhe Universität, Karlsruhe, (1997).

[4] K. U. Schildmacher, A. Hoffmann, L. Selle, R. Koch, C. Schulz, H. J. Bauer, T. Poinsot, W. Krebs and B. Prade, *Unsteady Flame and Flow Field Interaction of a Premixed Model Gas Turbine Burner*, Proceedings of the Combustion Institute, **31**, (2007).

[5] K. Kuo, *Principles of Combustion*, Wiley-Interscience Publication, John Wiley & Sons Inc., (1986).

[6] F. Williams, *Combustion Theory*, Addison Wesley Publishing Company, (1985).

[7] P. Berenbrink and S. Hoffmann, *Suppression of Dynamic Combustion Instabilities by Passive and Active Means*, ASME Turbo Expo, Munich, (2000).

[8] G. J. M. Sims, R. W. Copplestone and J. R. Tilston, *Performance Studies of Passive Damping Techniques Used to Suppress Combustion Oscillations in LPP Combustor*, ASME Turbo Expo, 159-166, (2003).

[9] H. Krämer, F. Dinkelacker, A. Leipertz, G. Poeschel, M. Huth and M. Lenze, *Optimization of the Mixing Quality of a Real Size Gas Turbine Burner with Instantaneous Planar Laser-Induced Fluorescence Imaging*, ASME-Paper, **135**, (1999).

[10] B. T. Zinn, T. Lieuwen and Y. Neumeier, *Combustion Instabilities in Low NO_x Gas Turbines and their Active Control*, Gas Turbine Engine Combustion Symposium, 1998.

[11] H. Büchner, W. Leuckel and A. Hilgenstock, *Experimentelle und theoretische Untersuchungen der Entstehungsmechanismen thermoakustischer Druckschwingungen in einem industriellen Vormischbrenner*, VDI-Berichte, **1193**, 243-250, (1995).

[12] J. Göring, S. Hackemann and B. Kanka, *WHIPOX®: Ein faserverstärkter oxidkeramischer Werkstoff für Hochtemperatur- Langzeitanwendungen*, Materialwissenschaft und Werkstofftechnik, **38**, 766-772, (2007).

[13] M. Schmücker, A. Grafmüller and H. Schneider, *Mesostructure of WHIPOX All Oxide CMCs*, Composites Part A - Applied Science and Manufacturing, **34**, 613-622, (2003).

[14] F. Giese, H. C. Ries and C. Eigenbrod, *On the Performance of Porous Sound Absorbent Material in High Temperature Applications*, Journal of Engineering for Gas Turbines and Power, **132**, 121301.1-121301.6, (2010).

[15] M. Biot, *General Theory of Three Dimensional Consolidation*, J. App. Phys, **12**, 155-164, (1941).

[16] M. A. Biot, *Theory of Propagation of Elastic Waves in a Fluid-Saturated Porous Solid 2: Higher Frequency Range*, Journal of the Acoustical Society of America, **28**, 179-191, (1956).

[17] M. A. Biot, *Theory of Elasticity and Consolidation for a Porous Anisotropic Solid*, Journal of Applied Physics, **26**, 182-185, (2009).

[18] M. A. Biot, *Theory of Deformation of a Porous Viscoelastic Anisotropic Solid*, Journal of Applied Physics, **27**, 459-467, (2009).

[19] L. A. Taber, *A Theory for Transverse Deflection of Poroelastic Plates*, Journal of Applied Mechanics, **59**, 628-628, (1992).

[20] D. Theodorakopoulos and D. Beskos, *Flexural Vibration of Poroelastic Plates*, Acta Mechanica, **103**, 191-203, (1994).

[21] G. Cederbaum, L. P. Li and K. Schulgasser, *Poroelastic Structures*, Elsevier Science Ltd, (2000).

[22] L. Nagler and M. Schanz, *An Extendable Poroelastic Plate Formulation in Dynamics*, Archive of Applied Mechanics, **80**, 1177-1195, (2010).

[23] R. D. Mindlin and J. Yang, *An Introduction to the Mathematical Theory of Vibrations of Elastic Plates*, World Scientific Pub Co Inc., (2006).

[24] G. Preußer, *Eine systematische Herleitung verbesserter Plattengleichungen*, Archive of Applied Mechanics (Ingenieur Archiv), **54**, 51-61, (1984).

[25] R. Kienzler, *On Consistent Plate Theories*, Archive of Applied Mechanics, **72**, 229-247, (2002).

[26] R. Kienzler and H. Altenbach, *On Consistent Second-Order Plate Theories*, in: R. Kienzler, H. Altenbach, I. Ott (Eds.), Theories of Plates and Shells: Critical Review and New Applications, Springer, 2004, pp. 85-85.

[27] W. Ehlers, *Poröse Medien, Ein kontinuumsmechanisches Modell auf der Basis der Mischungstheorie*, Universität-GH-Essen, (1989).

[28] R. de Boer and S. J. Kowalski, *Thermodynamics of Fluid-Saturated Porous Media with a Phase Change*, Acta Mechanica, **109**, 167-189, (1995).

[29] S. Diebels, H. Steeb and W. Ehlers, *Microscopic and Macroscopic Modelling of Foams*, PAMM, **2**, 156-157, (2003).

[30] W. Ehlers, *Foundations of Multiphasic and Porous Materials*, in: W. Ehlers, Bluhm, J (Ed.), Porous Media: Theory, Experiments and Numerical Applications, Springer-Verlag, Berlin, 2002, pp. 3-86.

[31] C. Wieners, M. Ammann, S. Diebels and W. Ehlers, *Parallel 3-d Simulations for Porous Media Models in Soil Mechanics*, Computational Mechanics, **19**, 75-87, (2002).

[32] X. Chateau and L. Dormieux, *Micromechanics of Unsaturated Porous Media*, IUTAM Symposium on Theoretical and Numerical Merhods in Continuum Mechanics of Porous Materials, Stuttganrt, 125-130, (2001).

[33] R. de Boer, Ehlers, W., *Theorie der Mehrkomponentenkontinua mit Anwendung auf bodenmechanische Probleme*, Forschungsberichte aus dem Fachbereich Bauwesen, Universität Essen, 1986.

[34] D. S. Drumheller, *The Theoretical Treatment of a Porous Solid Using a Mixture Theory*, International Journal of Solids Structures, **14**, 441-456, (1978).

[35] R. M. Bowen, *Incompressible Porous Media Models by Use of the Theory of Mixtures*, International Journal of Engineering Science, **18**, 1129-1148, (1980).

[36] R. M. Bowen, *Compressible Porous Media Models by Use of the Theory of Mixtures*, International Journal of Engineering Science, **20**, 697-735, (1982).

[37] V. Mow, S. Kuei, W. Lai and C. Armstrong, *Biphasic Creep and Stress Relaxation of Articular Cartilage in Compression: Theory and Experiments*, ASME Journal of Biomechanical Engineering, **102**, 73-84, (1980).

[38] A. Droste, *Beschreibung und Anwendung eines elastisch-plastischen Materialmodells mit Schädigung für hochporöse Metallschäume*, Dissertation, Stuttgart, Stuttgart University, (2002).

[39] W. Ehlers and J. Kubik, *On Finite Dynamic Equations for Fluid-Saturated Porous Media*, Acta Mechanica, **105**, 101-117, (1994).

[40] D. Gawin and B. A. Schrefler, *Thermo-hydro-mechanical Analysis of Partially Saturated Porous Materials*, Geomechanics Abstracts, **1**, (1997).

[41] W. Ehlers and O. Klar, *On the Identification of the Parameters of a Viscoelastic Material Law for Polymeric Foams*, PAMM, **2**, 280-281, (2003).

[42] S. R. Ghadiani, *A Multiphasic Continuum Mechanical Model for Design Investigations of an Effusion-Cooled Rocket Thrust Chamber*, Dissertation, Stuttgart University, (2005).

[43] F. Vales, R. Rezakhanlou and C. Olagnon, *Determination of the Fracture Mechanical Parameters of Porous Ceramics from Microstructure Parameters Measured by Quantitative Image Analysis*, Journal of Materials Science, **34**, 4081-4088, (1999).

[44] C. G. Sammis and M. F. Ashby, *The Failure of Brittle Porous Solids under Compressive Stress States*, Acta Metallurgica, **34**, 511-526, (1986).

[45] J. B. Wachtman, W. R. Cannon and M. J. Matthewson, *Mechanical Properties of Ceramics*, John Wiley & Sons Inc, (2009).

[46] T. Sadowski and S. Samborski, *Prediction of the Mechanical Behaviour of Porous Ceramics Using Mesomechanical Modelling*, Computational Materials Science, **28**, 512-517, (2003).

[47] D. Hardy and D. J. Green, *Mechanical Properties of a Partially Sintered Alumina*, Journal of the European Ceramic Society, **15**, 769-775, (1995).

[48] T. Sadowski, *Thermodynamic Approach to Constitutive Modelling of Semi-Brittle Ceramics*, Computational Mechanics, **20**, 150-155, (1997).

[49] T. Sadowski, S. Hardy and E. Postek, *A New Model for the Time-dependent Behavior of Polycristalline Ceramic Materials with Metallic Inter-granular Layers under Tension*, Materials Science and Engineering A, **424**, 230-238, (2006).

[50] T. Sadowski and L. Marsavina, *Multiscale Modelling of Damage Processes in Polycrystalline Ceramic Porous Composites*, Key Engineering Materials, **399**, 79-88, (2009).

[51] T. Sadowski and L. Marsavina, *Multiscale Modelling of Gradual Degradation in Al2O3/ZrO2 Ceramic Composites under Tension*, Material Science Forum, **638**, 2743-2748, (2010).

[52] T. Sadowski and S. Samborski, *Modeling of Ceramics Response to Compressive Loading*, Journal of American Ceramic Society, **86**, 2218-21, (2003).

[53] T. Sadowski and S. Samborski, *An Influence of Initial Porosity on Damage Process in Semi-brittle Polycrystalline Ceramics under Compression*, in: W. Ehlers (Ed.), IUTAM Symposium ob the Theoretical and Numerical Methods in Continuum Mechanics of Porous Materials, Stuttgart, 2002, pp. 313-318.

[54] T. Sadowski and S. Samborski, *Modeling of porous ceramics response to compressive loading*, Journal of the American Ceramic Society, **86**, 2218-2221, (2003).

[55] T. Sadowski and S. Samborski, *Development of Damage State in Porous Ceramics under Compression*, Computational Materials Science, **43**, 75-81, (2008).

[56] S. Samborski and T. Sadowski, *On the Method of Damage Assessment in Porous Ceramics*, In: 11th International Conference on Fracture, Turin, 2005.

[57] I. C. Van den Born, A. Santen, H. D. Hoekstra and J. T. M. De Hosson, *Mechanical Strength of Highly Porous Ceramics*, Physical Review B, **43**, 3794-3796, (1991).

[58] G. D. Quinn, *Weibull Strength Scaling for Standardized Rectangular Flexure Specimens*, Journal of the American Ceramic Society, **86**, 508-510, (2003).

[59] G. D. Quinn, *Weibull Effective Volumes and Surfaces for Cylindrical Rods Loaded in Flexure*, Journal of the American Ceramic Society, **86**, 475-479, (2003).

[60] R. Danzer, P. Supancic, J. Pascual and T. Lube, *Fracture Statistics of Ceramics-Weibull Statistics and Deviations from Weibull Statistics*, Engineering Fracture Mechanics, **74**, 2919-2932, (2007).

[61] K. K. Phani, *A New Modified Weibull Distribution Function for the Evaluation of the Strength of Silicon Carbide and Alumina Fibres*, Journal of Materials Science, **23**, 2424-2428, (1988).

[62] R. H. Doremus, *Fracture Statistics: A Comparison of the Normal, Weibull, and Type I Extreme Value Distributions*, Journal of Applied Physics, **54**, 193-198, (1983).

[63] B. Bergman, *On the Estimation of the Weibull Modulus*, Journal of Materials Science Letters, **3**, 689-692, (1984).

[64] J. D. Sullivan and P. H. Lauzon, *Experimental Probability Estimators for Weibull Plots*, Journal of Materials Science Letters, **5**, 1245-1247, (1986).

[65] F. P. Knudsen, *Dependence of Mechanical Strength of Brittle Polycrystalline Specimens on Porosity and Grain Size*, Journal of the American Ceramic Society, **42**, 376-387, (1959).

[66] S. Ji, Q. Gu and B. Xia, *Porosity Dependence of Mechanical Properties of Solid Materials*, Journal of Materials Science, **41**, 1757-1768, (2006).

[67] A. R. Boccaccini, *Influence of Stress Concentrations on the Mechanical Property–Porosity Correlation in Porous Materials*, Journal of Materials Science Letters, **17**, 1273-1275, (1998).

[68] R. W. Rice, *Comparison of Stress Concentration Versus Minimum Solid Area Based Mechanical Property-Porosity Relations*, Journal of Materials Science, **28**, 2187-2190, (1993).

[69] A. R. Boccaccini and Z. Fan, *A New Approach for the Young's Modulus-Porosity Correlation of Ceramic Materials*, Ceramics International, **23**, 239-245, (1997).

[70] R. C. Rossi, *Prediction of the elastic moduli of composites*, Journal of the American Ceramic Society, **51**, 433-440, (1968).

[71] R. W. Rice, *Comparison of Physical Property-Porosity Behaviour with Minimum Solid Area Models*, Journal of Material Science, **31**, 1509-1528, (1996).

[72] L. J. Gibson and M. F. Ashby, *Cellular Solids: Structure and Properties*, Cambridge University Press, (1999).

[73] K. K. Phani, *Young's Modulus-Porosity Relation in Gypsum Systems*, American Ceramic Society Bulletin, **65**, 1584-1586, (1986).

[74] A. P. Roberts and E. J. Garboczi, *Elastic Properties of Model Porous Ceramics*, Journal of the American Ceramic Society, (2000).

[75] E. J. Garboczi and A. R. Day, *An Algorithm for Computing the Effective Linear Elastic Properties of Heterogeneous Materials: Three-Dimensional Results for Composites with Equal Phase Poisson Ratios*, Journal of the Mechanics and Physics of Solids, **43**, 1349-1362, (1995).

[76] J. Poutet, D. Manzoni, F. Hage-Chehade, J. F. Thovert and P. M. Adler, *The Effective Mechanical Properties of Random Porous Media*, Journal of the Mechanics and Physics of Solids, **44**, 1587-1620, (1996).

[77] I. Doghri and L. Tinel, *Micromechanics of Inelastic Composites with Misaligned Inclusions: Numerical Treatment of Orientation*, Computer Methods in Applied Mechanics and Engineering, **195**, 1387-1406, (2006).

[78] D. F. Adams, *Inelastic Analysis of a Unidirectional Composite Subjected to Transverse Normal Loading*, Journal of Composite Materials, **4**, 310-310, (1970).

[79] D. Saraev and S. Schmauder, *Finite Element Modelling of Al/SiCp Metal Matrix Composites with Particles Aligned in Stripes– a 2D-3D Comparison*, International Journal of Plasticity, **19**, 733-747, (2003).

[80] H. J. Böhm and W. Han, *Comparisons Between Three-Dimensional and Two-Dimensional Multi-Particle Unit Cell Models for Particle Reinforced Metal Matrix Composites*, Modelling and Simulation in Materials Science and Engineering, **9**, 47-47, (2001).

[81] J. Aboudi, M. J. Pindera and S. M. Arnold, *Higher-Order Theory for Periodic Multiphase Materials with Inelastic Phases*, International Journal of Plasticity, **19**, 805-847, (2003).

[82] R. M. Haj-Ali and A. H. Muliana, *A Multi-Scale Constitutive Formulation for the Nonlinear Viscoelastic Analysis of Laminated Composite Materials and Structures*, International Journal of Solids and Structures, **41**, 3461-3490, (2004).

[83] G. J. Dvorak, *Transformation Field Analysis of Inelastic Composite Materials*, Proceedings of the Royal Society of London. Series A: Mathematical and Physical Sciences, **437**, 311-327, (1992).

[84] S. Jansson, *Homogenized Nonlinear Constitutive Properties and Local Stress Concentrations for Composites with Periodic Internal Structure*, International Journal of Solids and Structures, **29**, 2181-2200, (1992).

[85] F. Lene, *Damage Constitutive Relations for Composite Materials*, Engineering Fracture Mechanics, **25**, 713-728, (1986).

[86] C. González and J. Llorca, *A Self-Consistent Approach to the Elasto-Plastic Behaviour of Two-Phase Materials Including Damage*, Journal of the Mechanics and Physics of Solids, **48**, 675-692, (2000).

[87] F. Castagna, S. Giammartini, C. Mongiello, M. Presaghi and G. Puglisi, *Numerical Investigation Aimed at Parametrical Validation of Combustion Phenomena in Small Size Premixed Burners*, 29th Meeting on Combustion, Pisa, Italy, (2006).

[88] H. E. Pettermann, A. F. Plankensteiner, H. J. Böhm and F. G. Rammerstorfer, *A Thermo-Elasto-Plastic Constitutive Law for Inhomogeneous Materials Based on an Incremental Mori-Tanaka Approach*, Computers and Structures, **71**, 197-214, (1999).

[89] P. Ponte Castaneda and P. Suquet, *Nonlinear Composites and Microstructure Evolution*, Mechanics for a New Mellennium, 253-274, (2002).

[90] O. Pierard and I. Doghri, *An Enhanced Affine Formulation and the Corresponding Numerical Algorithms for the Mean-Field Homogenization of Elasto-Viscoplastic Composites*, International Journal of Plasticity, **22**, 131-157, (2006).

[91] I. Doghri, L. Adam and N. Bilger, *Mean-Field Homogenization of Elasto-Viscoplastic Composites Based on a General Incrementally Affine Linearization Method*, International Journal of Plasticity, (2009).

[92] J. D. Eshelby, *The Determination of the Elastic Field of an Ellipsoidal Inclusion, and Related Problems*, Proceedings of the Royal Society of London. Series A, Mathematical and Physical Sciences, **241**, 376-396, (1957).

[93] E. O. Hall, *The Deformation and Ageing of Mild Steel: III Discussion of Results*, Proceedings of the Physical Society. Section B, **64**, 747-747, (1951).

[94] N. J. Petch, *The Orientation Relationships Between Cementite and Iron*, Acta Crystallographica, **6**, 96-96, (1953).

[95] O. Pierard, C. Friebel and I. Doghri, *Mean-field Homogenization of Multi-Phase Thermo-Elastic Composites: A General Framework and its Validation*, Composites Science and Technology, **64**, 1587-1603, (2004).

[96] T. Mori and K. Tanaka, *Average Stress in Matrix and Average Elastic Energy of Materials with Misfitting Inclusions*, Acta Metallurgica, **21**, 571-574, (1973).

[97] C. Friebel, I. Doghri and V. Legat, *General Mean-Field Homogenization Schemes for Viscoelastic Composites Containing Multiple Phases of Coated Inclusions*, International Journal of Solids and Structures, **43**, 2513-2541, (2006).

[98] I. Doghri and L. Tinel, *Micromechanical Modeling and Computation of Elasto-Plastic Materials Reinforced with Distributed-Orientation Fibers*, International Journal of Plasticity, **21**, 1919-1940, (2005).

[99] O. Pierard, J. Llorca, J. Segurado and I. Doghri, *Micromechanics of Particle-Reinforced Elasto-Viscoplastic Composites: Finite Element Simulations Versus Affine Homogenization*, International Journal of Plasticity, **23**, 1041-1060, (2007).

[100] M. Boussuge, *Some Numerical Approaches of Creep, Thermal Shock, Damage and Delayed Failure of Ceramics and Refractories*, Bulletin of Material Science, **24**, 97-100, (2001).

[101] G. Schoeck, *Thermally Activated Crack-Propagation in Brittle Materials*, International Journal of Fracture, **44**, 1-14, (1990).

[102] R. Danzer, *Ceramics: Mechanical Performance and Life Time Prediction*, in: D. Bloor, R. Brook, S. Mahajan, R. Cahn (Eds.), The Encyclopedia of Advanced Materials, Pergamon, 1994, pp. 385-398.

[103] A. M. Brown and M. F. Ashby, *On the Power-Law Creep Equation*, Scripta Metallurgica, **14**, 1297-1302, (1980).

[104] H. J. Frost and M. F. Ashby, *Deformation Mechanism Maps*, Pergamon Press, Oxford, (1982).

[105] H. Riedel, *Fracture at High Temperatures*, Springer, New York, (1987).

[106] T. Fett and D. Munz, *Versagen von Keramik im Hochtemperaturbereich*, Materialwissenschaft und Werkstofftechnik, **29**, 670-678, (1998).

[107] B. Schneider, A. Guette, R. Naslain, M. Cataldi and A. Costecalde, *A Theoretical and Experimental Approach to the Active-to-Passive Transition in the Oxidation of Silicon Carbide: Experiments at High Temperatures and Low Total Pressures*, Journal of Materials Science, **33**, 535-547, (1998).

[108] C. J. Gilbert, D. R. Bloyer, M. W. Barsoum, T. El-Raghy, A. P. Tomsia and R. O. Ritchie, *Fatigue-Crack Growth and Fracture Properties of Coarse and Fine-Grained Ti3SiC2*, Scripta Materialia, **42**, 761-767, (2000).

[109] G. Grathwohl and T. Liu, *Crack Resistance and Fatigue of Transforming Ceramics: II, CeO2-Stabilized Tetragonal ZrO2*, Journal of the American Ceramic Society, **74**, 3028-3034, (1991).

[110] G. Briche, N. Tessier-Doyen, M. Huger and T. Chotard, *Investigation of the Damage Behaviour of Refractory Model Materials at High Temperature by Combined Pulse Echography and Acoustic Emission Techniques*, Journal of the European Ceramic Society, **28**, 2835-2843, (2008).

[111] R. Danzer, T. Lube, P. Supancic and R. Damani, *Fracture of ceramics*, Advanced Engineering Materials, **10**, 275-298, (2008).

[112] M. Fellner and P. Supancic, *Thermal Shock Failure of Brittle Materials*, Key Engineering Materials, **223**, 97-106, (2002).

[113] R. Danzer and P. Supancic, *Thermal Shock Behavior of Batio3 PTC-Ceramics*, (2003).

[114] R. Danzer, *Mechanical Failure of Advanced Ceramics: the Value of Fractography*, Key Engineering Materials, **223**, 1-18, (2002).

[115] H. Chai and B. R. Lawn, *A Universal Relation for Edge Chipping from Sharp Contacts in Brittle Materials: A Simple Means of Toughness Evaluation*, Acta Materialia, **55**, 2555-2561, (2007).

[116] M. Lengauer and R. Danzer, *Silicon Nitride Tools for the Hot Rolling of High-Alloyed Steel and Superalloy Wires-Crack Growth and Lifetime Prediction*, Journal of the European Ceramic Society, **28**, 2289-2298, (2008).

[117] A. Börger, P. Supancic and R. Danzer, *The Ball on Three Balls Test for Strength Testing of Brittle Discs: Stress Distribution in the Disc*, Journal of the European Ceramic Society, **22**, 1425-1436, (2002).

[118] R. Morrell, *Edge Flaking-Similarity Between Quasistatic Indentation and Impact Mechanisms for Brittle Materials*, Key Engineering Materials, **290**, 14-22, (2005).

[119] R. Danzer, M. Hangl and R. Paar, *Edge Chipping of Brittle Materials*, Ceramic Transactions (USA), **122**, 43-55, (2000).

[120] E. A. Almond and N. J. McCormick, *Edge Flaking of Brittle Materials*, Journal of Hard Materials, **1**, 154-156, (1990).

[121] D. B. Marshall and B. R. Lawn, *An Indentation Technique for Measuring Stresses in Tempered Glass Surfaces*, Journal of the American Ceramic Society, **60**, 86-87, (1977).

[122] D. P. H. Hasselman, *Unified Theory of Thermal Shock Fracture Initiation and Crack Propagation in Brittle Ceramics*, Journal of the American Ceramic Society, **52**, 600-604, (1969).

[123] J. J. Mecholsky Jr and S. W. Freiman, *Relationship Between Fractal Geometry and Fractography*, Journal of the American Ceramic Society, **74**, 3136-3138, (1991).

[124] T. A. Michalske and S. W. Freiman, *A Molecular Interpretation of Stress Corrosion in Silica*, Nature, **295**, 511-512, (1982).

[125] A. B. Alles and V. L. Burdick, *Grain Boundary Oxidation in PTCR Barium Titanate Thermistors*, Journal of the American Ceramic Society, **76**, 401-408, (1993).

[126] S. M. Wiederhorn and L. H. Bolz, *Stress Corrosion and Static Fatigue of Glass*, Journal of the American Ceramic Society, **53**, 543-548, (1970).

[127] J. Lemaitre and R. Desmorat, *Engineering Damage Mechanics*, Springer-Verlag, Berlin, Heidelberg, (2005).

[128] L. Brassart, I. Doghri and L. Delannay, *Homogenization of Elasto-Plastic Composites Coupled with a Nonlinear Finite Element Analysis of the Equivalent Inclusion Problem*, International Journal of Solids and Structures, **47**, 716-729, (2010).

[129] L. Brassart, H. M. Inglis, L. Delannay, I. Doghri and P. H. Geubelle, *An Extended Mori-Tanaka Homogenization Scheme for Finite Strain Modeling of Debonding in Particle-Reinforced Elastomers*, Computational Materials Science, **45**, 611-616, (2009).

[130] I. Doghri and C. Friebel, *Effective Elasto-plastic Properties of Inclusion-Reinforced Composites. Study of Shape, Orientation and Cyclic Response*, Mechanics of Materials, **37**, (2005).

[131] O. Pierard, C. Gonzalez, J. Segurado, J. Llorca and I. Doghri, *Micromechanics of Elasto-Plastic Materials Reinforced with Ellipsoidal Inclusions*, International Journal of Solids and Structures, **44**, 6945-6962, (2007).

[132] A. Selmi, C. Friebel, I. Doghri and H. Hassis, *Prediction of the Elastic Properties of Single Walled Carbon Nanotube Reinforced Polymers: A Comparative Study of Several Micromechanical Models*, Composites Science and Technology, **67**, 2071-2084, (2007).

[133] DIGIMAT, *Mean-Field Homogenization User's Manual Version 4.1.2*, e-Xstream engineering SA, Louvain-la-Neuve, Belgium, 2011.

[134] S. Nemat-Nasser, M. Hori and W. Bielski, *Micromechanics: Overall Properties of Heterogeneous Materials*, North-Holland Amsterdam, (1993).

[135] DIGIMAT, *Linear and Nonlinear Multi-scale Material Modeling Software*, e-Xstream engineering SA, Louvain-la-Neuve, Belgium, 2003.

[136] Y. Benveniste, *A New Approach to the Application of Mori-Tanaka's Theory in Composite Materials*, Mechanics of Materials, **6**, 147-157, (1987).

[137] G. Lielens, *Micro-Macro Modeling of Structured Materials*, Phd thesis, Universite Catholique de Louvain, Belgium, (1999).

[138] F. Giese, C. Eigenbrod and D. Koch, *A Novel Production Method for Porous Sound-Absorbing Ceramic Material for High-Temperature Applications*, International Journal of Applied Ceramic Technology, **7**, (2010).

[139] M. J. Statham, F. Hammett, B. Harris, R. G. Cooke, R. M. Jordan and A. Roche, *Net-Shape Manufacture of Low-Cost Ceramic Shapes by Freeze-Gelation*, Journal of Sol-Gel Science and Technology, **13**, 171-175, (1998).

[140] D. Koch, L. Andresen, T. Schmedders and G. Grathwohl, *Evolution of Porosity by Freeze Casting and Sintering of Sol-Gel Derived Ceramics*, Journal of Sol-Gel Science and Technology, **26**, 149-152, (2003).

[141] S. Deville, *Freeze-Casting of Porous Ceramics: A Review of Current Achievements and Issues*, Advanced Engineering Materials, **10**, 155-169, (2008).

[142] S. W. Sofie and F. Dogan, *Freeze Casting of Aqueous Alumina Slurries with Glycerol*, Journal of the American Ceramic Society, **84**, 1459-1464, (2004).

[143] T. Fukasawa, M. Ando, T. Ohji and S. Kanzaki, *Synthesis of Porous Ceramics with Complex Pore Structure by Freeze-Dry Processing*, Journal of the American Ceramic Society, **84**, 230-232, (2001).

[144] A. C. Cohen, *Maximum Likelihood Estimation in the Weibull Distribution Based on Complete and on Censored Samples*, Technometrics, **7**, 579-588, (1965).

[145] K. V. Bury, *Statistical Models in Applied Sciences*, Krieger Publishing Company, (1986).

[146] E. J. Gumbel, *Statistics of Extremes*, Dover Publishings, (2004).

[147] F. I. Chu, R. E. Taylor and A. B. Donaldson, *Thermal Diffusivity Measurements at High Temperatures by the Radial Flash Method*, Journal of Applied Physics, **51**, 336-336, (1980).

[148] U. Hammerschmidt, *A New Pulse Hot Strip Sensor for Measuring Thermal Conductivity and Thermal Diffusivity of Solids*, International Journal of Thermophysics, **24**, 675-682, (2003).

[149] U. Hammerschmidt, *A Quasi-Steady State Technique to Measure the Thermal Conductivity*, International Journal of Thermophysics, **24**, 1291-1312, (2003).

[150] U. Hammerschmidt and V. Meier, *New Transient Hot-Bridge Sensor to Measure Thermal Conductivity, Thermal Diffusivity, and Volumetric Specific Heat*, International Journal of Thermophysics, **27**, 840-865, (2006).

[151] S. E. Gustafsson, *Transient Hot Strip Techniques for Measuring Thermal Conductivity and Thermal Diffusivity*, The Rigaku Journal, **4**, 16-28, (1987).

[152] S. M. Marcus and R. L. Blaine, *Thermal Conductivity of Polymers, Glasses and Ceramics by Modulated DSC*, Thermochimica Acta, **243**, 231-239, (1994).

[153] E. Verdonck, K. Schaap and L. C. Thomas, *A Discussion of the Principles and Applications of Modulated Temperature DSC (MTDSC)*, International Journal of Pharmaceutics, **192**, 3-20, (1999).

[154] Z. P. Bazant and S.-D. Pang, *Activation Energy Based Extreme Value Statistics and Size Effect in Brittle and Quasibrittle Fracture*, Journal of the Mechanics and Physics of Solids, **55**, 91-131, (2007).

[155] Abaqus, *Theory Manual – Version 6.10 Edition*, Hibbit and Karlson and Sorensen Inc, 2010.

[156] F. Giese, *Entwicklung und Charakterisierung keramischer Porenabsorber zur Dämpfung thermoakustischer Instabilitäten*, Dissertation, Bremen, Bremen, (2011).

Curriculum Vitae

Name:	Reza Malekmohammadi
Date of Birth:	28.08.1978
Place of Birth:	Teheran-Iran
Nationality:	German, Iranian

Experience

2007-2011	Research assistant in the department of Applied Mechanics at the University of Bremen

Education

2003-2006	Master of Science in Production Engineering at the University of Bremen, Germany
1997-2002	Bachelor of Science in Mechanical Engineering at the Amirkabir University of Technology, Tehran, Iran